UNIVERSITÀ DEGLI STUDI DI NAPOLI FEDERICO II

POLYTECHNIC AND BASIC SCIENCES SCHOOL

TEACHING AREA - MATHEMATICAL, PHYSICAL AND NATURAL SCIENCES

PHD IN CHEMICAL SCIENCES, XXX-CYCLE

HETEROGENEOUS ZIEGLER-NATTA CATALYSTS: EXPERIMENTAL AND COMPUTATIONAL STUDY BY MEANS OF RESONANCE-BASED TECHNIQUES

GIUSEPPE ANTINUCCI*

SUPERVISOR:
PROF. VINCENZO BUSICO*

ASSESSOR:
PROF. NADIA REGA

PHD SCHOOL COORDINATOR:
PROF. LUIGI PADUANO

2014-2017

* Dutch Polymer Institute (DPI), P.O. Box 902, 5600 AX Eindhoven, the Netherlands

Table of Contents

This research forms part of the research programme of the Dutch Polymer Institute (DPI), project #793

Abstract

Ziegler-Natta Catalysts (ZNC) for the industrial production of isotactic polypropylene were introduced over 60 years ago. Compared with the original $TiCl_3$-based systems, present-day versions are much more complex: they are comprised of a solid precatalyst, in which $TiCl_4$ and a suitable Lewis Base (LB; e.g. an ester or ether) are co-adsorbed on a nano-structured $MgCl_2$ support, and a soluble cocatalyst made of a trialkyl-Al compound and another LB (typically an alkoxysilane). Despite a tremendous commercial success, the question of the exact nature and structure of the active species in such formulations remains open. This hampered rational catalyst design; as a matter of fact, progress has been – and still is – mostly based on trial-and-error.

In this Ph.D. project, which is part of the research programme of the Dutch Polymer Institute (DPI), real-world ZNC and model systems thereof were investigated with an integrated experimental and computational approach. Advanced solid-state Quadrupolar Nuclear Magnetic Resonance (QNMR) and Electron Spin Resonance (ESR) characterizations were backed by state-of-the-art periodic and cluster dispersion-corrected Density Functional Theory (DFT-D) models. The latter were aimed to calculate relevant spectroscopic parameters of use for the interpretation of the spectroscopic data. The project was a collaboration between the host Institution, namely the Federico II University of Naples (Italy; research group of Prof. Vincenzo Busico), Radboud Universiteit Nijmegen (The Netherlands; research group of Prof. Arno Kentgens), the University of Turin (Italy; research group of Prof. Elio Giamello), and ETH Zurich (Switzerland; research group of Prof. Christophe Copéret).

Owing to the complexity of ZNC, a bottom-up approach was applied. The first step was an investigation of the neat $MgCl_2$ support, and simple $MgCl_2/TiCl_4$ or $MgCl_2$/LB binary adducts, so as to achieve a deeper insight into the pairwise interactions between components. The investigation was then extended to ternary $MgCl_2/TiCl_4$/LB systems (including industrial precatalysts), and finally to their activation process.

Chapter 1 of the present thesis provides a brief historical overview of ZNC, and introduces the challenges of their mechanistic study.

Chapter 2 discusses the question how to prepare dry samples of 'activated' (i.e. high-surface-area) $MgCl_2$ and $MgCl_2$/LB adducts for meaningful spectroscopic studies. $MgCl_2$ is an exceedingly hygroscopic solid, and water adsorption can lead to flawed results. Two $MgCl_2$ drying protocols were applied, and evaluated comparatively: one entailed treatment of $MgCl_2$ with $SiCl_4$ in aliphatic hydrocarbon slurry; another consisted in prolonged exposure to a flow of dry N_2 at 250°C. The thus obtained dry samples, either neat or after chemisorption of a LB, were characterized by FTIR and/or solid-state NMR. The conclusion was that it is virtually impossible to prevent water from re-adsorbing on (activated) dry $MgCl_2$ under non-UHV conditions (UHV = Ultra High Vacuum), even when the samples are manipulated inside a high-performance glovebox. On the other hand, activated $MgCl_2$/LB adducts featured only minor water contents (despite a much lower average particle size); we trace this finding to an effective 'shielding' of the surface by the chemisorbed LB molecules.

Chapter 3 reports on the characterization of $MgCl_2$/LB model adducts by means of advanced solid-state (Q)NMR techniques. The study included DFT-D calculations of quadrupole coupling constants and chemical shift tensors for systems at variable degree of surface coverage, as an aid to the interpretation

of the experimental spectra. All results consistently indicated that certain LB (e.g. 1,3-diethers) chemisorb in preference on $MgCl_2$ crystal terminations exposing tetra-coordinated Mg, whereas others (e.g. phthalates) do not feature any strong preference for a particular crystal edge.

Chapter 4 addresses the long-standing question of the chemical activation of the precatalyst by means of the Al-alkyl cocatalyst. DFT-D evaluations of epitaxial Ti_xCl_{3x} (x = 1 or 2) adsorbates on $MgCl_2$(104) and $MgCl_2$(110) terminations, as originally proposed by Corradini and coworkers, were carried out using high-end periodic and cluster methods. The relative stability of various Ti(III) model species *via* reduction and alkylation of Ti(IV) precursors by Et_3Al was calculated, along with the Ti(III) ESR parameters for comparison with experimental data for model and real-world catalysts. Overall, the results pointed to mononuclear Ti(III) adsorbates on $MgCl_2$(110) terminations as the most plausible ZNC active species.

Finally**,** a brief summary and an outlook of the study are given in **Chapter 5**.

Parts of this thesis have already been published in peer-reviewed journals:

- Blaakmeer, E. S. (Merijn), Antinucci G., Busico V., van Eck, Ernst R. H., Kentgens, Arno P. M.; Solid-State Investigation of $MgCl_2$, Crystal Support. *Journal of Physical Chemistry C*, **2016**, *120*, 6063.
- Morra E., Giamello E., Van Doorslaer S., Antinucci G., D'Amore M., Busico V., Chiesa M.; Probing the Coordinative Unsaturation and Local Environment of Ti^{3+} Sites in an Activated High-Yield Ziegler-Natta Catalyst. *Angew. Chem. Int. Ed.*, **2015**, *54*, 4857.

Chapter 1. Introduction

1.1 This project in a pill

Introduced more than 60 years ago with resounding success, Ti-based Ziegler-Natta Catalysts (ZNC) still have the monopoly on the industrial production of isotactic polypropylene (iPP). iPP represents the second largest-volume polymer on the market after polyethylene, and accounts for approximately 2.5% of the overall chemical sales per year. The annual production has more than doubled in the first years of the new millennium; the current global capacity of ca. 60 million metric tons per year continues to grow annually by ~4%, and revenues are expected to escalate to over $100 billions by 2021.[1]

The original ZNC consisting of crystalline $TiCl_3$ in combination with a trialkyl-Al[2] were plagued by a low productivity and a comparatively poor stereoselectivity.[3] In the late 1960s, a breakthrough was the introduction of supported versions. These are multi-component formulations consisting of:

a) a solid precatalyst, in which a Ti precursor (usually $TiCl_4$) is co-adsorbed with a Lewis Base (LB, often referred to as the 'Internal' Donor, ID; e.g., an aromatic ester or a 1,3-diether) on a nano-structured $MgCl_2$ support
b) a soluble cocatalyst, comprised of a trialkyl-Al (usually triethyl-Al, TEA) and a second LB (the 'External' Donor, ED; typically, an alkoxysilane).

Despite decades of extensive experimental and theoretical studies, ZNC are still poorly understood both from a structural and a mechanistic viewpoint. There is consensus in the literature that precatalyst activation by the alkyl-Al generates alkylated Ti(III) species, which would be the active sites, but the

exact structure of such species is unknown, as is(are) the role(s) of the LB. The unambiguous identification of surface structure and dynamics would evidently open the door to a (more) rational catalyst design and tuning, so as to predict the right formulation for a desired performance. Unfortunately, it is extremely difficult to gather adequate information from experiments, because these solids are extremely reactive and highly disordered; moreover, the fraction of active Ti is reported to be low.[3-5] So far, no analytical technique was able to shed enough light on the inner workings of these systems, and the most valuable information was derived from 'circumstantial evidence', by analyzing the microstructure of the polymers as a catalyst's 'fingerprint'.

A method with the potential to directly characterize the active sites is solid-state Nuclear Magnetic Resonance (NMR). The versatility of NMR derives from both the sensitivity of the nuclear spins toward local environment, and the possibility to manipulate them in elaborate ways so as to extract the desired structural and/or dynamic information. In the specific case of ZNC, however, NMR is limited to the analysis of the precatalysts, because activation leads to paramagnetic Ti(III) ($3d^1$, S=1/2) which dramatically complicates the signal. Electron Spin Resonance (ESR), in turn, can be a powerful tool to look at the electronic structure and local coordination environment of Ti(III) centers; unfortunately though, multinuclear Ti-species are ESR-silent, thus only mononuclear species can be investigated.

In this project, we characterized $MgCl_2$-supported ZNC by means of state-of-the-art NMR and ESR techniques, integrated with dispersion-corrected Density Functional Theory (DFT-D) calculations. We adopted a bottom-up approach, from neat $MgCl_2$ to simple binary $MgCl_2$/$TiCl_4$ and $MgCl_2$/LB model adducts up to industrial $MgCl_2$/$TiCl_4$/LB (pre)catalysts. As we shall see, the results of the study were of great help to narrow the hypotheses on the structure and behavior of the catalytic surfaces.

1.2 A brief mechanistic introduction to ZNC

1.2.1 From $TiCl_3$ to $MgCl_2/TiCl_4$

Present-day ZNC for iPP production descend from those discovered in the laboratories of Giulio Natta at the Milan Polytechnic in 1954, which featured $TiCl_3$ in one of its 'violet' crystalline modifications (α, γ, δ) as the solid precatalyst.[2] All such modifications are characterized by structural layers made by two planes of close-packed Cl atoms, with Ti atoms occupying 2/3 of the octahedral cavities in between; the various polymorphs correspond to different stacking modes of the structural layers perpendicularly to the basal planes. Detailed investigations highlighted the chirality of the Ti centers, in the bulk as well as on lateral terminations of the structural layers (Figure 1.1).[6,7] Therefore, it was possible to understand the much higher stereoselectivity in propene polymerization of these modifications, compared with the 'brown' polymorph with fibrillar structure and non-chiral Ti originally obtained by Ziegler.[2a] A seminal mechanism for the enantioselective insertion of propene into chirotopic Ti-C bonds was proposed in the 1960s by Cossee and Arlman.[8]

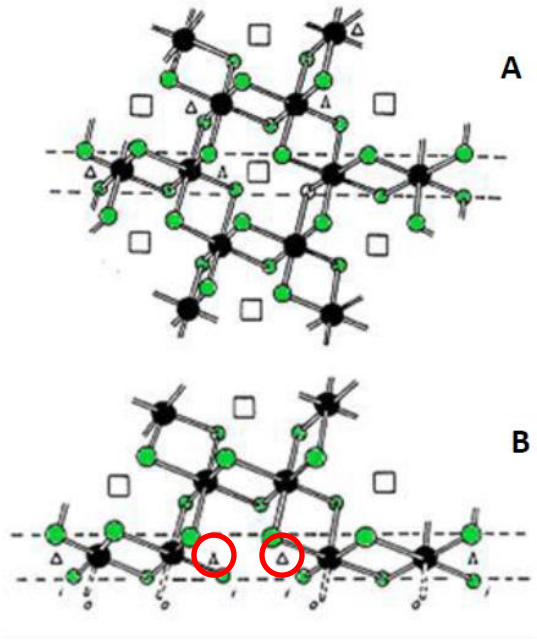

Figure 1.1 Schematic representation of a 'violet' $TiCl_3$ structural layer, before (**A**) and after (**B**) being cut along the (110) crystallographic direction. The Δ or Λ chirality of the Ti centers is explicitly indicated.[6]

The main drawback of $TiCl_3$-based catalysts was the low productivity; even with catalysts characterized by high surface area, 10-15 kg of iPP per gram of catalyst was the maximum achievable mileage.[3] This resulted into a non-negligible residual amount of acidic Ti-Cl bonds remaining in the polymer, which therefore had to go through a laborious (and cost-intensive) de-ashing procedure.[3-4] Supporting the active Ti species on an inert matrix, thereby increasing the productivity referred to Ti, looked like an obvious solution to the problem. However, as we noted before, the bulk of the crystal in 'violet' $TiCl_3$ is not an innocent self-support, because its crystal structure determines the stereogenic environment of the surface-exposed Ti centers. As a matter of fact, when typical supports like calcined silica or alumina were impregnated with $TiCl_4$ and reacted with a trialkyl-Al for Ti alkylation/reduction, only

poorly active and low-stereoselective catalysts were obtained.[3-4] Intriguingly, using MgO as the support led to more active systems; it soon turned out that $TiCl_4$ is able to chlorinate MgO, ending up with a $MgCl_2/TiCl_4$ adduct. Using authentic $MgCl_2$ as the support led to even better catalysts, with productivities in excess to 150 kg of polymer per gram of Ti, although less than 40 wt-% of the polymer was isotactic. In a relatively short time, it was then discovered that addition of certain LB (such as aromatic monoesters) to the catalyst formulation, either as components of the solid precatalysts or in combination with the alkyl-Al cocatalyst, led to dramatic improvements of stereoselectivity (>90% iPP) and, quite surprisingly, productivity as well.[3-4] Trial-and-error searches of better LB led to the identification of dialkylphthalates, 1,3-dimethoxypropanes and dialkylsuccinates as preferred ID, and alkoxysilanes as best-in-class ED; present-day catalysts can produce up to 99 wt-% iPP with a productivity of 1-2 metric tons per gram of Ti (Table 1.1).[3,4]

Table 1.1 Typical formulations and performance of ZNC for iPP.[4]

Internal Donor (ID)	External Donor (ED)	Productivity [10^3 kg(PP)/g(Ti)]	Index of Isotacticity (I.I.)	M_w/M_n
ethyl benzoate	methyl *p*-toluate	0.5	> 95%	6 – 8
dibutyl phthalate	$R^1R^2Si(OMe)_2$	1 – 2	> 98%	5 – 7
2,2-dialkyl-1,3-dimethoxypropane	$R^1R^2Si(OMe)_2$ (optional)	> 2	> 97%	3 – 5
dialkyl succinate	$R^1R^2Si(OMe)_2$	1 – 2	> 97%	> 10

Understanding the reason(s) for this extraordinary performance was, and still is, very challenging. Crystalline $MgCl_2$ has a layer structure which is very similar to 'violet' $TiCl_3$, with structural layers in which all octahedral cavities

are filled by Mg.[3,4,7] This suggested the possibility to extend the crystallochemical model by Cossee and Arlman[8] from $TiCl_3$ to the $MgCl_2$-supported homologues. The starting assumption is that $TiCl_4$ chemisorption can only take place at coordinatively unsaturated lateral terminations of the $MgCl_2$ crystals. According to Giannini[9] and Corradini[10], the most plausible terminations would be $MgCl_2$(100) and $MgCl_2$(110), exposing 5-coordinated and 4-coordinated Mg atoms respectively. A pioneering paper by Corradini and co-workers[10] proposed that stereoselective active species result from the epitaxial chemisorption of dinuclear Ti_2Cl_8 species on $MgCl_2$(100) (104 in α-$MgCl_2$), followed by reduction to Ti_2Cl_6 and subsequent alkylation by the alkyl-Al (Figure 1.2-A and A'); according to these authors, the local coordination environment of Ti would be practically identical to that on authentic 'violet' $TiCl_3$ crystal edges. Sterically more open (albeit chiral) non-stereoselective active species, on the other hand, would originate from mononuclear epitaxial $TiCl_4$ chemisorption on $MgCl_2$(110) (Figure 1.2-B and B').[10] Such species would not form in the presence of a LB, because chemisorption of the latter would be stronger.[10] Years later, 1,3-dimethoxypropanes were claimed as a class of LB specifically designed to chelate 4-coordinated Mg on $MgCl_2$(110).[11]

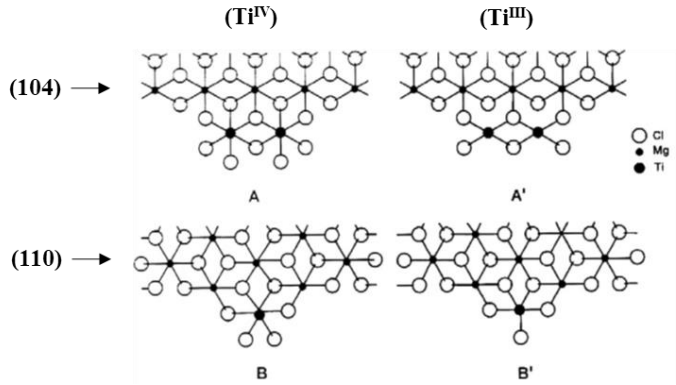

Figure 1.2 Epitaxial models of Ti_xCl_{4x} (**A** and **B**) and Ti_xCl_{3x} (**A'** and **B'**) species on lateral $MgCl_2$ crystal terminations, according to Corradini et al.[10]

It should be noted at this point that the aforementioned hypotheses do not involve any direct interactions between Ti species and LB molecules on the surface of the support, because the two would reside at different $MgCl_2$ crystal terminations.[10] In the 1990s, though, experimental and computational evidence was reported in conflict with Corradini's model.

Thorough microstructural analyses of the polymer demonstrated that LB have strong and idiosyncratic effects on PP stereoregularity.[12] It is worth recalling here that all ZNC are 'multi-sited', i.e. feature multiple classes of active species with different stereoselectivities. Even the best industrial systems contain a fraction of active species yielding a poorly stereoregular PP. The amount of weakly crystalline 'atactic' by-product can be quantified by means of solvent fractionation (e.g. dissolution in hot xylene followed by fractional precipitation, or extraction with boiling heptane); the weight-% of insoluble highly crystalline 'isotactic' polymer is often referred to as 'Index of Isotacticity' (I.I.). It has long been known that the I.I. can be dramatically enhanced by catalyst modification with proper ID/ED combinations; what took longer to be noted, on the other hand, is that a different choice of LB also affects the microstructure of the individual PP fractions (and also other important characteristics like polymer molar mass distribution; Table 1.1). In view of that, Busico *et al.*[12] introduced, and recently refined[13], a novel active site model according to which LB (or alkyl-Al) molecules adsorbed on the $MgCl_2$ surface at non-bonded contact with the Ti(III) species modulate the catalytic pocket similarly to ancillary ligand(s) in molecular catalyst. In the same papers, these authors showed that epitaxial mononuclear isotactic-selective $TiCl_n$ species (n = 3, 4) may well form on $MgCl_2$(110) terminations too.

Around the same time, the first quantitative DFT calculations of $TiCl_4$ adsorption energy on various $MgCl_2$ crystal surfaces were reported by different

authors, with strikingly conflicting results. To one extreme, Martinsky found that adsorption of both mononuclear $TiCl_4$ on $MgCl_2$(110) and dinuclear Ti_2Cl_8 on $MgCl_2$(104) is strong[14], which would agree with Corradini's view.[10] To the other extreme, Ziegler[15] concluded that $TiCl_4$ binding to $MgCl_2$ is very weak, and *all* epitaxial models proposed that far would be unstable. In between these two claims are the results by Parrinello[16], Cavallo[17], Stukalov[18], Taniike[19] and others. Much more recently, Busico and Causà[20] pointed out that $TiCl_4$ adsorption on $MgCl_2$ is largely dispersion-driven, and the inclusion of dispersion forces in DFT evaluations of binding energy is mandatory for meaningful calculations. When this is done, the conclusion is that $TiCl_4$ can only chemisorb on $MgCl_2$(110) or alike surfaces exposing 4-coordinated Mg[21]; we will comment more extensively on this important point at a later stage (§ 1.3.3).

1.2.2 Some basic remarks on ZNC preparation

Several protocols for the preparation of $MgCl_2/TiCl_4$/ID precatalysts have been proposed.[3] One is intensively ball-milling $MgCl_2$, $TiCl_4$ and ID together, or $MgCl_2$ and ID alone followed by impregnation of the binary $MgCl_2$/ID adduct with neat or concentrated $TiCl_4$ at high temperature ('titanation' step).[3] In both cases, any loosely bound $TiCl_4$ and ID fraction is removed by hot-washing with hydrocarbons. Pre-catalysts prepared in this way typically contain 1-2 wt-% of Ti and 5-10 wt-% of ID. This protocol is very simple (albeit harsh at the titanation step), but the drawback is that no control over catalyst particle morphology can be achieved. Since catalyst morphology is replicated at a later stage by the produced iPP particles, which important beneficial effects on process management, the drawback is severe.

More recent preparation routes start from soluble or low-melting $MgCl_2$ precursors (such as e.g. MgR_2, or $MgCl_2$/alcohol adducts), that are compatible with the adoption of emulsion, spray-drying or spray-cooling techniques at the titanation step.[22] The organic moieties are removed by reaction with excess $TiCl_4$ at high temperature in the presence of the ID, so as to end-up with a precatalyst featuring secondary particles with highly controlled spherical morphology and a diameter in the range of 10 to 100 μm. These are aggregates of billions of primary $MgCl_2$/$TiCl_4$/ID nano-particles, with high Ti (up to 5 wt-%) and ID (up to 20 wt-%) contents.[4]

No evidence has been reported thus far that the primary particles obtained with the two protocols are significantly different. It is generally accepted that, in both cases, the most important role of the ID is to stabilize by strong chemisorption the lateral terminations of $MgCl_2$ crystallites, so that nano-sized primary particles can be obtained.

1.2.3 Surface science and spectroscopic studies of ZNC

Reports on direct experimental observations of ZN (pre)catalysts are limited. As noted before, these solids are extremely reactive, and even the smallest amounts of ubiquitous contaminants (e.g. H_2O, O_2) can alter the sample and consequently affect the results. Moreover, it should be kept in mind that the fraction of active Ti in ZNC is reported to be low[4,5], which implies that the minor amounts of catalytic species can escape detection.

Based on High-Resolution Transmission Electron Microscopy (TEM) images (Figure 1.3), Terano[23] reported that 'activated' $MgCl_2$ samples exhibit, in addition to the basal (001) planes, two kinds of lateral terminations, namely 'atomically flat' (assumed to belong to (110)-type surfaces) and 'atomically

rough' planes (perpendicular to the former). The adsorption of $TiCl_4$ on $MgCl_2$ severely distorts the crystals and renders the surfaces 'no longer atomically flat planes'.

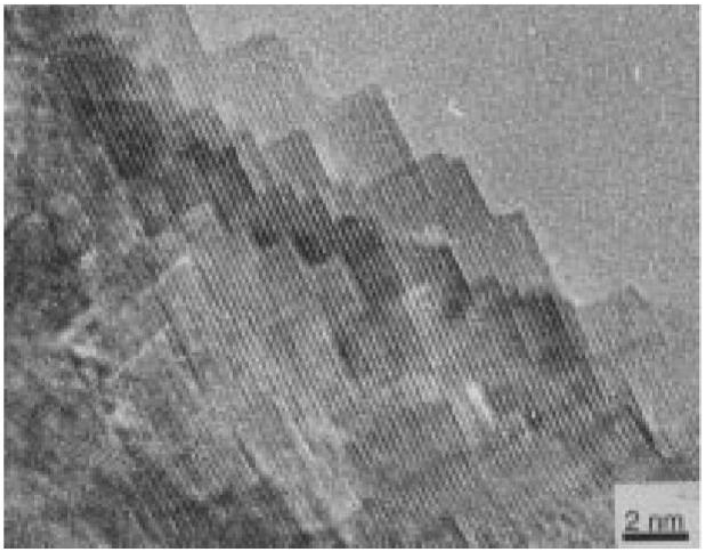

Figure 1.3 High-Resolution TEM image of an 'activated' crystalline $MgCl_2$ sample.[23]

Electron microscopy observations by Oleshko[24] and Thüne[25] demonstrated that samples obtained from $MgCl_2$•*n*ROH precursors[26] also contain crystalline $MgCl_2$ domains, along with regions characterized by extensive disorder (Figure 1.4). Therefore, the $MgCl_2$ layer leit-motiv seems to be a common feature of physically and chemically activated ZNC.

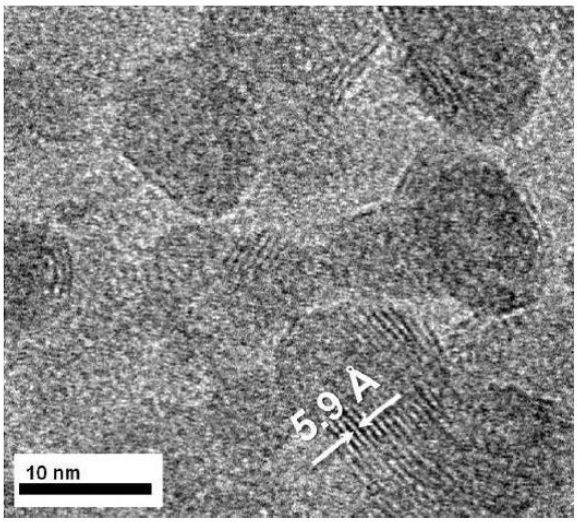

Figure 1.4. TEM image of a $MgCl_2$ film obtained by spin-coating from a $MgCl_2$ solution in ethanol at 30°C. The spacing of 5.9 Å is characteristic of the perpendicular stacking of the structural layers in crystalline $MgCl_2$.[25]

Magni and Somorjai[27] studied the interaction of $TiCl_4$ with $MgCl_2$ films grown on a gold support in a UHV chamber. At low temperature (<110 K), $TiCl_4$ turned out to bind only weakly, and was completely removed under vacuum. On the other hand, when the film was annealed at high temperature (~300 K) prior to applying vacuum, 1-2 % of Ti was observed to bind more strongly, and heating the system up to the sublimation temperature of $MgCl_2$ was required to remove it. Notably, 1-2 wt-% is also the typical Ti content of $MgCl_2$-supported ZNC precatalysts. According to these authors, the strongly bound Ti might have been included in the bulk of the $MgCl_2$ film, but the exact meaning of this remark and its possible implications for catalysis were not discussed.

Recent vibrational spectroscopic studies by Zerbi[28] concluded that surface Ti species in ZNC are most likely octahedral adducts bound to 4-coordinated Mg

(e.g., on $MgCl_2$(110) or equivalent surfaces). This agrees with the aforementioned DFT-D calculations.[21]

1.3 Computational Modeling of ZNC

1.3.1 From Molecular Mechanics to Quantum Mechanics

Until the late 1980s, Molecular Mechanics (MM) was the only available computational tool for simulating ZNC.[6,10] This technique is based on the empirical parametrization of interactions between the atoms of the simulated systems, with the presence or absence of bonds decided by the researcher. The quality of the results is mainly determined by the quality of the parametrization. High-quality parametrizations are available for organic molecules, but not for metal atom containing systems. In addition, MM methods do not handle making and breaking of chemical bonds, thus precluding prediction of reaction barriers. Some very interesting results have been obtained based on judicious use of MM, as illustrated by Corradini's 'growing chain orientation mechanism of stereocontrol' which remains a milestone in the understanding of stereoselective olefin polymerization.[7] Nevertheless, nowadays MM has been mostly superseded by the use of electronic structure methods, at least for systems smaller than proteins.

Despite the advances in CPU processing power in the last decades, *rigorous* Quantum Mechanical (QM) treatment is currently still unfeasible for systems with more than 20 heavy atoms, and therefore approximations like Density Functional Theory (DFT) are required. DFT calculations can be carried out with different levels of accuracy, forming a hierarchy that is often represented by the rungs of a ladder. The simplest approximation for the exchange-correlation energy used in DFT is the 'local density approximation' (LDA), which approximates the exchange-correlation energy density at a given

position as a function of the electron density at that same local position. At the next level of sophistication comes the 'generalized gradient approximation' (GGA), for which the energy density approximation also depends on the gradient of the density at that given position. One level above this is 'meta-GGA', for which the energy density depends also on the local kinetic energy density of the calculated Kohn–Sham orbitals. DFT scales approximately with N^3 (N = number of electrons), which is the same as Hartree-Fock (HF) theory, which crudely approximates the wavefunction. Higher-order approximations such as hybrid functionals or post-HF methods further improve the accuracy, but at higher computational cost; for example, CCSD(T) scales with N^7. Current DFT methods work well with systems featuring localized bonds, but have significant shortcomings in describing medium and long-range interactions, which is important in describing crystal structures (e.g. the inter-layer interactions in $MgCl_2$) as well as weak coordination complexes (e.g. olefin complexes). Several recently published benchmark papers[29,30] indicate that the large majority of DFT functionals, whether based on LDA, GGA or even the most popular meta-GGA, do not describe models relevant to ZNC systems well (compared to Coupled Cluster calculations as a reference).

A key point to make here is that standard DFT methods do not adequately reproduce dispersion forces, and whenever such interactions are non-negligible, semi-empirical ad-hoc corrections must be introduced in the calculations (see next section for details). Very recently, new generations of functionals covering medium and long-range correlations have been implemented, some specifically for use with crystals, and these seem to perform rather well[31], but their adoption is not yet widespread. Despite its shortcomings, DFT (with suitable choices of functional and dispersion corrections) is currently the only practical method for studying catalytic systems like ZNC.

Apart from choosing a DFT functional sited for a given problem, an additional important issue is the basis set selection. The first requirement is that basis sets for different elements in a molecule are balanced, else completely unrealistic electronic structures can be obtained. In addition, special precautions may be needed for specific situations, such as the addition of diffuse functions for atoms with a large negative charge (e.g. Cl).[29] Unfortunately, in the last 20 years many DFT studies of ZNC have been published without a serious analysis of the aforementioned aspects, which means that their results are potentially flawed.

1.3.2 Dispersion-corrected DFT (DFT-D) modeling

Dispersion forces, also called Van der Waals (VdW) forces or London forces, are non-covalent interactions between atoms or molecules, or between molecules and a solid surface. As is well-known, they are caused by correlations in the fluctuating polarizations of nearby atoms, resulting from a transient shift in electron density as the atoms approach; this generates a transient charge that can be either attractive or repulsive. When the interatomic distance is greater than ~0.6 nm the force is not strong enough to be observed. At the same time, when the interatomic distance is below ~0.4 nm the force becomes repulsive. These interactions play an important role in physisorption as well as chemisorption phenomena. The vast majority of DFT functionals do not describe such long-range interactions well.

Recently, new DFT functionals were developed in order to describe both short and long-range interactions as well as transition-metal bonding with high accuracy. One class of those are the Minnesota functionals, introduced a while ago with the publication of the M05 and M06 families (nowadays arriving at M11 and MN15 families).[31] These functionals use the meta-GGA

approximation and are additionally highly parametrized using a systematic fitting of experimental and computational data. Due to the large number of parameters and the complexity of the involved equations, the use of such functionals usually corresponds to a higher computational cost, which may pose a problem for investigations of very large systems.

An alternative solution, combining accuracy and efficiency but possibly with a more limited range of validity) has been proposed by Grimme and coworkers.[32] These authors define the dispersion-corrected total energy E_{MF-D} as follows:

$$E_{MF-D} = E_{MF} + E_{disp} \qquad \text{Eq. 1.1}$$

where E_{MF-D} is the mean-field energy (i.e. calculated using HF or a DFT method) and E_{disp} is an empirical dispersion correction. They then expand E_{disp}in a series of R_{ij}^{-6} terms (i.e. the distance between two atoms to the power of -6) using atom-pair dispersion coefficients C_6^{ij} estimated from per-element coefficients ($C_6^{ij} = \sqrt{C_6^{ii} C_6^{jj}}$):

$$E_{disp} = -s_6 \sum_{i=1}^{N-1} \sum_{j=i+1}^{N} \frac{C_6^{ij}}{R_{ij}^6} f_{dmp}(R_{ij}) \qquad \text{Eq. 1.2}$$

Here, s_6 is a global scaling factor that depends on the DFT functional to calculate the mean-field energy and *N* is the number of atoms in the system. To avoid overestimation of the correction between atoms with a distance well below typical Van der Waals radii (mostly bonded atoms), a damping function f_{dmp} is applied:

$$f_{dmp} = \frac{1}{1+e^{-\alpha\left(R_{ij}/R_{ij}^0 - 1\right)}} \qquad \text{Eq. 1.3}$$

where α is a constant value that determines the steepness of the damping function and R_{ij}^0 is the sum of atomic Van der Waals radii. This function decays very rapidly for small R_{ij}, resulting in a negligible contribution of dispersion corrections between bonded atoms.

Grimme's approach can be used with any DFT functional as well as for HF calculations, although different parametrizations are required for different functionals.

1.3.3 Periodic DFT-D modeling of ZNC

Modeling crystal structures or perfect crystal surfaces or edges is best done using periodic calculations. Periodic QM methods are inherently more complex than isolated-molecule methods. The first periodic DFT-D studies on $MgCl_2$-supported ZNC were carried out in the research group hosting the present thesis.[20,21] Periodic boundary conditions were adopted to investigate the relative stability of the most common surfaces exposed by a crystal of neat α-$MgCl_2$. Inclusion of dispersion forces was found to be crucial for a correct description of inter and intra-layer interactions. In particular, the authors found that the model obtained under thermodynamic conditions (in which relative surface stability determines crystal morphology), as well as a model including kinetic factors (using the method of Bravais, Friedel, Donnay and Harker[33]), only feature basal (001) planes and lateral terminations with 5-coordinated Mg (i.e., 104 or equivalent; Figure 1.5). Surfaces exposing 4-coordinated Mg (i.e. (110) or equivalent) are significantly higher in energy, and should at most constitute a very minor fraction.

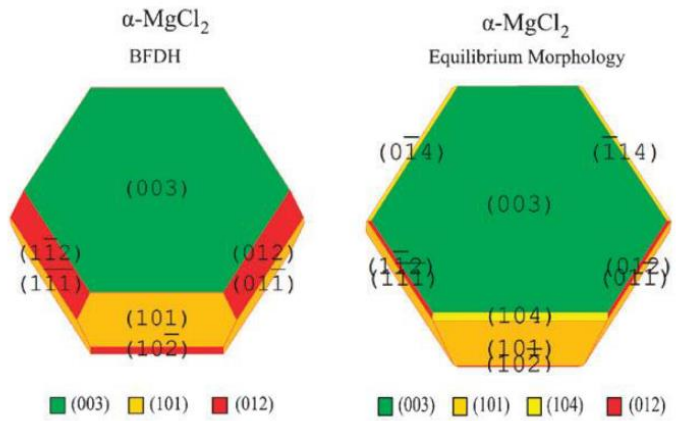

Figure 1.5 Crystal morphologies predicted for α-$MgCl_2$ using Bravais, Friedel, Donnay and Harker (BFDH) and equilibrium models.[20b]

On the other hand, a more recent study using the same computational approach for $MgCl_2$ adducts with various LB probe molecules (namely H_2O, NH_3 and EtOH)[34] concluded, plausibly, that the relative stability of the crystal terminations can be altered. In particular, the energy of formation of $MgCl_2$(110) was calculated to become negative (compared with the bulk) upon adsorption at full saturation (2:1 LB/Mg mole ratio). This is consistent with the known fact that H_2O and EtOH are solvents for $MgCl_2$. Some steric repulsion between adjacent adsorbate molecules showed up for EtOH molecules, leading to an appreciable drop of chemisorption energy between the first and the second EtOH molecule bound to each Mg center. This point is expected to become important with the sterically demanding LB molecules of industrial interest.

Perhaps the most important contribution of periodic DFT-D calculations was the study of $TiCl_4$ chemisorption on $MgCl_2$. This question was addressed by several computational groups, as mentioned before (§ 1.2.1), with largely different results.[14-19] It was only recently that Busico and co-workers[20,21]

demonstrated that $TiCl_4$ adsorption is a 'dispersion-driven' process, and therefore including dispersion contributions is mandatory for a correct analysis of the system. These authors concluded that $TiCl_4$ could only chemisorb on lateral $MgCl_2$ crystal terminations exposing 4-coordinated Mg atoms, e.g. $MgCl_2$(110) or equivalent.[21] Binding of monomeric and dimeric $TiCl_4$ units to $MgCl_2$(104) was calculated to be endergonic; therefore, long-standing models of stereoselective dinuclear Ti species on such surfaces[10] are flawed.

1.3.4 Periodic vs cluster DFT-D approaches

Periodic studies are extremely useful for studying crystal bulk and perfect surfaces and edges. However, they are less suited for the description of e.g. point defects, crystal corners, and the alike, as well as isolated adsorbate species. Due to the periodic nature of the calculation, very large unit cells are needed to isolate one individual species from its neighbors. Since the cost of a periodic DFT calculation scales as $\sim V^2$ to $\sim V^3$, using very large unit cells is impractical.

Even when modeling densely adsorbed species, periodic boundary conditions may be too restrictive. Consider for example a $MgCl_2$ edge with one EtOH molecule per exposed Mg atom. The 'natural' choice of a unit cell containing exactly one EtOH molecule implicitly forces all EtOH molecules on the edge to have exactly the same conformation. An arrangement with alternating different conformations might be lower in energy, but describing this requires - again - a larger cell. A more insidious issue is that the need for a larger unit cell may well be non-obvious, leading to artificially low binding energies. Finally, it is not entirely logical to use periodic calculations for the study of catalytic reactions; catalytic sites are rare, and will surely not occur in periodic 'lock-step' fashion on a surface or edge.

The alternative to periodic studies is a 'cluster' approach, wherein a fragment is taken out and isolated from a large crystal, and used to model isolated features of interest. The cluster model needs to be large enough so that the feature of interest 'feels' the same environment as it would on a crystal surface/edge. The cluster representing the crystal environment needs to be properly terminated, and this is not always trivial. Sometimes artificial terminating groups or ligands can be used. Judicious use of constraints may be helpful but also introduces some degree of arbitrariness. Often, even a minimally realistic cluster model contains many atoms. On the other hand, the approach was adopted and successfully benchmarked against periodic calculations in the framework of a Ph.D. thesis recently finalized in the same research group hosting the present one.[35] A recent publication by Cavallo et al. is an independent example of cluster approach to ZNC.[36]

1.4 Scope and objectives of this work

In this Ph.D. project, which is part of the research programme of the Dutch Polymer Institute (DPI), real-world ZNC and model systems thereof were investigated with an integrated experimental and computational approach. Advanced solid-state Quadrupolar Nuclear Magnetic Resonance (QNMR) and Electron Spin Resonance (ESR) characterizations were backed by state-of-the-art periodic and cluster dispersion-corrected Density Functional Theory (DFT-D) models. The latter were aimed to calculate relevant spectroscopic parameters of use for the interpretation of the spectroscopic data. The project was a collaboration between the host Institution, namely the Federico II University of Naples (Italy; research group of Prof. Vincenzo Busico),

Radboud Universiteit Nijmegen (The Netherlands; research group of Prof. Arno Kentgens), the University of Turin (Italy; research group of Prof. Elio Giamello), and ETH Zurich (Switzerland; research group of Prof. Christophe Copéret).

Owing to the complexity of ZNC, a bottom-up approach was applied. The first step was an investigation of the neat $MgCl_2$ support, and simple $MgCl_2/TiCl_4$ or $MgCl_2$/LB binary adducts, so as to achieve a deeper insight into the pairwise interactions between components. The investigation was then extended to ternary $MgCl_2/TiCl_4$/LB systems (including industrial precatalysts), and finally to their activation process.

Chapter 1 of the present thesis provides a brief historical overview of ZNC, and introduces the challenges of their mechanistic study.

Chapter 2 discusses the question how to prepare dry samples of 'activated' (i.e. high-surface-area) $MgCl_2$ and $MgCl_2$/LB adducts for meaningful spectroscopic studies. $MgCl_2$ is an exceedingly hygroscopic solid, and water adsorption can lead to flawed results. Two $MgCl_2$ drying protocols were applied, and evaluated comparatively: one entailed treatment of $MgCl_2$ with $SiCl_4$ in aliphatic hydrocarbon slurry; another consisted in prolonged exposure to a flow of dry N_2 at 250°C. The thus obtained dry samples, either neat or after chemisorption of a LB, were characterized by FTIR and/or solid-state NMR. The conclusion was that it is virtually impossible to prevent water from re-adsorbing on (activated) dry $MgCl_2$ under non-UHV conditions (UHV = Ultra High Vacuum), even when the samples are manipulated inside a high-performance glovebox. On the other hand, activated $MgCl_2$/LB adducts featured only minor water contents (despite a much lower average particle size); we trace this finding to an effective 'shielding' of the surface by the chemisorbed LB molecules.

Chapter 3 reports on the characterization of $MgCl_2$/LB model adducts by means of advanced solid-state (Q)NMR techniques. The study included DFT-D calculations of quadrupole coupling constants and chemical shift tensors for systems at variable degree of surface coverage, as an aid to the interpretation of the experimental spectra. All results consistently indicated that certain LB (e.g. 1,3-diethers) chemisorb in preference on $MgCl_2$ crystal terminations exposing tetra-coordinated Mg, whereas others (e.g. phthalates) do not feature any strong preference for a particular crystal edge.

Chapter 4 addresses the long-standing question of the chemical activation of the precatalyst by means of the Al-alkyl cocatalyst. DFT-D evaluations of epitaxial Ti_xCl_{3x} (x = 1 or 2) adsorbates on $MgCl_2$(104) and $MgCl_2$(110) terminations, as originally proposed by Corradini and coworkers, were carried out using high-end periodic and cluster methods. The relative stability of various Ti(III) model species *via* reduction and alkylation of Ti(IV) precursors by Et_3Al was calculated, along with the Ti(III) ESR parameters for comparison with experimental data for model and real-world catalysts. Overall, the results pointed to mononuclear Ti(III) adsorbates on $MgCl_2$(110) terminations as the most plausible ZNC active species.

Finally**,** a brief summary and an outlook of the study are given in **Chapter 5**.

Parts of this thesis have already been published in peer-reviewed journals:

- Blaakmeer, E. S. (Merijn), Antinucci G., Busico V., van Eck, Ernst R. H., Kentgens, Arno P. M.; Solid-State Investigation of $MgCl_2$, Crystal Support. *Journal of Physical Chemistry C*, **2016**, *120*, 6063.
- Morra E., Giamello E., Van Doorslaer S., Antinucci G., D'Amore M., Busico V., Chiesa M.; Probing the Coordinative Unsaturation and Local Environment of Ti^{3+} Sites in an Activated High-Yield Ziegler-Natta Catalyst. *Angew. Chem. Int. Ed.*, **2015**, *54*, 4857.

References

[1] Ceresna Research Market Study: Polypropylene, 2014, http://www.ceresana.com/en/market-studies/plastics/polypropylene/.

[2] (a) Boor, J., Jr. *Ziegler-Natta Catalysts and Polymerizations*; Academic Press: New York, 1979. (b) Kissin, Y. V., *Isospecific polymerization of olefins* (1st Ed.); Springer-Verlag, New York, 1985.

[3] Moore, E. P., Jr. (Ed.) *Polypropylene Handbook: Polymerization, Characterization, Properties, Processing, Applications*; Hanser Publishers: Munich, 1996.

[4] Cecchin, G.; Morini, G.; Piemontesi, F. *Ziegler-Natta Catalysts*. In *Kirk-Othmer Encyclopedia of Chemical Technology (5th Ed.)*, Wiley: Hoboken (NJ), 2007; *Vol. 26*, p. 502.

[5] (a) Mori, M.; Terano, M. *Trends Polym. Sci.* **1997**, *5*, 314. (b) Yu, Y.; Busico, V.; Budzelaar, P. H. M.; Vittoria, A.; Cipullo, R. *Angew. Chem. Int. Ed.* **2016**, *55*, 8590.

[6] Natta, G.; Corradini, P.; Allegra, G. *J. Polym. Sci.* **1961,** *51*, 399.

[7] (a) Corradini, P.; Barone, V.; Fusco, R.; Guerra, G. *Eur. Polym. J.* **1979,** *15*, 1133. (b) Corradini, P.; Guerra, G.; Fusco, R.; Barone, V. *Eur. Polym. J.* **1980,** *16*, 835.

[8] (a) Cossee, P. *J. Catal.* **1964,** *3*, 80. (b) Arlman, E. J. *J. Catal.* **1964,** *3*, 89. (c) Arlman, E. J.; Cossee, P. *J. Catal.* **1964,** *3*, 99.

[9] Giannini, U. *Makromol. Chem.* **1981,** *5*, 216.

[10] Corradini, P.; Barone, V.; Fusco, R.; Guerra, G. *Gazz. Chim. Ital.* **1983,** *113*, 601.

[11] (a) Scordamaglia, R.; Barino, L. *Macromol. Theory Simul.* **1998,** *7*, 399. (b) Albizzati, E.; Giannini, U.; Morini, G.; Galimberti, M.; Barino, L.; Scordamaglia, R. *Macromol. Symp.* **1995,** *89*, 73.

[12] Busico, V.; Cipullo, R.; Monaco, G.; Talarico, G.; Vacatello, M.; Chadwick, J. C.; Segre, A. L.; Sudmeijer, O. *Macromolecules* **1999,** *32*, 4173.

[13] Vittoria, A.; Meppelder, A.; Friederichs, N.; Busico, V.; Cipullo, R. *ACS Catal.* **2017**, *7*, 4509.

[14] Martinsky, C; Minot, C.; Ricart, J. M. *Surface Sci.* **2001**, *490*, 237.

[15] Seth, M.; Margl, P. M.; Ziegler, T. *Macromolecules* **2002,** *35*, 7815.

[16] (a) Boero, M.; Parrinello, M.; Terakura, K. *J. Am. Chem. Soc.* **1998**, *120*, 2746. (b) Boero, M.; Parrinello, M.; Hüffer, S.; Weiss, H. *J. Am. Chem. Soc.* **2000**, *122*, 501. (c) Boero, M.; Parrinello, M.; Weiss, H.; Hüffer, S. *J. Phys. Chem. A* **2001**, *105*, 5096.

[17] (a) Monaco, G.; Toto, M.; Guerra, G.; Corradini, P.; Cavallo, L. *Macromolecules* **2000**, *33*, 8953. (b) Bahri-Laleh, N.; Correa, A.; Mehdipour-Ataei, S.; Arabi, H.; Haghighi, M. N.; Zohuri, G.; Cavallo, L. *Macromolecules* **2011**, *44*, 778.

[18] Stukalov, D. V.; Zilberberg, I. L.; Zakharov, V. A. *Macromolecules* **2009**, *42*, 8165.

[19] Taniike, T.; Terano, M. *Macromol. Rapid Commun.* **2008**, *29*, 1472.

[20] (a) Busico, V.; Causà, M.; Cipullo, R.; Credendino, R.; Cutillo, F.; Friederichs, N.; Lamanna, R.; Segre, A.; Van Axel Castelli, V. *J. Phys. Chem. C* **2008,** *112*, 1081. (b) Credendino, R.; Busico, V.; Causà, M.; Barone, V.; Budzelaar, P. H. M.; Zicovich-Wilson, C. *Phys. Chem. Chem. Phys.* **2009,** *11*, 6525.

[21] D'Amore, M.; Credendino, R.; Budzelaar, P. H. M.; Causà, M.; Busico, V. *J. Catal.* **2012,** *286*, 103.

[22] (a) Malizia, F.; Fait, A.; Cruciani, G., *Chemistry, Eur. J.* **2011,** *17*, 13892. (b) Huang, R.; Malizia, F.; Pennini, G.; Koning, C. E.; Chadwick, J. C., *Macromol. Rapid Commun.* **2008,** *29*, 1732. (c) Stukalov, D. V.; Zakharov, V. A.; Potapov, A. G.; Bukatov, G. D. *J. Catal.* **2009,** *266*, 39.

[23] Mori, H.; Sawada, M.; Higuchi, T.; Hasebe, K.; Otsuka, N.; Terano, M. *Macromol. Rapid Commun.* **1999,** *20*, 245.

[24] Oleshko, V. P.; Crozier, P. A.; Cantrell, R. D.; Westwood, A. D. *J. Electron Microsc.* **2002,** *51*, S27.

[25] Cheruvathur, A. V.; Langner, E. H. G.; Niemantsverdriet, J. W.; Thüne, P. C. *Langmuir* **2012,** *28*, 2643.

[26] Sozzani, P.; Bracco, S.; Comotti, A.; Simonutti, R.; Camurati, I. *J. Am. Chem. Soc.* **2003,** *125*, 12881.

[27] Magni, E.; Somorjai, G. A. *Surf. Sci.* **1997,** *377*, 824.

[28] (a) Brambilla, L.; Zerbi, G.; Nascetti, S.; Piemontesi, F.; Morini, G. *Macromol. Symp.* **2004,** *213*, 287. (b) Brambilla, L.; Zerbi, G.; Piemontesi, F.; Nascetti, S.; Morini, G. *J. Mol. Catal. A: Chem.* **2007,** *263*, 103. (c) Brambilla, L.; Zerbi, G.; Piemontesi, F.; Nascetti, S.; Morini, G. *J. Phys. Chem. C* **2010,** *114*, 11475.

[29] Ehm, C.; Antinucci, G.; Budzelaar, P. H. M.; Busico, V. *J. Organomet. Chem.* **2014,** *772*, 161.

[30] Correa, A.; Bahri-Laleh, N.; Cavallo, L. *Macromol. Chem. Phys.* **2013,** *214*, 1980.

[31] (a) Zhao, Y.; Schultz, N. E.; Truhlar, D. G. *J. Chem. Theory Comput.* **2006,** *2*, 364. (b) Zhao, Y.; Truhlar, D. G. *J. Chem. Phys.* **2006,** *125*, 194101. (c) Zhao, Y.; Schultz, N. E.; Truhlar, D. G. *J. Chem. Phys.* **2005,** *123*, 161103. (d) Zhao, Y.; Truhlar, D., *Theor. Chem. Acc.* **2008,** *120*, 215. (e) Peverati, R.; Truhlar, D. G. *J. Phys. Chem. Lett.* **2011,** *2*, 2810. (f) Yu, H. S.; He, X.; Truhlar, D. G. *J. Chem. Theory Comput.* **2016,** *12*, 1280.

[32] (a) Grimme, S. *J. Comput. Chem.* **2004,** *25*, 1463. (b) Grimme, S. *J. Comput. Chem.* **2006,** *27*, 1787. (c) Grimme, S.; Antony, J.; Ehrlich, S.; Krieg, H. *J. Chem. Phys.* **2010,** *132*, 1347. (d) Grimme, S.; Ehrlich, S.; Goerigk, L. *J. Comput. Chem.* **2011,** *32*, 1456.

[33] Donnay, J., D., H.; Harker, D. *Am. Mineral.* **1937,** *22*, 446.

[34] Capone, F.; Rongo, L.; D'Amore, M.; Budzelaar, P. H. M.; Busico, V. *J. Phys. Chem. C* **2013,** *117*, 24345.

[35] Breuza E. *Computational and Structural Study of Model and Industrial Ziegler-Natta Catalysts, PhD Thesis;* Federico II University of Naples, 2016.

[36] Credendino, R.; Liguori, D.; Fan, Z.; Morini, G.; Cavallo, L., *ACS Catal.* **2015,** *5*, 5431.

Chapter 2. Preparation of 'activated' $MgCl_2$ and $MgCl_2$/LB model adducts

2.1 Drying and physical activation of neat $MgCl_2$

As was discussed in the previous Chapter (§ 1.2.2), modern $MgCl_2/TiCl_4$/ID precatalysts with highly controlled spherical morphology are obtained by means of a 'chemical' activation process. 'Physical' activation by ball-milling has been abandoned in industrial practice, because it does not enable any morphology control[1]; on the other hand, for the purpose of the present project this route is appealing, because it is technically straightforward and yields very pure products. A poor morphology is not a drawback here, because our study does not comprise a polymerization step. Nowadays, highly efficient planetary ball-mills are capable of generating nano-structured materials in just a few hours, due to a mechanical energy 1000-fold larger than conventional ball-mills.[2] In the specific case of $MgCl_2$, samples featuring primary particles of similar size compared with chemically activated ones can be produced, as will be shown at a later stage in this chapter.

$MgCl_2$ is a highly hygroscopic substance. Water molecules can decorate the lateral terminations of $MgCl_2$ crystals; when these are saturated, further adsorption can ultimately lead to a number of crystalline hydrated phases ($MgCl_2 \cdot nH_2O$) with non-layered lattices[3] and distinctive powder X-ray diffraction (XRD) patterns (Figure 2.1). Even when dry $MgCl_2$ samples are handled inside a glovebox at very low water pressure (~10^{-6} bar), some water uptake will occur.

Figures 2.2 and 2.3 show the powder XRD pattern of the commercial batch of 'dry' $MgCl_2$ that was used as the starting material for this study. By comparison

with Figure 2.1, it can be concluded on inspection that the sample contained appreciable amounts of different hydrated phases, including $MgCl_2 \cdot 4H_2O$. Therefore, a dehydration treatment prior to planetary ball-milling was mandatory.

We applied two alternative drying protocols (see Appendix A-2 for experimental details). 'Chemical' drying entailed reaction of the $MgCl_2$ sample with a proper amount of $SiCl_4$ in heptane slurry at moderate temperature (50 to 65°C) under vigorous stirring for 4 to 5 hours, followed by filtration, thorough washing and vacuum drying. As is well-known, $SiCl_4$ is violently hydrolyzed by H_2O, with formation of amorphous silica and HCl(g). Importantly, unlike $TiCl_4$, $SiCl_4$ has no tendency to chemisorb on $MgCl_2$, therefore any excess $SiCl_4$ is readily removed by hot washing. 'Physical' drying, in turn, consisted in the treatment of $MgCl_2$ in a flow of dry nitrogen at 250 °C for 6 hours. No residual hydrated phases were detected by XRD (Figures 2.2 and 2.3) in samples recovered after chemical drying (CD) or physical drying (PD).

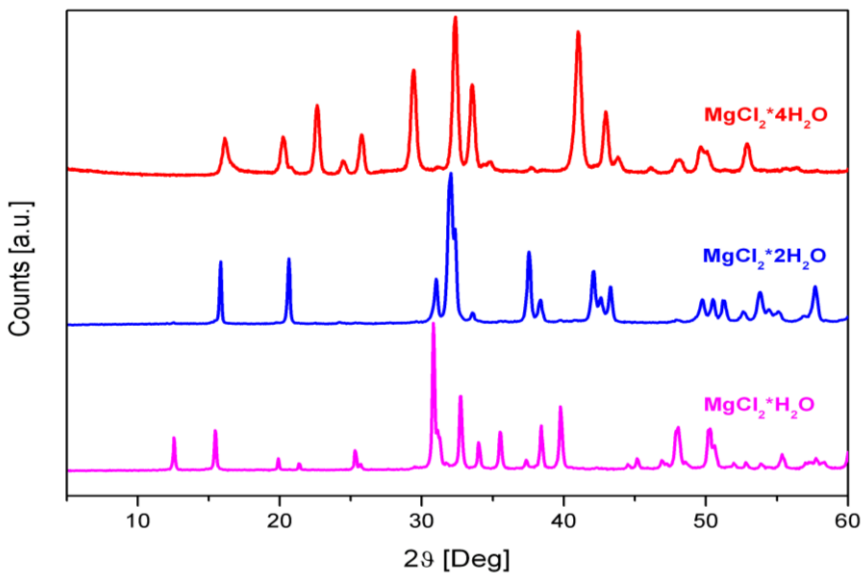

Figure 2.1. Powder XRD patterns of different $MgCl_2 \cdot nH_2O$ crystalline phases. Courtesy of Dr. Federica Malizia (Lyondellbasell).

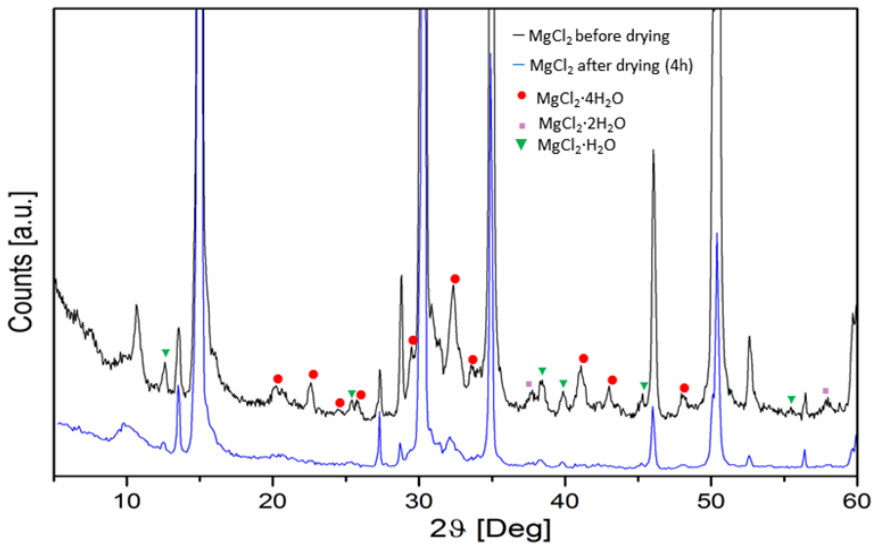

Figure 2.2. Powder XRD patterns of a commercial batch of 'dry' $MgCl_2$ before (black trace) and after (blue trace) ‘chemical’ drying.

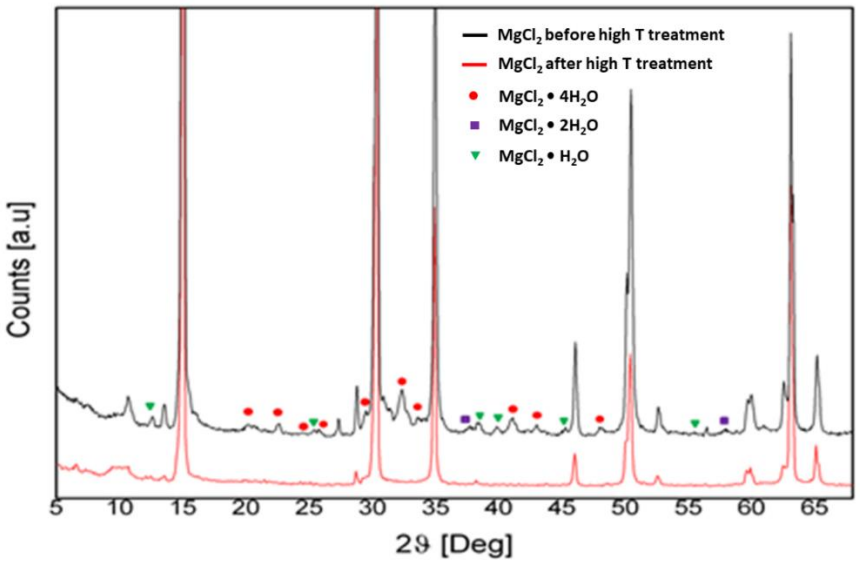

Figure 2.3. Powder XRD patterns of a commercial batch of 'dry' $MgCl_2$ before (black trace) and after (red trace) ‘physical’ drying.

Chemically dried and physically dried samples ($MgCl_2$(CD) and $MgCl_2$(PD), respectively) were activated by planetary ball-milling for 8 h (Appendix A-2 for details). The powder XRD pattern of $MgCl_2$(CD) before and after activation are shown in Figure 2.4; practically identical patterns were observed for $MgCl_2$(PD) (not shown). The spectrum of the unmilled sample is characteristic of the ordered α-form, featuring a hexagonal unit cell with $\underline{\boldsymbol{a}}$ = 0.364 nm, $\underline{\boldsymbol{c}}$ = 1.767 nm, and an $(ABC)_n$ stacking of the Cl planes.[4] In the spectra of activated samples, most diffraction peaks are broad, to the point that some coalesced and/or faded into the noise; this points to a δ-form with small coherent domains, due to a low crystallite size and/or the presence of lattice disorder.[5] Whereas it is difficult to separate the two effects, the literature suggests that the former is dominant.[6]

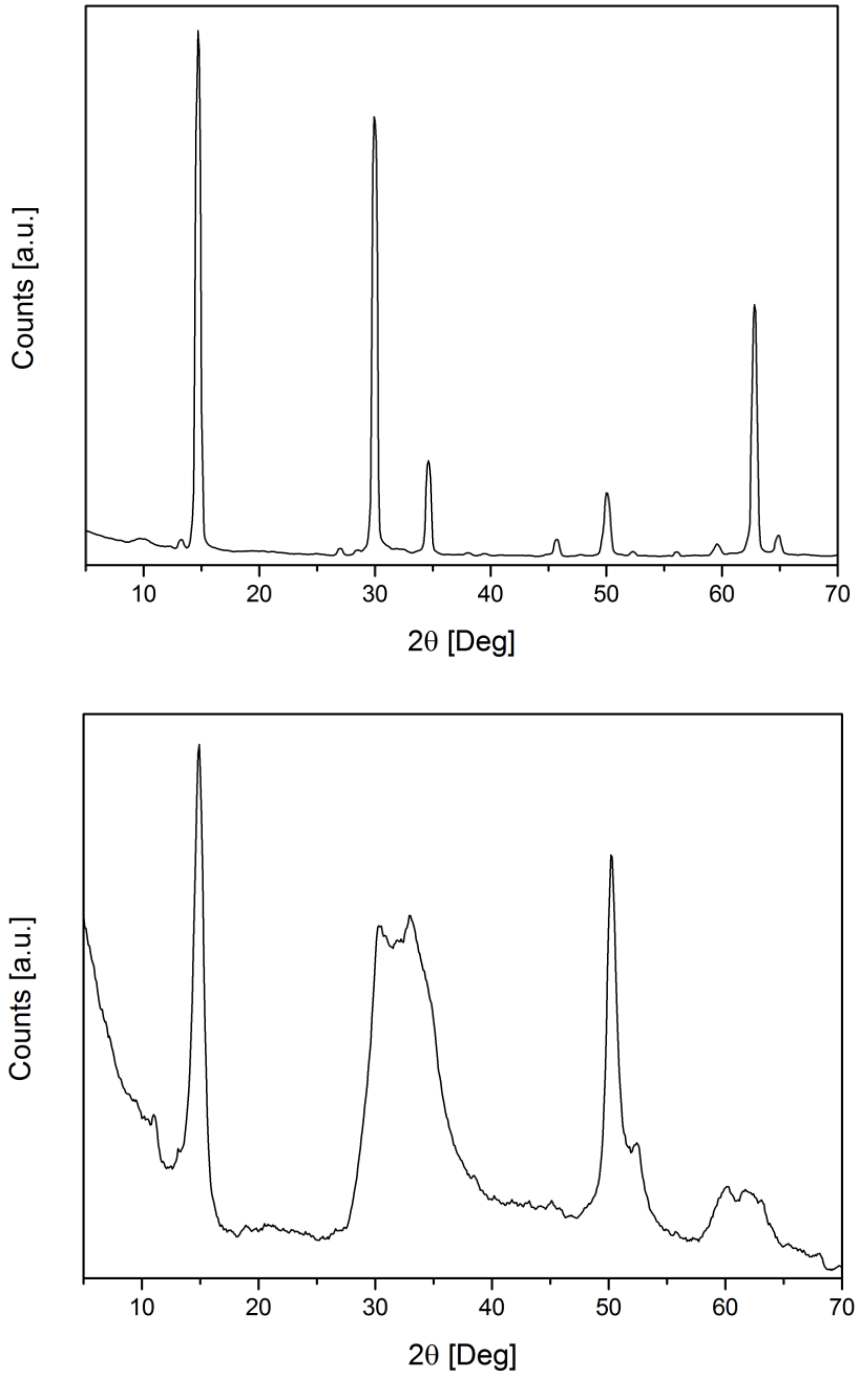

Figure 2.4. Powder XRD patterns of $MgCl_2$(CD) before (top) and after (bottom) physical activation by planetary ball-milling.

According to Giunchi and Allegra[6], the average dimensions of the crystallites along the **c** and **a** axes (<L_c> and <L_a>, respectively) can be estimated from the full widths at half height of the 003 (2θ ~15.0°) and 110 (2θ ~50.1°) reflections (I_1 and I_2, respectively) according to Eqs. 2.1 and 2.2, which are customized versions of the well-known Scherrer formula[6]:

$$\langle L_c \rangle = {}^{2\boldsymbol{c}}\!/_{3\gamma} \qquad \text{Eq. 2.1}$$

$$\langle L_a \rangle = {}^{\boldsymbol{a}}\!/_{\alpha} \qquad \text{Eq. 2.2}$$

The values of γ and α for a given sample can be estimated from $\{I_1,\alpha\}$ and $\{I_2,\gamma\}$ correlation plots, as provided by the same Authors[6] and shown in Figure 2.5.

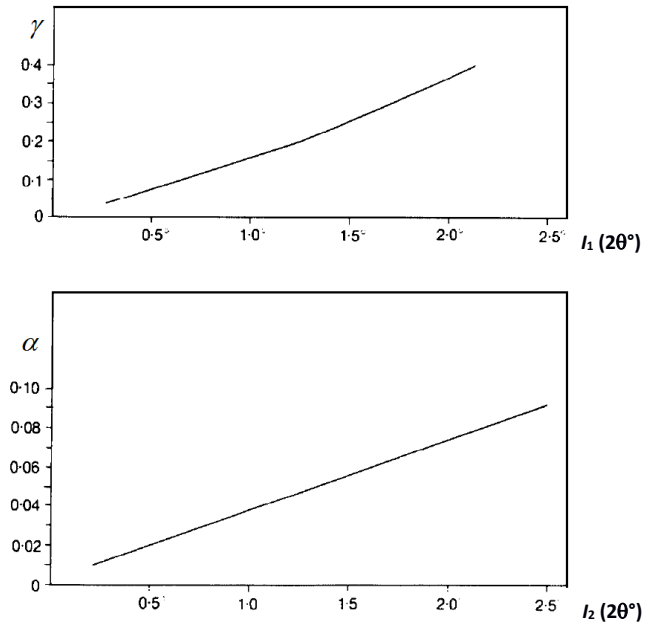

Figure 2.5. $\{I_1,\alpha\}$ and $\{I_2,\gamma\}$ correlation plots (Eqs 2.1 and 2.2).[6]

By applying this method to the spectra of activated $MgCl_2$(CD) and $MgCl_2$(PD), we calculated the $<L_a>$ and $<L_c>$ values reported at entries 1 and 2 of Table 2.1. At odds with what is observed for large(r) $MgCl_2$ crystals, which feature a platelet morphology due to exfoliation along the weakly bound basal planes of adjacent structural layers, both samples would have similar crystallite sizes (≈15 nm) parallel and perpendicular to the basal planes. A possible explanation is that lateral crystallite terminations in these samples were stabilized by H_2O molecules adsorbed upon manipulation downstream of the drying process. We will come back to this point later.

2.2 Preparation of $MgCl_2/TiCl_4$ and $MgCl_2$/LB model adducts

Planetary ball-milling was also used to prepare $MgCl_2/TiCl_4$ and $MgCl_2$/ID model adducts (see Appendix A-2 for experimental details). Aliquots of $MgCl_2$(CD) were co-milled with a certain amount of $TiCl_4$, or an ID of industrial relevance (Figure 2.6), namely 2,2-dimethyl-1,3-dimethoxypropane (**Do1**), 9,9-bis(methoxymethyl)-9*H*-fluorene (**Do2**), or diisobutylphthalate (**Do3**).[1] For all adducts, the average size of the crystallites was determined by powder XRD, with the same procedure described in the previous section for neat activated $MgCl_2$. The results are reported at entries 3-12 of Table 2.1.

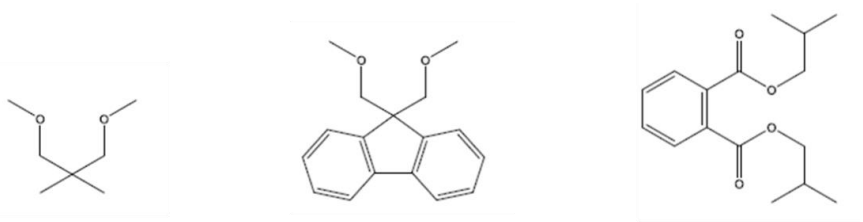

Figure 2.6. Chemical structures of 2,2-dimethyl-1,3-dimethoxypropane (**Do1**), 9,9-bis(methoxymethyl)-9*H*-fluorene (**Do2**), and diisobutylphthalate (**Do3**)**.**

Table 2.1. Average dimensions of the primary particles (estimated by powder XRD) for physically activated samples of $MgCl_2$, $MgCl_2/TiCl_4$, and $MgCl_2$/LB (see text).

Entry	Sample	*n* (Adsorbate) / *n* (Mg), %	$\langle L_c \rangle$, nm	$\langle L_a \rangle$, nm
1	$MgCl_2$(CD,M)		13.0	12.6
2	$MgCl_2$(PD,M)		14.6	16.1
3	$MgCl_2$/**$TiCl_4$**	4.3	6.3	7.9
4	$MgCl_2$/**Do1**	1.2	9.7	10.8
5		4.0	4.2	7.7
6		6.2	3.5	6.1
7		10.0	2.8	4.4
8	$MgCl_2$/**Do2**	2.5	5.0	8.4
9	$MgCl_2$/**Do3**	2.0	7.0	10.1
10		2.1	7.3	7.8
11		6.3	n.a.*	7.8
12		6.7	n.a.*	3.9

* Not available (average particle size could not be determined because the powder XRD peaks were too broad)

All adducts featured smaller crystallites than neat $MgCl_2$, the more so the greater the Adsorbate/Mg mole ratio. $\langle L_a \rangle$ and $\langle L_c \rangle$ values below 10 nm were estimated, and once again no clear anisotropy in crystallite morphology was observed. Some adducts would be close to the monolayer state (see in particular entries 11 and 12 of Table 2.1).

2.3 The question of adsorbed water

2.3.1 IR characterizations

Powder XRD analysis of a given $MgCl_2$ sample can rule out the presence of hydrated $MgCl_2.nH_2O$ phases, but gives no indications of the possible presence of adsorbed water decorating lateral crystallite terminations. In the previous section, indirect evidence that such water may indeed be present was discussed. Aiming to obtain direct information on the question, we characterized several samples of Table 2.1 by IR spectroscopy (in collaboration with the group of Prof. Christophe Copéret at ETH Zurich). This approach is extremely sensitive, although quantitations are difficult.

Figures 2.7-2.9 show Attenuated Total Reflection Fourier Transform IR (ATR-FTIR) spectra of neat unmilled $MgCl_2$(CD) and $MgCl_2$(PD) samples, physically activated ones ($MgCl_2$(CD,M) and $MgCl_2$(PD,M); entries 1 and 2 of Table 2.1), $MgCl_2$/**Do1** adducts (entries 4 and 6 of Table 2.1), and $MgCl_2$/**Do3** adducts (entries 9 and 11 of Table 2.1). In all cases, characteristic bands were observed around 3500 cm^{-1} and 1600 cm^{-1}, which can be assigned to the stretching and bending of surface -OH groups, respectively.

Interestingly, Figure 2.7 shows that the band around 3500 cm^{-1} was narrower for unmilled neat $MgCl_2$ samples than for physically activated ones. This suggests that in the former the -OH groups were (more) far apart (possibly isolated).

The spectra also featured a band around 700 cm^{-1}, which is compatible with the bending adsorption of Mg-O-Mg structures. These may be traced to the reaction of chemisorbed water with the underlying $MgCl_2$ surface at the high temperature (T > 150°C) reached in the mill jar during the energy-intensive milling process or, in the specific case of $MgCl_2$(PD) and $MgCl_2$(PD,M), upon

exposure to the hot N_2 flow. This suggests that caution is mandatory when heating, deliberately or inadvertently, $MgCl_2$ samples prior to catalysis-related studies.

Other bands around 1250 and 600 cm^{-1} could not be assigned.

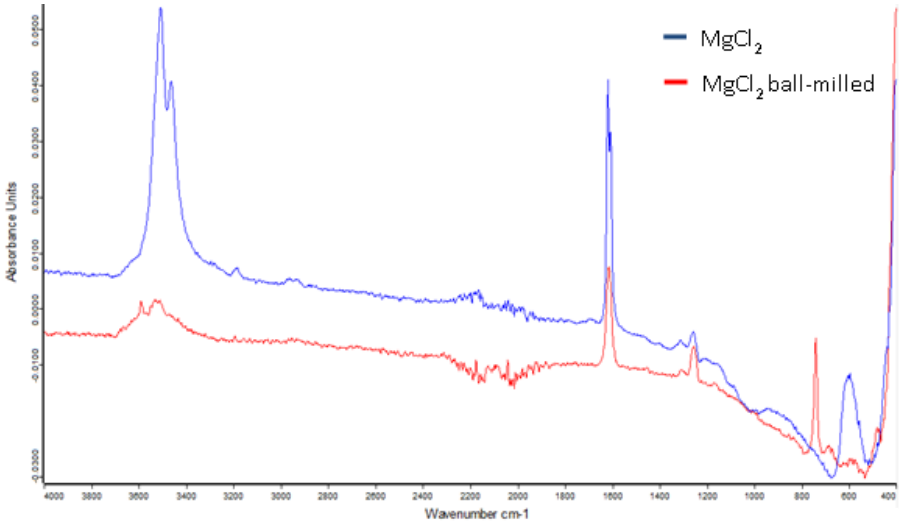

Figure 2.7. ATR-FTIR spectra of neat $MgCl_2$ before (blue trace) and after (red trace) physical activation by planetary ball milling.

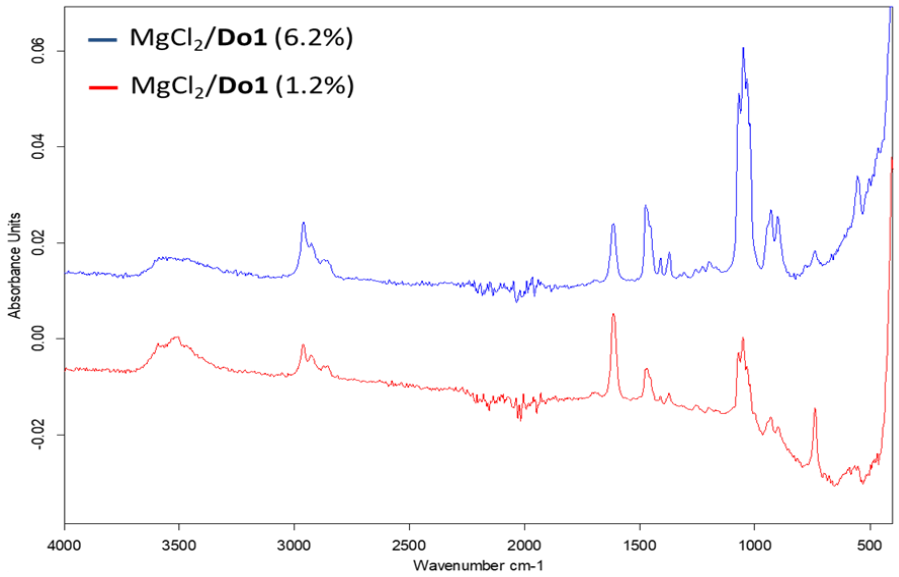

Figure 2.8. ATR-FTIR spectra of $MgCl_2$/**Do1** adducts at different donor loadings (see text and Table 2.1).

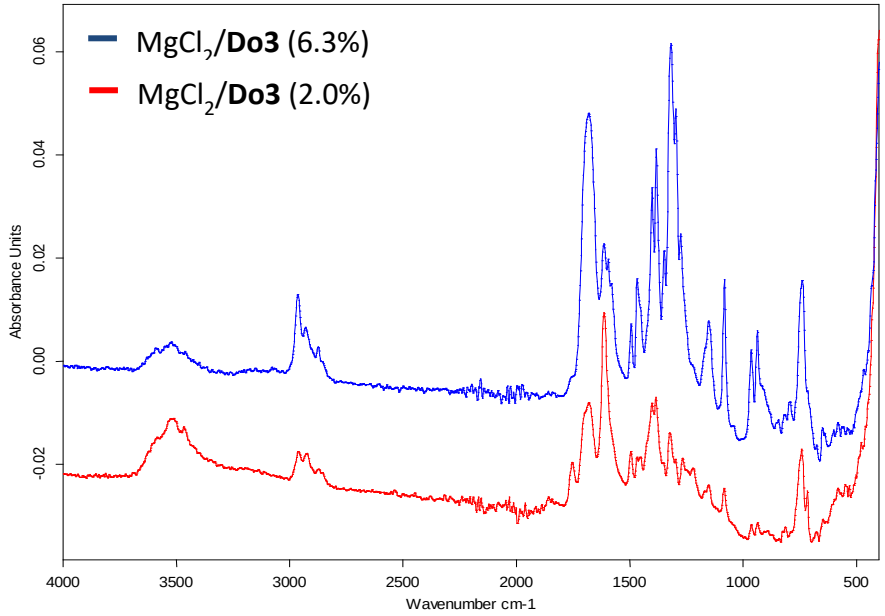

Figure 2.9. ATR-FTIR spectra of $MgCl_2$/**Do3** adducts at different donor loadings (see text and Table 2.1).

A variable-temperature (VT) FTIR characterization of the unmilled $MgCl_2$(PD) sample in the range of 25 to 300°C under vacuum (~10^{-4} atm) indicated that a temperature as high as 300°C must be reached in order to observe the disappearance of the characteristic -OH bands (Figure 2.10). Part of the adsorbed water reacted with the $MgCl_2$ surface, as is indicated by the clear Mg-O-Mg bending peak. Notably, upon exposure of the thus obtained dry sample to the Argon atmosphere of a high-performance glovebox, water was rapidly and progressively re-adsorbed, as further ATR-FTIR spectra demonstrated (Figure 2.11); it was striking to detect the –OH bands after a one-minute exposure only! Clearly, all this must be taken into account when carrying out surface science studies of $MgCl_2$, even on samples with low surface areas.

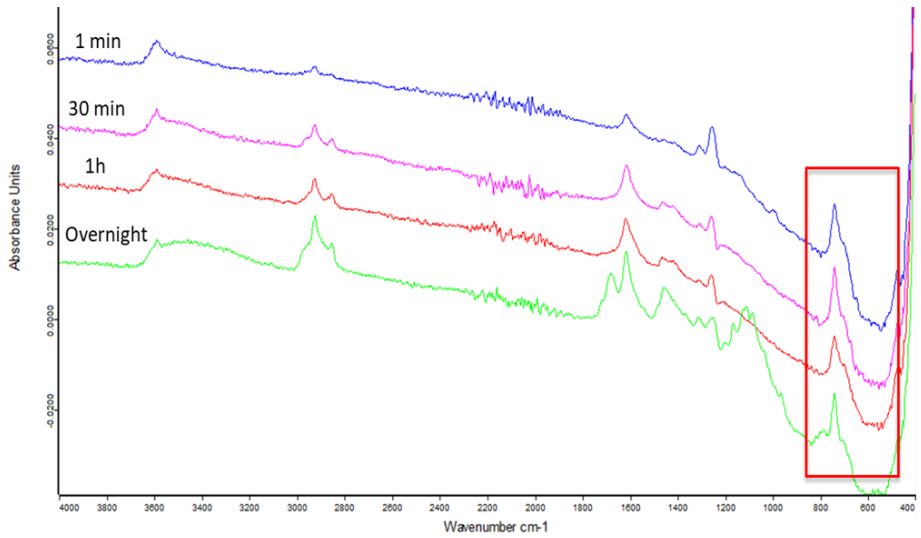

Figure 2.10. VT-FTIR spectra of the unmilled $MgCl_2$(PD) sample (see text).

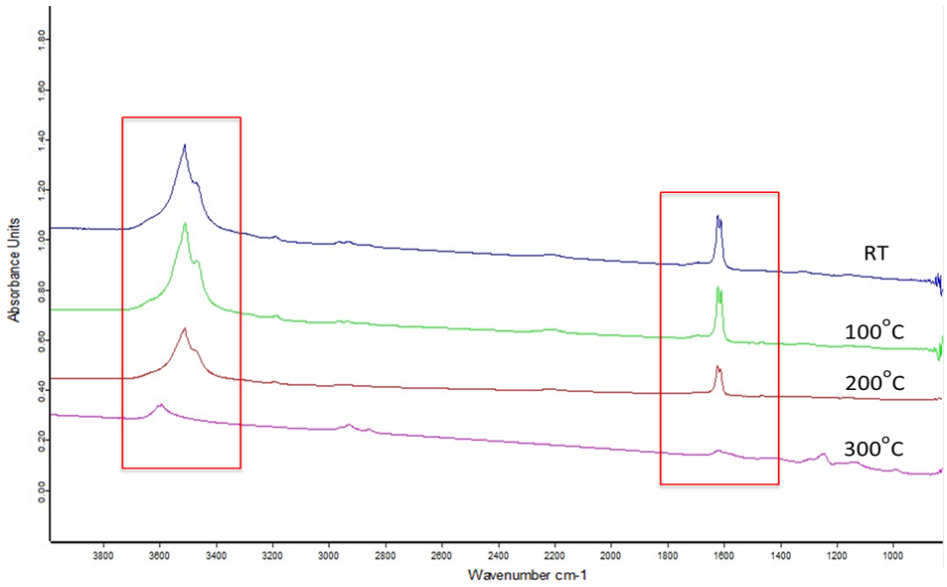

Figure 2.11. Water re-uptake by the unmilled $MgCl_2$(PD) sample as obtained by exposure to 300°C in a vacuum inside the IR cell, upon exposure to the Argon atmosphere of a high-performance glovebox, as monitored by VT-FTIR (see text).

2.3.2 Determinations of total proton content by solid-state ^1H NMR spectroscopy

As noted above, quantifying the water content of a $MgCl_2$ sample by IR spectroscopy is problematic. ^{1}H NMR, on the other hand, is a (more) quantitative spectroscopy. In this section, we report on solid-state ^{1}H NMR measurements (carried out in collaboration with the research group of Prof. Arno Kentgens at Radboud Universiteit Nijmegen) aimed to quantify the total proton content of $MgCl_2$(CD), $MgCl_2$(PD), $MgCl_2$(CD,M), and $MgCl_2$(PD,M) samples.

For all samples, static Hahn-echo ^{1}H NMR spectra at 7.1 T featured a clear proton signal. In the case of chemically dried samples, this had the distinctive shape of a Pake doublet[7] (Figure 2.12), with two ‘horns’ at around ±18 kHz,

and two shoulders/feet at around ±35 kHz. The appearance of a Pake doublet is caused by dipolar couplings by an isolated spin pair; in the case of interest here, this points to the coupling between the two protons of isolated adsorbed water molecules. The narrower lines (and the disappearance of the Pake doublet) in the spectra of physically dried samples, on the other hand, suggests that the protons in such samples were either more mobile, or more isolated compared to those in chemically dried ones; an educated guess is that these protons belong to surface hydroxyl groups. By peak integration, water contents were estimated to be as reported in Table 2.2.

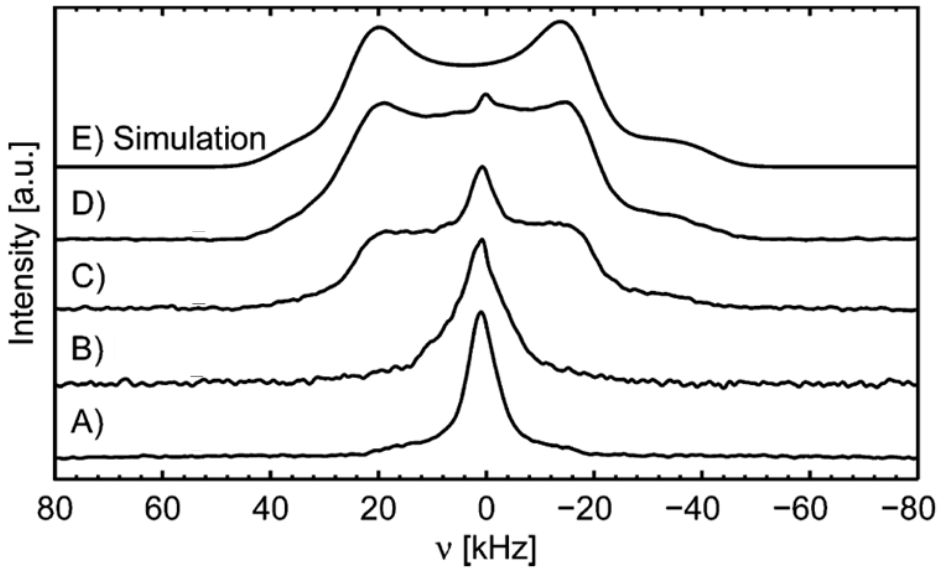

Figure 2.12. Experimental static Hahn-echo ^{1}H NMR spectra obtained at 7.1 T of (A) $MgCl_2$(CD,M), (B) $MgCl_2$(CD), (C) $MgCl_2$(PD,M), (D) $MgCl_2$(PD**)**, and (E) simulation of the Pake doublet for an isolated proton pair with r_{H-H} = 1.65 Å, 20 ppm of Chemical Shift Anisotropy (CSA), and 10 kHz Gaussian line broadening.

Table 2.2. Water contents of the analyzed samples, as measured by solid state ^{1}H NMR.

Sample	Water content (mol% wrt Mg)
$MgCl_2$(CD)	3.5
$MgCl_2$(PD)	1.0
$MgCl_2$(CD,M)	5.5
$MgCl_2$(PD,M)	4.5

To better elucidate the nature of the proton signal we carried out Magic Angle Spinning (MAS) experiments in order to resolve isotropic chemical shifts (Figure 2.13). The two chemically dried samples featured proton signals around 5 ppm, compatible with molecular H_2O. Physically dried samples, on the other hand, gave a sharp(er) signal around 1.7 ppm which may well correspond to −OH groups.[8] This would be consistent with the ATR-FTIR characterizations (§ 2.3.1).

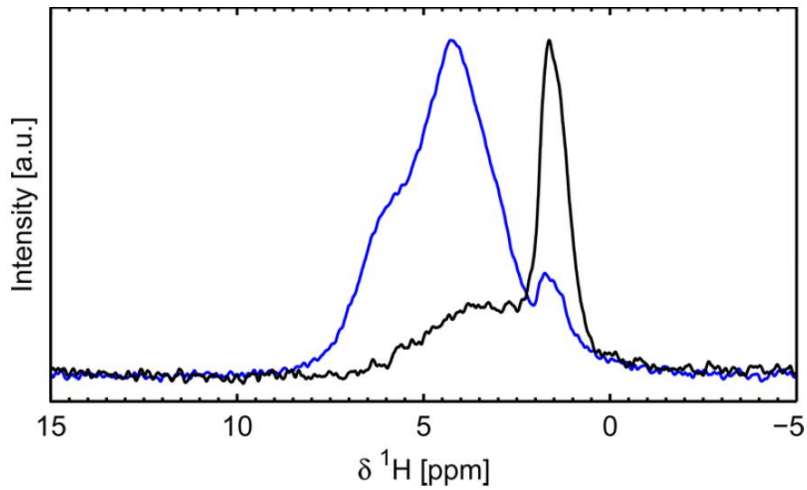

Figure 2.13. 50 kHz MAS ^{1}H NMR spectra of $MgCl_2$(CD,M) (blue trace) and $MgCl_2$(PD,M) (black trace) at 20 T.

The water contents of Table 2.2 are very high, and suggest that, in the analyzed samples, lateral terminations of $MgCl_2$ crystallites were practically saturated by adsorbed molecular or dissociated water. Also in view of the (ATR) FTIR results, an educated guess is that said water was re-gained by the samples upon manipulation downstream of the drying process.

In line with the above interpretation, the solid state ^1H NMR spectra of $MgCl_2$/LB adducts did not show clear evidence of adsorbed water, despite the lower average particle size compared with neat $MgCl_2$. We trace this to the shielding effect of chemisorbed LB molecules, hampering water diffusion to the surface. This finding is important, as it suggests that studying $MgCl_2$ adducts is reasonably safe because the risk of flawed results due to the presence of adventitious water is low.

2.4 Summary and conclusions

Two methods for the preparation of dry $MgCl_2$ samples were tested and found to be satisfactory. The first one (chemical method) consists of a treatment of $MgCl_2$ in aliphatic hydrocarbon slurry with $SiCl_4$, while the second (physical method), features in prolonged exposure to a flow of dry N_2 at 250°C.

Preventing water from re-adsorbing onto neat activated samples, prior to FTIR and ^1H solid-state NMR characterizations, is practically impossible under non-UHV conditions (UHV = Ultra High Vacuum), even when operating inside a high performance glovebox. On the contrary, in activated $MgCl_2$/ID adducts, only negligible amounts of water were found, despite the lower average particle size compared with neat $MgCl_2$; we trace these findings to the ‘shielding’ of the surface by chemisorption of the ID.

References

[1] Moore, E. P., Jr. (Ed.) *Polypropylene Handbook: Polymerization, Characterization, Properties, Processing, Applications*; Hanser Publishers: Munich, 1996.

[2] Chen, Y.; Li, C. P.; Chen, H.; Chen, Y. *Sci. Technol. Adv. Mater.* **2006,** *7*, 839.

[3] Sugimoto, K.; Dinnebier, R. E.; Hanson, J. C. *Acta Cryst. B* **2007,** *63*, 235.

[4] Partin, D. E.; O'Keeffe, M. *J. Solid State Chem.* **1991,** *95*, 176.

[5] Auriemma, F.; De Rosa, C. *J. Appl. Crystallogr.* **2008,** *41*, 68.

[6] Giunchi, G.; Allegra, G., *J. Appl. Crystallogr.* **1984,** *17*, 172.

[7] Pake, G. E. *J. Chem. Phys.* **1948,** *16*, 327.

[8] (a) Phillips, B. L.; Burnley, P. C.; Worminghaus, K.; Navrotsky, A. *Phys. Chem. Miner.* **1997** *24*, 179. (b) Xue, X.; Kanzaki, M. *J. Phys. Chem. B* **2007**, *111*, 13156. (c) Xue, X.; Kanzaki, M.; Shatskiy, A. *Am. Mineral.* **2008,** *93*, 1099. (d) Xue, X.; Kanzaki, M. *J. Am. Ceram. Soc.* **2009**, *92*, 2803.

Appendix A-2

Chemicals

'Dry' crystalline $MgCl_2$ (in its stable α polymorphic modification) was kindly donated by LyondelBasell. $SiCl_4$ was purchased from Fluka (> 99% purity). Heptane and pentane (Romil HPLC grade) were purified by passing them through activated-Cu and A4-molecular-sieves columns in an MBraun SPS-5 unit (final concentration of O_2 and H_2O < 1 ppm).

All air-sensitive compounds were handled under argon, using Schlenk techniques and/or an MBraun LabMaster 130 glovebox (water and oxygen levels < 1 ppm_v).

$MgCl_2$ chemical drying protocol

$MgCl_2$ aliquots (5-15 g) were suspended in 60-70 *m*L of heptane inside a (custom-made) Pyrex® reactor equipped with a siphon and a sintered-glass bottom filter, connected to a Schlenk line operating under flowing Argon (purity 5.0 grade).

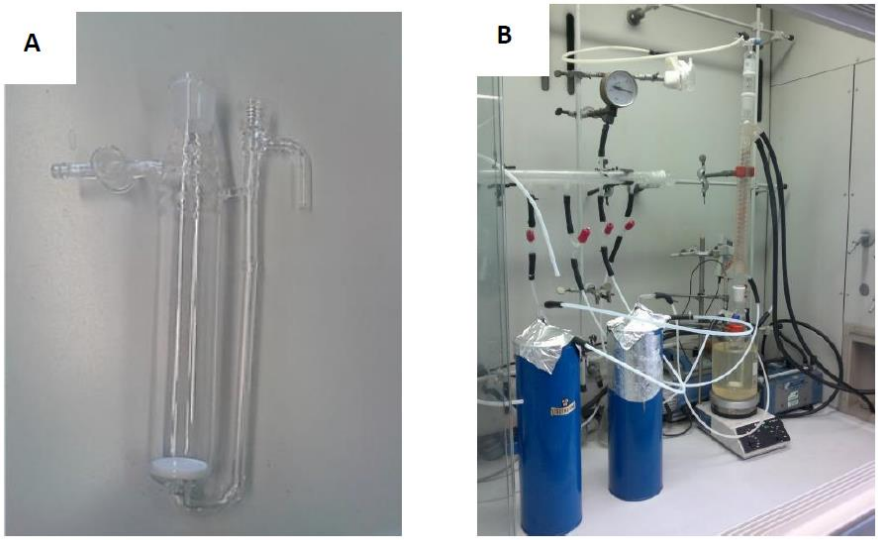

Figure A-2.1. The Pyrex reactor used for the $MgCl_2$ chemical drying protocol (**A**), and the overall setup connected to a Schlenk line (**B**). All components had been kept at 135 °C overnight prior to use.

A proper amount (5-35 mL) of $SiCl_4$ was added, and the slurry was subjected to vigorous magnetic stirring at 55-65°C. After a proper time (4-5 h), the liquid phase was siphoned out through the bottom filter under vacuum. The solid was then washed with one or more aliquots of dry pentane (60-70 *mL*) at room temperature under vigorous stirring, and finally dried under vacuum at 100°C overnight. The samples were then recovered inside a glove-box.

$MgCl_2$ physical drying protocol

$MgCl_2$ aliquots were treated at 250 °C in a flow of dry N_2 (ultra-high purity grade) for 6 hours (procedure performed by N. Friederichs and T. van Kessel; SABIC Research Center in Geleen).

Planetary ball-milling set-up and protocol

After drying, the samples (neat or in the presence of $TiCl_4$ of a LB) were physically activated by means of a Retsch® PM-100 planetary ball mill (Figure A-2.2). In this setup, the grinding jar is positioned eccentrically on the sun wheel of the planetary ball mill. The direction of motion of the sun wheel is opposite to that of the grinding jar, (1:-2 ratio). The speed of the sun wheel is electronically controlled in the range of 100 to 650 rpm. The grinding balls in the jar are subjected to superimposed rotational motions; the difference in speed between the balls and the grinding jar produces an interaction between frictional and impact forces, which releases high dynamic energy.

Figure A-2.2. Retsch PM-100 planetary ball mill (on the right, different options of the jar and the grinding balls).

Operating inside a glovebox, the samples (2-12 *g*) were loaded inside an air-tight and chemically inert ceramic jar made with ZrO_2 stabilized with Y, along with 87 *g* of grinding ceramic balls (3 mm diameter). The jar was then transferred to the mill. The rotational speed was set to the maximum value (650 rpm), and the rotational motion was inverted at 20 min intervals to prevent as far as possible encrustations on the inside walls of the jar. A milling time of 6-8 h turned out to be adequate to reach the lower-limit crystallite size

(at longer times, the primary particles tend to coalesce). At the end of the milling process, the samples were collected in a glove-box. In case of $MgCl_2$/LB adducts, the powders were suspended in 30 mL of heptane, further washed with aliquots of heptane and pentane and, finally dried under high-vacuum overnight.

Powder XRD characterization

All samples were characterized by powder XRD using a Philips PW 1830 diffractometer, equipped with a custom-made airtight cell with PVC windows, able to maintain a static atmosphere with negligible O_2 and moisture contamination for at least 8 h. The cell was loaded in a glove box and transferred to the diffractometer, where the diffraction profile was collected using Ni-filtered CuK_α radiation (30 mA, 35 KV) with a step scanning procedure (2ϑ range between 5° and 70°, 0.1° step, 20 *s* counting time per step).

EDS-TEM characterization

Upon $MgCl_2$ chemical drying treatment, $SiCl_4$ reacts with adsorbed water forming SiO_2. EDS-TEM measurements were performed to investigate the distribution of Si in the product. Unfortunately, it was not possible to avoid exposure to air during transfer of the sample into the JEOL 1010 TEM; this caused some hydration and coagulation of the fine particles. Moreover, the copper grid (size ~2 μm) used for the analysis produced background signals in the Si EDS analysis. Nevertheless, the experiments did show that Si was finely dispersed in the products as nanometer-sized spots. Si content did not correlate with the Mg or Cl distribution. Therefore, it can be concluded that silicon was

not adsorbed on the $MgCl_2$ particles, but rather formed a separate SiO_2 phase (Figure A-2.3).

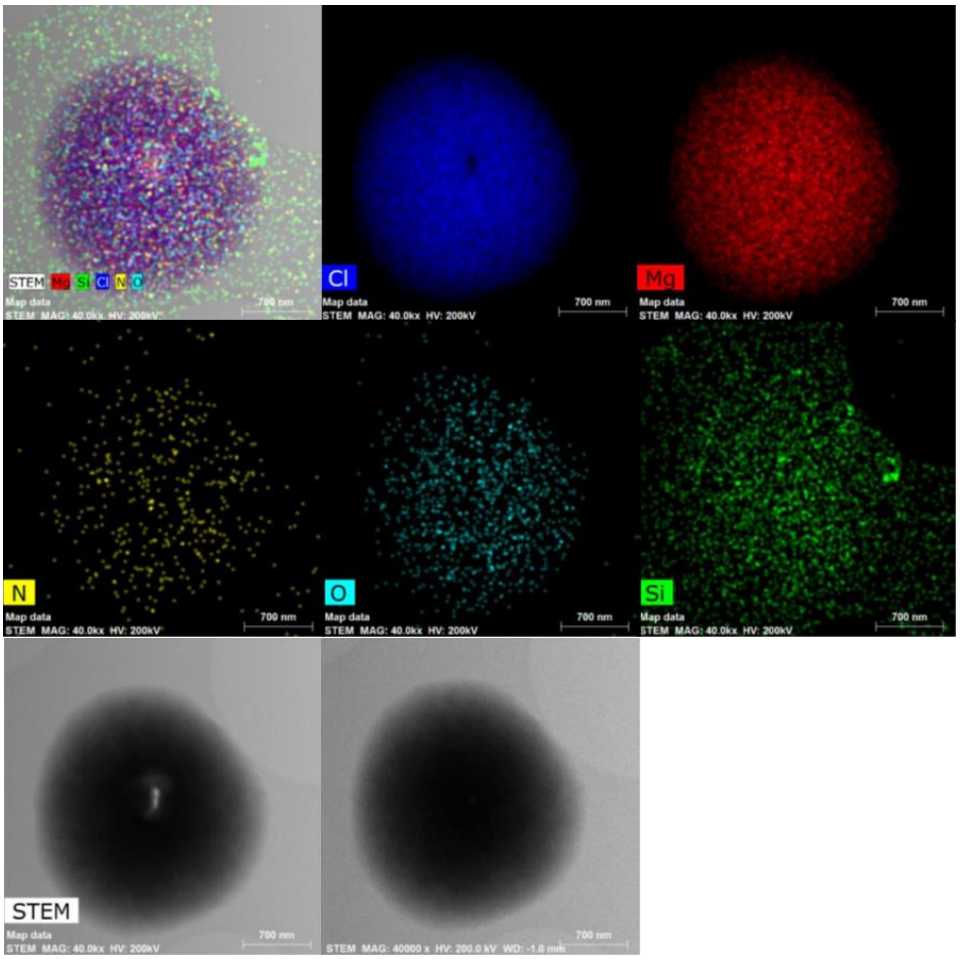

Figure A-2.3. EDS-TEM images of a $MgCl_2$ sample after chemical drying and physical activation.

IR spectroscopy characterizations

IR spectra were recorded in transmission and Attenuated Total Reflectance (ATR) mode on a Nicolet 6700 FT-IR spectrophotometer, contained inside a

glovebox operating under Argon (research group of Prof. C. Copéret, ETH Zurich).

Solid-state ^{1}H NMR characterizations

All measurements were performed at Radboud Universiteit Nijmegen (research group of Prof. A. Kentgens), using a 300 MHz spectrometer (7.04 T) equipped with a home-built static probe without proton background. Either 4.0 mm rotors or glass tubes were used. Glass tubes were filled with the $MgCl_2$ sample of interest inside a glovebox, and subsequently flame-sealed to avoid contamination during measurements. The proton intensity was quantified against adamantane. Full T_2 decay curves were obtained for each sample, so as to account for T_2 relaxation effects. The T_2 curves were fitted, and the pre-exponential factor was determined as the quantitative intensity at $\tau = 0$. MAS and fast MAS proton measurements were performed at 20 T (850 MHz) using 4.0 and 1.2 mm triple-resonance Varian T3MAS probes. To make sure that the proton signal and intensity were not misinterpreted, the rotor background was checked, and/or the rotors were previously cleaned with ethanol.

Chapter 3. Solid-state (Q)NMR and DFT-D investigations of $MgCl_2$/LB adducts

3.1 Introduction

All industrial Ziegler-Natta precatalysts for iPP production contain a LB (the so-called Internal Donor, ID) in significant amounts (10-20 wt-%). As was noted in Chapter 1, this is mandatory to achieve a high activity and stereoselectivity.[1,2] Well-working ID include aromatic monoesters (e.g. ethyl benzoate), aromatic diesters (e.g. dialkylphthalates), aliphatic diesters (e.g. diethyl-2,3-dialkylsuccinates), and 1,3-diethers (e.g. 2,2-dialkyl-1,3-dimethoxypropanes). A second LB (the so-called External Donor, ED, which almost invariably is an alkoxysilane) is usually added to the R_3Al cocatalyst, to further enhance the stereoselectivity.[1,2] Although the role of these molecules is still under debate, practically all aspects of catalyst performance depend on the choice of the ID/ED pair. The current view is that LB molecules chemisorbed on the surface of $MgCl_2$ at non-bonded contact with the active Ti species modulate the active pocket by means of steric and (possibly) electronic effects, similarly to ancillary ligands in molecular catalysts.[3]

It has been proposed, mainly based on computational studies, that some ID have a more or less strong preference for certain $MgCl_2$ crystal terminations. In particular, 1,3-diethers are believed to bind much more strongly to 4-coordinated Mg atoms (e.g., exposed on $MgCl_2$(110) and the alike)[4] in chelating mode (Figure 3.1-A). Others, instead, like phthalates and succinates, seem to adsorb rather indiscriminately on 5-coordinated and 4-coordinated Mg[4.5], because they can adopt either a chelating or a bridging mode (Figure 3.1-B, C and D).[4] As was recalled in Chapter 1, chemically activated Ziegler-Natta precatalysts are formed by titanation from precursor compounds in the

presence of the ID, which implies that, if the donor favors certain $MgCl_2$ surfaces, it can steer crystal morphology.

In this part of the work, we aimed to achieve a deeper insight into the coordination mode(s) of three industrially relevant ID, namely 2,2-dimethyl-1,3-dimethoxypropane (**Do1**), 9,9-bis(methoxy-methyl)-9*H*-fluorene **(Do2**), and diisobutylphthalate (**Do3**) (Figure 3.2), by means of advanced solid-state (Quadrupolar) NMR measurements integrated with state-of-the-art DFT-D calculations. $MgCl_2$/ID model adducts were prepared ad-hoc for this study (Chapter 2).

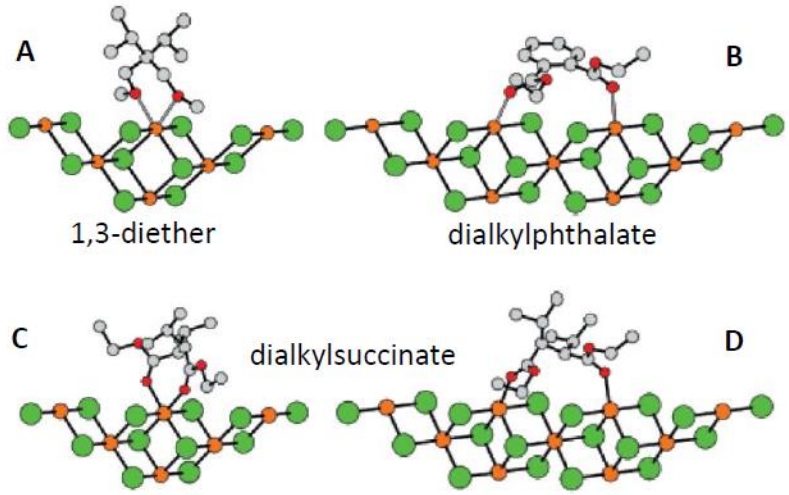

Figure 3.1. Schematic representations of binding modes for different ID on a $MgCl_2$(110)-like surface.[4]

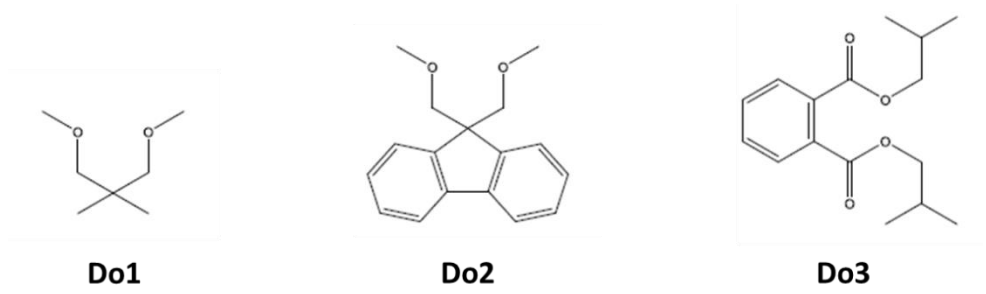

Figure 3.2. Chemical structures of 2,2-dimethyl-1,3-dimethoxypropane (**Do1**), 9,9-bis(methoxymethyl)-9*H*-fluorene (**Do2**), and diisobutylphthalate (**Do3**)**.**

3.2 Quadrupolar parameters: theory and experiment

3.2.1 Introductory remarks

The electric field gradient (EFG) measures the rate of change of the electric field at an atomic nucleus generated by the electronic charge distribution and the other nuclei. The EFG couples with the nuclear electric quadrupole moment of quadrupolar nuclei (i.e. atoms with spin quantum number greater than ½) to generate an effect (quadrupolar interaction) which can be measured using several spectroscopic methods, such as NMR, ESR, Mössbauer spectroscopy, etc. The EFG is non-zero only if the charges surrounding the nucleus violate cubic symmetry and therefore generate an inhomogeneous electric field at the position of the nucleus.

Valuable structural information can be gained by evaluating the quadrupolar interaction, which is characterized by the quadrupolar coupling constant (C_Q) and the asymmetry parameter (η), defined as follows:

$$C_Q = \frac{eQV_{zz}}{h} \qquad \text{(Eq. 3.1)}$$

$$\eta = \frac{V_{xx} - V_{yy}}{V_{zz}} \qquad \text{(Eq. 3.2)}$$

where *e* is the elementary charge of the electron, Q is the electric quadrupolar momentum of a given nuclei, *h* is the Planck constant and V_{xx}, V_{yy} and V_{zz} are the principal tensor components of the EFG in the principal axis system, with $|V_{zz}| \geq |V_{yy}| \geq |V_{xx}|$. Both parameters are highly sensitive to the coordination environment, and combined with chemical shifts, can help to determine the local structure of surface sites.[6]

3.2.2 DFT calculations of ^{25}Mg and ^{35}Cl quadrupolar parameters

In this work, quadrupolar parameters were calculated by means of two well-known periodic ab-initio software packages, namely the Vienna Ab-Initio Simulation Package (VASP; version 5.3.5[7]), which is based on plane-wave basis sets, and the CRYSTAL09 suite[8], which uses atom-centered (Gaussian) basis sets.

Preliminarily, we carried out calculations of the lattice constants, as well as ^{25}Mg and ^{35}Cl quadrupolar parameters, for an α-$MgCl_2$ crystal. Full relaxation of the unit cell (cell parameters and atomic coordinates) was allowed. EFG calculations were performed at PBE[9] level with the projector augmented-wave method (PAW)[7] at increasing energy cut-offs and using various dispersion correction methods, namely Grimme's D2 and D3 corrections,[10] and the VdW-DF[11] functional as implemented in VASP. The calculations were then repeated using CRYSTAL09 at B3LYP[12]/TZVP[13] level. The results are compared between them and with experimental values in Table A-3.1 of Appendix A-3. For the VASP calculations, the best agreement with experiment for both lattice constants and quadrupolar parameters was achieved by including Grimme's D3 dispersion correction, already at a 400 eV cut-off; this protocol was then used for all subsequent calculations.

In the case of model adducts, surfaces were generated using the slab method, with a separation of 10-15 Å between the slabs. Geometry optimizations were carried out holding the lattice parameters constant. With the CRYSTAL09 package, geometry optimizations and EFG calculations were carried out at the B3LYP level of theory using the TZVP basis set[13] for Mg, Cl and Ti, and Ahlrichs VTZ plus polarization basis set[14] for the C, H and O atoms (optimized in a previous work[15]).

Next, we calculated ^{25}Mg and ^{35}Cl quadrupolar parameters for a $MgCl_2(110)/TiCl_4$ model adduct with epitaxially chemisorbed $TiCl_4$ (Figure 3.3), and various $MgCl_2$(*hkl*)/**Do1** and $MgCl_2$(*hkl*)/**Do3** model adducts, with the donor molecules bound either in the bridging or in the chelating mode (Figure 3.4). The results are summarized in Tables 3.2 and 3.3. Calculated values for the naked $MgCl_2$ surfaces are reported for comparison in Table A-3.2.

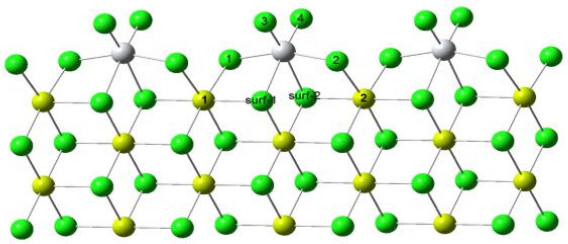

Figure 3.3 Optimized structures of a $MgCl_2(110)/TiCl_4$ model adduct. (Mg atoms are colored in yellow, Cl atoms in green, Ti atoms in grey).

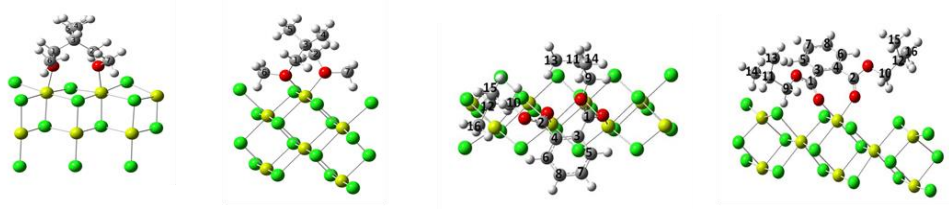

Figure 3.4. From left to right: optimized structures of $MgCl_2$(104)/**Do1**, $MgCl_2$(110)/**Do1**, $MgCl_2$(104)/**Do3** and $MgCl_2$(110)/**Do3** model adducts (see text). For the sake of clarity, the picture shows only selected surface atoms close to the donor molecules. (Mg atoms are coloured in yellow, Cl atoms in green, O atoms in red, C atoms in grey, H atoms in white).

Table 3.1. Calculated ^{35}Cl and ^{25}Mg C_Q (in MHz) and asymmetry parameters (η) for $MgCl_2$(110)/$TiCl_4$ at B3LYP/TZVP level of theory (see text and Figure 3.3).

	C_Q	**η**
Cl_{surf}–1	7.8	1.0
Cl_{surf}–2	7.8	1.0
Cl-1	-19.2	0.7
Cl-2	-19.2	0.7
Cl-3	-13.9	0.1
Cl-4	-14.0	0.1
Mg-1	2.2	0.8
Mg-2	2.2	0.8

Table 3.2. ^{35}Cl and ^{25}Mg C_Q (in MHz) and asymmetry parameters (η) for $MgCl_2$(*hkl*)/**Do1** and $MgCl_2$(*hkl*)/**Do3** adducts, calculated at PBE/PAW level using the VASP code and at B3LYP/TZVP level using the CRYSTAL09 code (see text and Figure 3.4).

QC software	Basis set	Nuclei	System	C_Q	η
VASP	plane waves	^{35}Cl	$MgCl_2$ 104/**Do1**	12.2	0.5
			$MgCl_2$ 110/**Do1**	14.5	0.5
		^{25}Mg	$MgCl_2$ 104/**Do1**	2.30	0.4
			$MgCl_2$ 110/**Do1**	3.52	0.8
		^{35}Cl	$MgCl_2$ 104/**Do3**	12.6	0.6
			$MgCl_2$ 110/**Do3**	14.6	0.5
		^{25}Mg	$MgCl_2$ 104/**Do3**	1.96	0.5
			$MgCl_2$ 110/**Do3**	2.69	0.6
CRYSTAL09	atom-centered	^{35}Cl	$MgCl_2$ 104/**Do1**	12.2	0.7
			$MgCl_2$ 110/**Do1**	14.9	0.5
		^{25}Mg	$MgCl_2$ 104/**Do1**	2.81	0.3
			$MgCl_2$ 110/**Do1**	3.42	0.7
		^{35}Cl	$MgCl_2$ 104/**Do3**	12.9	0.7
			$MgCl_2$ 110/**Do3**	13.5	0.3
		^{25}Mg	$MgCl_2$ 104/**Do3**	2.83	0.6
			$MgCl_2$ 110/**Do3**	4.33	0.8

Reassuringly, a good agreement was observed between VASP and CRYSTAL09 calculated parameters, despite the profound differences in the theoretical approach. In general, the results indicate that the presence of an adsorbate can produce significant and idiosyncratic effects on the quadrupolar parameters of the ^{25}Mg and ^{35}Cl nuclei in the underlying surface.

For the $MgCl_2(110)/TiCl_4$ adduct (Figure 3.3), the calculated C_Q for the surface Mg atoms is close to that in the bulk; this can be ascribed to the restored coordinative saturation. To some extent, the same applies to the surface Cl atoms labelled as $Cl_{surf\text{-}1}$ and $Cl_{surf\text{-}2}$, which underwent a decrease of C_Q from 16-18 MHz for the naked surface to 8-9 MHz. The asymmetry parameters of all such nuclei are close to 1. On the other hand, the remaining Cl atoms (Cl-1 to Cl-4) feature C_Q values in the range of 14 to 21 MHz, i.e. from slightly lower to even larger than those on naked $MgCl_2$ surfaces (Table A-3.2).

Concerning the $MgCl_2$/LB adducts (Figure 3.4), here too donor adsorption restored the coordinative saturation of the surface Mg atom(s) to which the donor was bound; indeed, the calculated C_Q was significantly reduced, and approached the bulk value. On the other hand, the surface Cl nuclei maintained quadrupolar parameters which are similar to those found for a naked surface, and thus appear to be rather insensitive to the presence of an adsorbate.

When the above is translated into predicted line widths in QNMR spectra, one should expect comparatively narrow lines for ^{25}Mg. Unfortunately, ^{25}Mg solid-state NMR is very challenging, mainly due to the low natural abundance of this nucleus, and therefore experimental validation of our calculations is still pending. Calculated C_Q values for ^{35}Cl, on the other hand, correspond to a line width of 400-800 kHz in experimental spectra recorded under static conditions, or 100-300 kHz under MAS conditions; this is larger than what can be observed experimentally with conventional techniques, especially because most of the signal arises from ^{35}Cl atoms in the bulk of the crystal, and the broader contributions of the nuclei on the surface, which represent a minority, fade into the background.

Even if our calculations suggest that the surface Cl sites cannot be directly observed, at least in samples at natural isotopic abundance, a useful (albeit indirect) observation came from the analysis of the intensity of ^{35}Cl QNMR spectra. As a matter of fact, ^{35}Cl (Hahn Echo) experimental spectra of activated $MgCl_2$ samples, with or without an adsorbate, showed a loss of signal intensity compared to unmilled $MgCl_2$ (Table 3.3) which correlates decently with average particle size $<L_a>$ as estimated in Chapter 2 (Figure 3.5). Intriguingly, $MgCl_2$/**Do1** adducts seem to deviate from this trend; indeed, despite a low particle size, such samples featured only a small intensity loss. This suggests that different donors can lead to different local $MgCl_2$ surface environments, which is potentially valuable for diagnostic studies. On the other hand, how to exploit this opportunity for practical purposes remains to be understood.

Table 3.3. Relative signal intensities in the solid-state ^{35}Cl NMR spectra of $MgCl_2$(/Adsorbate) samples. Based on the particle size measured by XRD (Chapter 2, Table 2.2), the fraction of surface Cl was estimated in the hypothesis of hexagonal particles.

Sample (*n* (Adsorbate) / *n* (Mg))	**Relative Signal Intensity**		**Estimated Fraction of Surface Cl**
	Static	**MAS**	
$MgCl_2$(CD)	100.0%	100.0%	
$MgCl_2$(CD,M)	96.8%	94.7%	6.0%
$MgCl_2$/**TiCl$_4$** (4.3%)	93.2%	91.4%	8.0%
$MgCl_2$ **Do2** (2.5%)	91.5%	88.6%	8.5%
$MgCl_2$/**Do1** (4.0%)	94.6%	92.7%	9.0%
$MgCl_2$/**Do1** (10%)	95.5%	92.8%	15%
$MgCl_2$/**Do3** (2.1%)	88.4%	86.3%	9.0%
$MgCl_2$/**Do3** (6.7%)	84.1%	80.4%	16%

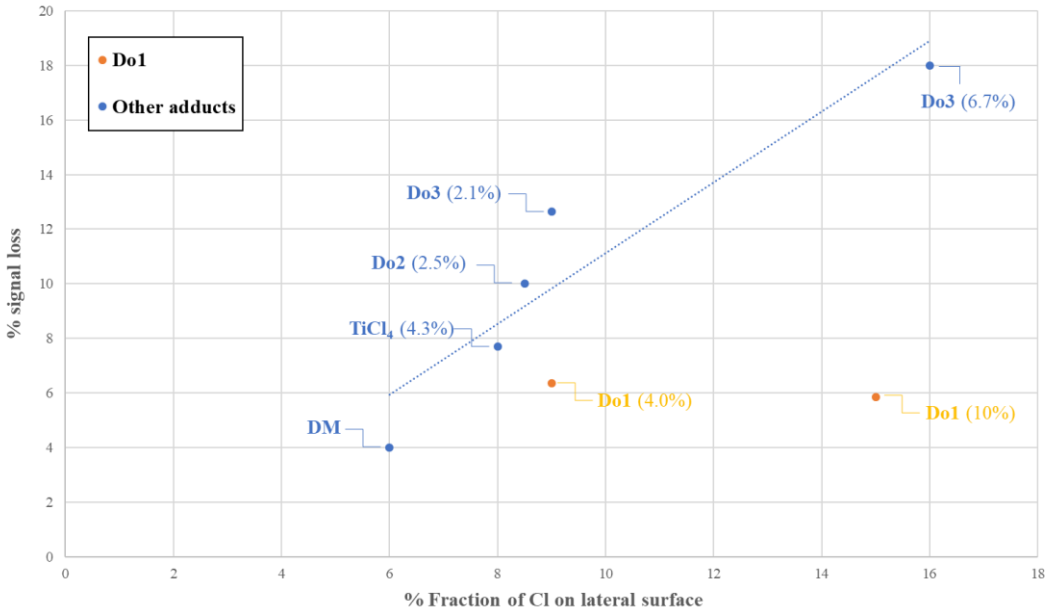

Figure 3.5. Correlation plot between relative signal intensity of solid-state ^{35}Cl NMR spectra and estimated fraction of surface Cl for different activated $MgCl_2$(/Adsorbate) adducts (data from Table 3.3).

3 .3 Solid-state ^{13}C NMR investigation of $MgCl_2$/LB adducts

3.3.1 Experimental solid-state ^{13}C NMR spectra

Industrially relevant ID are organic molecules, and therefore solid-state ^{13}C NMR spectroscopy can provide important information on donor adsorption mode(s) and, indirectly, on $MgCl_2$ surface environments. Several $MgCl_2$/**Do1**, $MgCl_2$/**Do2**, $MgCl_2$/**Do3** adducts, prepared as described in Chapter 2, were characterized by means of CPMAS ^{13}C NMR at Radboud Universiteit Nijmegen (research group of Prof. A. Kentgens; see Appendix A-3 for experimental details). Tables 3.4-3.6 compare the experimental ^{13}C chemical shifts of the donors in the adducts with those of the 'free' molecules in $CDCl_3$ solution (**Do1** and **Do3**), or in the solid state (**Do2**; this molecule is sparingly soluble in common NMR solvents). Typical CPMAS ^{13}C NMR spectra are shown in Figure 3.6.

Figure 3.6-A, in particular, compares the CPMAS ^{13}C NMR spectra of a $MgCl_2$/**Do2** adduct with that of the pure compound; the absence of narrow lines in the former indicates that 'all' donor molecules were strongly bound to the support. For the adsorbed molecule, the -OCH_2- (C-1, C-2) and -OCH_3 (C-16, C-17) signals underwent an important downfield shift ($\Delta\delta$ > 5 ppm); this is not surprising, considering that adsorption occurred via the ether O. Looking at the spectrum of the adduct in more detail, it can be noted that some resonances feature a fine structure: the quaternary carbon, in particular, has an asymmetric line shape that suggests multiple components, whereas two clear components can be recognized for the -OCH_2- and -OCH_3 resonances (Table 3.4).

Figure 3.6-B shows the solid-state spectra of two $MgCl_2$/**Do1** adducts at different donor loading. Both feature distinct resonances for the four

magnetically non-equivalent ^{13}C nuclei (Table 3.5). The quaternary carbon gave a rather sharp signal at 36.9 ppm; the other carbons produced significantly broader lines with at least two components. Here too, a downfield shift of over 5 ppm was observed for the -OCH_2- and -OCH_3 peaks of adsorbed **Do1** relative to the 'free' molecule in solution. Interestingly, the fine structure of the solid-state spectrum for the adduct at lower loading is better resolved and more complex. Part of the chemical shift values in Table 3.5 were obtained by means of peak deconvolution procedures (Figure A-3.2).

Finally, Figure 3.6-C shows the solid-state spectra of two $MgCl_2$/**Do3** adducts at different donor loadings. Aliphatic carbons gave relatively sharp peaks, whereas much broader peaks were observed for the aromatic, carbonyl and ester carbons; deconvolution of the carbonyl peak ended up with (at least) three components. Downfield shifts of over 5 ppm were observed for the -OCH_2- and the carbonyl ^{13}C nuclei, relative to the free molecule in solution (Table 3.6); it may be worthy to recall that **Do3** adsorption is known to occur via the carbonyl moieties. Compared with the previous literature[16,17,18], our spectra feature broader peaks, which may be traced to different adduct preparation protocols; co-milling $MgCl_2$ and **Do3**, rather than adsorbing **Do3** from solution on a pre-activated $MgCl_2$ sample, may well have led to a more complex surface distribution, because this donor can stabilize equally well $MgCl_2$ crystal terminations exposing 4-coordinated and 5-coordinated Mg (Chapters 1 and 2).

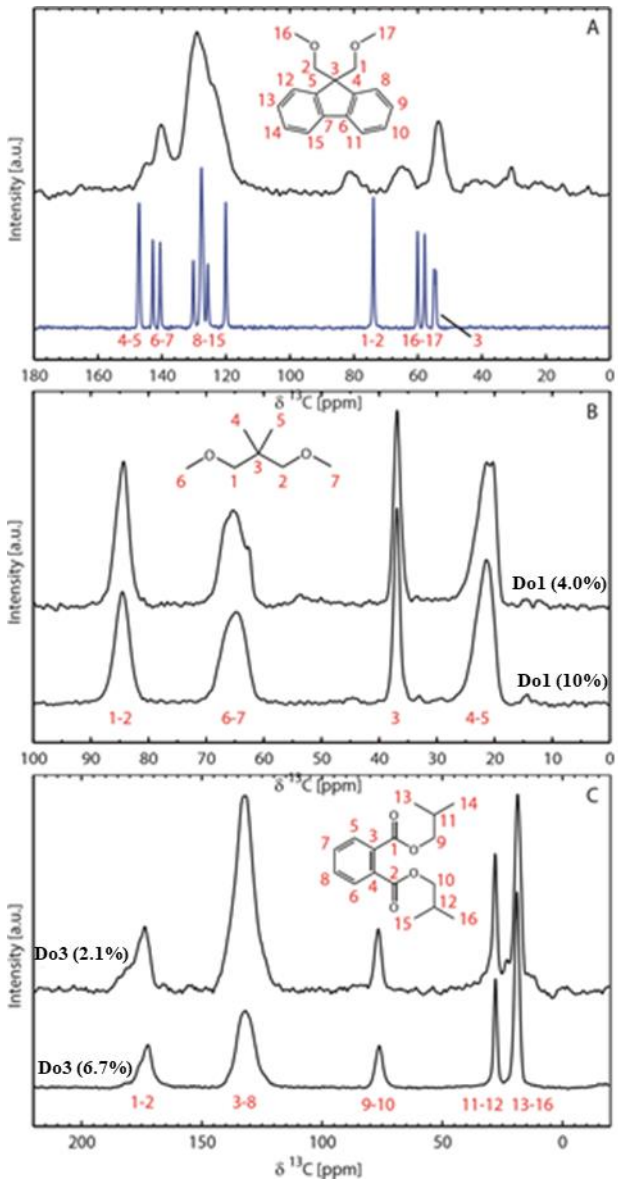

Figure 3.6. CPMAS ^{13}C NMR spectra of various $MgCl_2$/LB adducts (obtained at 9.4 T). In Figure 3.6-A, the CPMAS ^{13}C NMR spectrum of pure **Do2** is shown for comparison.

Table 3.4. Experimental CPMAS ^{13}C NMR chemical shifts (in ppm downfield of TMS) for a $MgCl_2$/**Do2** adduct and the pure donor.

Carbon #	δ (**Do2**)	δ ($MgCl_2$/**Do2**)
1	73.9	81.5
2	73.9	78.4
3	54.9 54.4	54.1 52.2
4	147.2	145.0
5	147.2	145.0
6	142.8	140.3
7	140.5	140.3
8	125.7	129.5
9	127.7	129.5
10	130.2	129.5
11	120.1	123.8
12	125.7	129.5
13	127.7	129.5
14	130.2	129.5
15	120.1	123.8
16	60.1	65.2
17	57.8	62.3

Table 3.5. Experimental CPMAS ^{13}C NMR chemical shifts (in ppm downfield of TMS) for $MgCl_2$/**Do1** adducts at different donor loadings (in mol-% relative to Mg), compared with the ^{13}C NMR chemical shifts of the free **Do1** molecule in $CDCl_3$ solution.

Carbon	$\delta_{solution}$	$\delta_{solid\text{-}state}$ **Do1** (4%)	$\delta_{solid\text{-}state}$ **Do1** (10%)
-OCH_2 (C-1, C-2)	78.9	84.2 85.0	84.5
Quaternary C (C-3)	35.9	36.9	36.9
-CH_3 (C-4, C-5)	21.9	23.1 21.3 20.0	23.1 21.1 -
-OCH_3 (C-6, C-7)	58.9	66.9 64.7 62.5	66.5 64.1 -

Table 3.6. Experimental CPMAS ^{13}C NMR chemical shifts (in ppm downfield of TMS) for $MgCl_2$/**Do3** adducts at variable donor loadings (in mol-% relative to Mg), compared with the ^{13}C NMR chemical shifts of the free **Do3** molecule in $CDCl_3$ solution.

Carbon	$\delta_{solution}$	$\delta_{solid\text{-}state}$ $MgCl_2$/**Do3** (2.1%)	$\delta_{solid\text{-}state}$ $MgCl_2$/**Do3** (6.7%)
Carbonyl (C-1, C-2)	167.3	173.4, 176.8, 181.0	172.5, 175.8, 182.0
Aromatic (C-3, C-4)	132.1	135.3	134.4
Aromatic (C-7, C-8)	130.6	131.8	131.2
Aromatic (C-5, C-6)	128.5	128.6	128.6
-OCH_2 (C-9, C-10)	71.4	76.1	76.2
-CH (C-11, C-12)	27.4	27.7	27.9
-CH_3 (C-13 – C-16)	18.9	18.1	18.9

The fine structure of CPMAS ^{13}C NMR spectra like those of Figure 3.6 contains valuable information on the binding mode of the donor molecules to

the $MgCl_2$ surface, and indirectly on the local surface environment too. This concept has been recognized in the previous literature[16-20], but never utilized in practice because assigning said fine structure is difficult. In the following section, we will illustrate an attempt based on state-of-the-art DFT-D methods, including structural optimizations for realistic models of $MgCl_2$/LB adducts, and calculations of ^{13}C chemical shift tensors thereof.

3.3.2 DFT calculations of ^{13}C chemical shift tensors for model $MgCl_2$/LB adducts

The adsorption of **Do1**, **Do2** and **Do3** on $MgCl_2$(104)-like and $MgCl_2$(110)-like surfaces was investigated by means of a cutting-edge cluster DFT-D approach, implemented in collaboration with Dr. Emanuele Breuza.[21] Two mono-layer $MgCl_2$ clusters with lateral terminations exposing mainly 5-coordinated and 4-coordinated Mg atoms, respectively, were used throughout: the former consisted of 24 $MgCl_2$ units (clu_24u_104), the latter of 27 $MgCl_2$ units (clu_27u_110). Donor molecules were adsorbed at different degrees of surface coverage, and the structures were optimized without any constraints, allowing for full relaxation.

*3.3.2.1 $MgCl_2$/**Do1** adducts*

A preliminary conformational analysis of the isolated (gas phase) **Do1** molecule was carried out, aiming to identify conformers suited to chemisorb on $MgCl_2$ surfaces. Out of four low-energy conformations with close Gibbs free energies values (Table A-3.3 and Figure 3.7), only two (namely, **A** and **C** of Figure 3.7) feature the methoxy moieties in orientations enabling the molecule to chelate 4-coordinate Mg on $MgCl_2$(110)-like terminations, or bridge 5-coordinated Mg on $MgCl_2$(104)-like terminations.

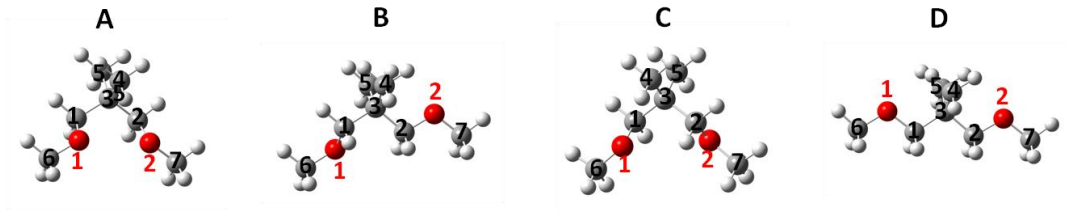

Figure 3.7. Optimized structures of the **Do1** conformers in gas phase (see text; calculations at TPSSTPSS/6-31+G(2d,p) level).

The optimized structures of $MgCl_2$ adducts with one single **Do1** molecule are shown in Figure 3.8; the corresponding values of adsorption energy and Gibbs free energy are reported in Table 3.7.

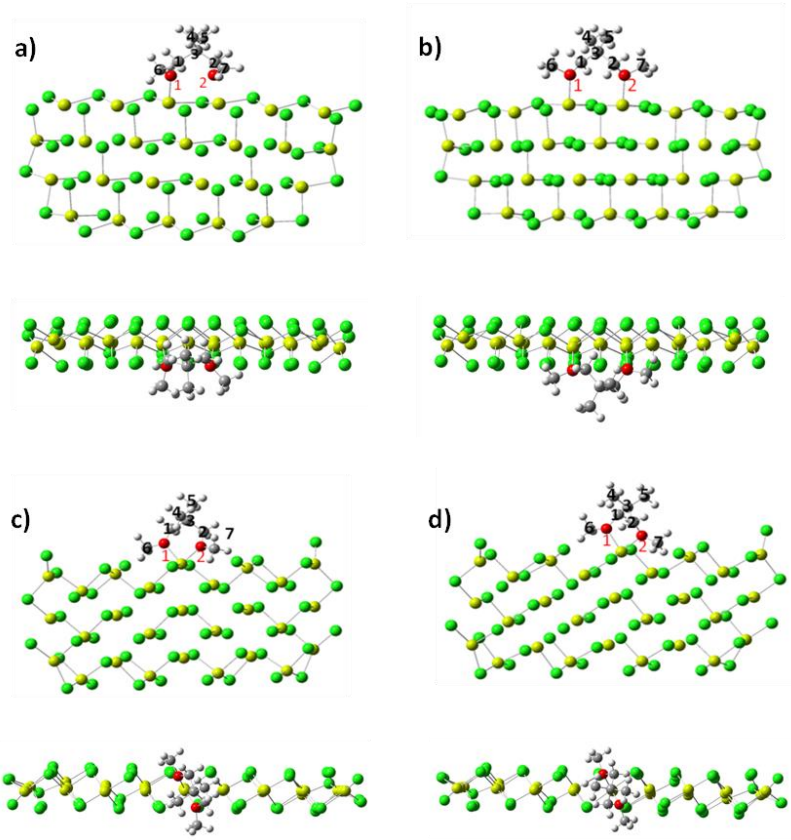

Figure 3.8. Side and top view of optimized structures of clu_24u_104_**Do1_A** (a), clu_24u_104_**Do1_C** (b), clu_27u_110_**Do1_A** (c) and clu_27u_110_**Do1_C** (d).

Table 3.7. Calculated binding energies (in kcal mol^{-1}) of the adducts of **Do1** on clu_24u_104 and clu_27u_110 model clusters. (Optimization and thermal corrections at 298.15 K were carried out at TPSSTPSS/6-31+G(2d,p) level; see Appendix A-3 for details).

	Δ*H* **(M06-2X)**	**Δ*G*** **(M06-2X)**	**Δ*H*** **(M06-2X-D3)**	**Δ*G*** **(M06-2X-D3)**	**Δ*H*** **(BP86-D3)**	**Δ*G*** **(BP86-D3)**
clu_24u_104 + Do1_A	-35.7	-20.4	-38.2	-23.0		
clu_24u_104 + Do1_C	-32.8	-17.1	-35.3	-19.6		
clu_27u_110 + Do1_A	-46.2	-31.9	-48.6	-34.2	-61.8	-47.4
clu_27u_110 + Do1_C	-42.4	-27.8	-44.7	-30.2	-59.3	-44.7

The results highlighted a strong preference (~11-15 kcal/mol) of **Do1** for chelating 4-coordinated Mg sites over bridging 5-coordinated Mg sites; this agrees with previous literature claims.[3,4,22] In all cases, conformer **A** turned out to bind stronger than conformer **C** (by 3-4 kcal/mol); this may well compensate its lower stability in the gas phase (Table A-3.3). The calculated values of ^{13}C chemical shifts for the four structures are reported in Table 3.8 (for details, see Appendix A-3).

Table 3.8. Calculated ^{13}C chemical shifts (δ_{calc}; in ppm) at TPSSTPSS/IGLO-II level for the clu_27u_110/**Do1** and clu_24u_104/**Do1** adducts (see Figure 3.7 and text).

Carbon #	**δ_{calc} 104 + A**	**δ_{calc} 104 + C**	**δ_{calc} 110 + A**	**δ_{calc} 110 + C**
1	84.9	79.9	86.3	82.1
2	82.2	79.9	83.4	82.1
3	41.2	41.0	38.4	38.2
4	24.3	21.0	19.0	20.6
5	21.8	20.8	20.7	20.6
6	62.6	63.5	64.0	64.6
7	62.6	63.1	63.8	64.6

Overall, the agreement between calculated and experimental (Table 3.6) values is decent (within ±3 ppm). This notwithstanding, reasoning on surface- and conformation-induced effects is safer and also more revealing than comparing absolute values. If one takes the experimental data for the $MgCl_2$/**Do1** (10 mol-%) adduct as a reference (Figure 3.6-B and Table 3.5), the following facts should be noted:

- The chemical shift values of the quaternary carbon (C-3) are very different for chelating and bridging adsorbates. Based on this, one can rule out the hypothesis that both modes are co-present, because the resonance of this C is single and rather sharp.

- Only the binding of conformer **A** was calculated to lead to a surface-induced asymmetry, both for 104-like and 110-like terminations (Figure 3.8). The predicted splitting was about 2 ppm for the methyl Cs (C-4 and C-5), and 0.2 ppm for the methoxy Cs (C-6 and C-7), which is in nice agreement with experiment. On the other hand, an even larger splitting (~3 ppm) was calculated for the -OCH_2- Cs (C-1 and C-2), which is less consistent with the experimental finding.
- An average of the two conformations on one termination, or of all conformations on both terminations, would produce a large split of the -OCH_2- (around 3-4 ppm), which is inconsistent with experiment.

Overall, energy and chemical shift calculations point to conformer **A** on 110-like terminations as the dominant adsorbate.

The additional features of the experimental spectrum for the adduct at lower **Do1** content, namely $MgCl_2$/**Do1** (4 mol-%), suggest the presence of a second species in minor amount. Looking at relative stabilities, conformer **C** on 110-like surfaces seems to be the most plausible candidate. This is consistent with the previously noted fact that C-3 features a single, narrow resonance; on the other hand, the calculations do not support the experimental observation of lower chemical shift values for C-4 to C-7.

We are the first to admit that the model clusters investigated so far are only rough approximations of real-world adducts, which are characterized by a larger degree of surface coverage and multiple structural layers. Fully relaxed multi-layer models are still prohibitively expensive in terms of necessary computational time and resources. On the other hand, mono-layer models at high(er) degree of coverage are feasible, and evaluating the effect of this parameter on calculated ^{13}C chemical shifts was our next step. We focused on 110-like terminations, in view of the strong preference of **Do1** for them (Table 3.7). Two models were implemented: one featuring three **Do1** molecules on

cluster clu_27u_110 (Figure 3.9); another with five **Do1** molecules adsorbed on a larger cluster, namely clu_39u_110 consisting of 39 $MgCl_2$ units (Figure 3.10). Due to the higher computational demand, we carried out structure optimizations and frequency calculations with a smaller basis set than for the single-molecule adducts. Moreover, full relaxation was only possible for the smaller clusters, whereas a 'frozen cluster' approximation had to be adopted for the larger ones (see Appendix A-3 for computational details). Calculated adsorption energies are summarized in Table 3.9, whereas calculated ^{13}C chemical shift splittings are listed in Tables 3.10 to 3.12.

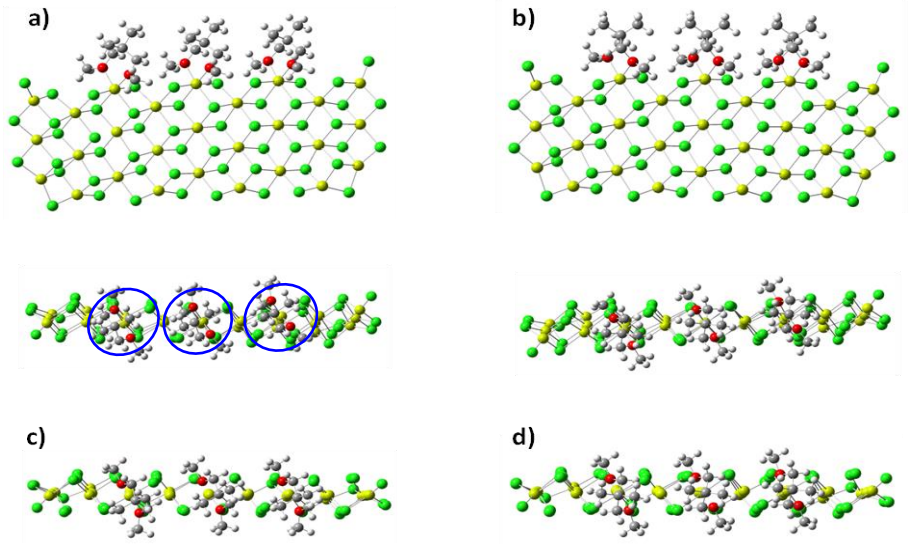

Figure 3.9. Optimized structures of clu_27u_110 + 3**Do1_A** (a: fully relaxed, side and top view; c: frozen cluster approximation, top view only), and clu_27u_110 + 3**Do1_C** (a: fully relaxed, side and top view; c: frozen cluster approximation, top view only). RI-TPSSTPSS/def2-SVP level (see text for details).

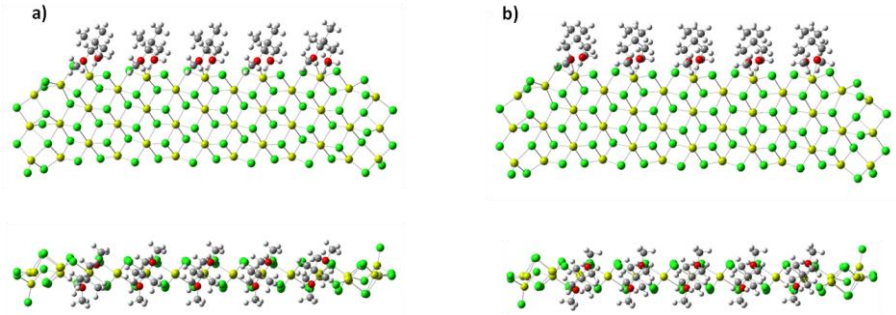

Figure 3.10. Optimized structures of clu_39u_110 + 5**Do1_A** (a: side and top view), and clu_39u_110 + 5**Do1_C** (b: side and top view). Frozen cluster approximation, RI-TPSSTPSS/def2-SVP level (see text for details).

Table 3.9. Calculated **Do1** adsorption energies (in kcal mol^{-1}) for various adducts of **Do1** in **A** or **C** conformation with clusters belonging in the clu_27u_110 and clu_39u_110 families. Optimization and thermal corrections (at 298.15 K) calculated at TPSSTPSS(-D3)/def2-SVP level (see text and Appendix A-3 for details).

	$\Delta E_{average}$	$\Delta H_{average}$	$\Delta H_{terminal\text{-}molecule}$	$\Delta G_{average}$	$\Delta G_{terminal\text{-}molecule}$
clu_39u_110 + 5 Do1_A*	-38.4				
clu_27u_110 + 3 Do1_A		-55.3	-54.6	-40.8	-40.5
clu_27u_110 + 3 Do1_A*	-43.4				
clu_27u_110 + Do1_A		-55.2		-40.5	
clu_39u_110 + 5 Do1_C*	-35.6				
clu_27u_110 + 3 Do1_C		-51.2	-49.9	-36.4	-35.5
clu_27u_110 + 3 Do1_C*	-37.6				
clu_27u_110 + Do1_C		-51.6		-36.9	

* Frozen cluster approximation

Table 3.10. Calculated ^{13}C chemical shift splits ($\Delta\delta$; in ppm) for chemically equivalent Cs of **Do1** (full relaxation, TPSSTPSS/IGLO-II level) for the clu_27u_110 + 3**Do1** adducts (see text for details). Molecule positioning refers to Figure 3.9.

	|Δδ| clu_27u_110 + 3 Do1_A			**|Δδ| clu_27u_110 + 3 Do1_C**		
Carbon #	**Left**	**Middle**	**Right**	**Left**	**Middle**	**Right**
1-2	2.0	2.1	2.3	0.5	0.0	0.5
4-5	1.4	0.5	0.3	0.3	0.0	0.3
6-7	1.1	1.1	1.1	0.4	.0.0	0.4

Table 3.11. Calculated chemical shift splits (Δδ; in ppm) for chemically equivalent Cs of **Do1** (frozen cluster approximation, TPSSTPSS/IGLO-II level) for the clu_27u_110 + 3**Do1** adducts (see text for details). Molecule positioning refers to Figure 3.9.

	|Δδ| clu_27u_110_fixed + 3 Do1_A			**|Δδ| clu_27u_110_fixed + 3 Do1_C**		
Carbon #	**Left**	**Middle**	**Right**	**Left**	**Middle**	**Right**
1-2	3.2	2.4	4.1	0.4	0.0	0.4
4-5	1.2	1.2	0.1	1.3	0.0	1.3
6-7	0.3	1.2	1.0	1.0	0.0	1.0

Table 3.12. Calculated chemical shift splits (Δδ; in ppm) for chemically equivalent Cs of **Do1** (frozen cluster approximation, TPSSTPSS/IGLO-II level) for the clu_39u_110 + 5**Do1** adducts (see text for details). Molecule positioning refers to Figure 3.10.

	|Δδ| clu_39u_110 + 5 Do1_A					**|Δδ| clu_39u_110 + 5 Do1_C**				
Carbon #	**Leftmost**	**Left**	**Middle**	**Right**	**Rightmost**	**Leftmost**	**Left**	**Middle**	**Right**	**Rightmost**
1-2	2.3	3.4	3.6	3.5	3.7	0.9	0.0	0.0	0.0	0.9
4-5	0.2	0.4	0.7	0.4	0.2	1.8	0.0	0.0	0.0	1.8
6-7	0.1	0.2	0.6	1.2	2.0	0.3	0.0	0.0	0.0	0.3

When full relaxation was allowed, a 'wave-like' cluster deformation was observed. Compared with frozen cluster calculations, this resulted into significantly larger calculated values of donor adsorption energies (by ~12-15 kcal mol^{-1}; see Table 3.9), and position-dependent changes in the chemical and magnetic environments of the adsorbed molecules along a string. For example, when looking at the top view of the clu_27u_110 + 3**Do1_A** system (Figure 3.9-a), one can see that, in the **Do1** molecule to the left, one of the 2-methyl groups eclipsed a Cl atom of the underlying surface, whereas the other eclipsed a Mg atom; on the other hand, in the central and right-most **Do1** molecules, both methyls eclipsed Mg atoms or Cl atoms, respectively. This specific deformation mode may have resulted from an unbalanced donor adsorption (all **Do1** molecules were positioned on the same cluster side), and therefore represent an artifact.

Looking at the overall results, one can conclude that increasing the degree of surface coverage did not lead to important position-dependent effects in calculated **Do1** adsorption energy values, nor in the relative stability of conformers **A** and **C** in corresponding surface environments (Table 3.9), whereas it did affect calculated ^{13}C chemical shift splits (Tables 3.10-3.12). In particular, no split was predicted for the central **Do1** molecule in **C** conformation, both for the 3-molecule and the 5-molecule string, independently of whether or not full cluster relaxation was allowed. This seems to rule out this conformer in high-coverage adducts, such as $MgCl_2$/**Do1** (10%), whereas it lends support to the hypothesis of a co-presence of conformer **A** and **C** in adducts at lower degree of surface coverage, such as $MgCl_2$/**Do1** (4%). For all other Cs, more or less significant variations were observed, depending on the model and whether or not the structure was allowed to relax; however, no decisive improvement in the agreement with experiment was achieved.

*3.3.2.2 $MgCl_2$/**Do2** adducts*

Despite the rigid skeleton and the lack of conformationally flexible aliphatic side chains, the **Do2** molecule is significantly larger than **Do1**, and therefore computationally more demanding. In analogy with **Do1**, two low-energy conformers suited to interact with the $MgCl_2$ surface were identified (and labelled as **A** and **C**, in analogy with **Do1**). Model adducts with one single **Do2** molecule adsorbed on 110-like and 104-like terminations were evaluated (Figure 3.11); the former were found to be more stable by ~10-12 kcal mol^{-1}, which is consistent with the propensity of 1,3-diethers to chelate 4-coordinated Mg, already discussed for **Do1**. Conformer **A** was always slightly more stable than conformer **C** (by ~1.5 kcal mol^{-1}) in a given surface environment. Models

at a higher degree of surface coverage, with three **Do2** molecules on 110-like terminations, were also examined (Figure 3.12). The calculated values of ^{13}C chemical shifts are collected in Tables 3.13 and 3.14.

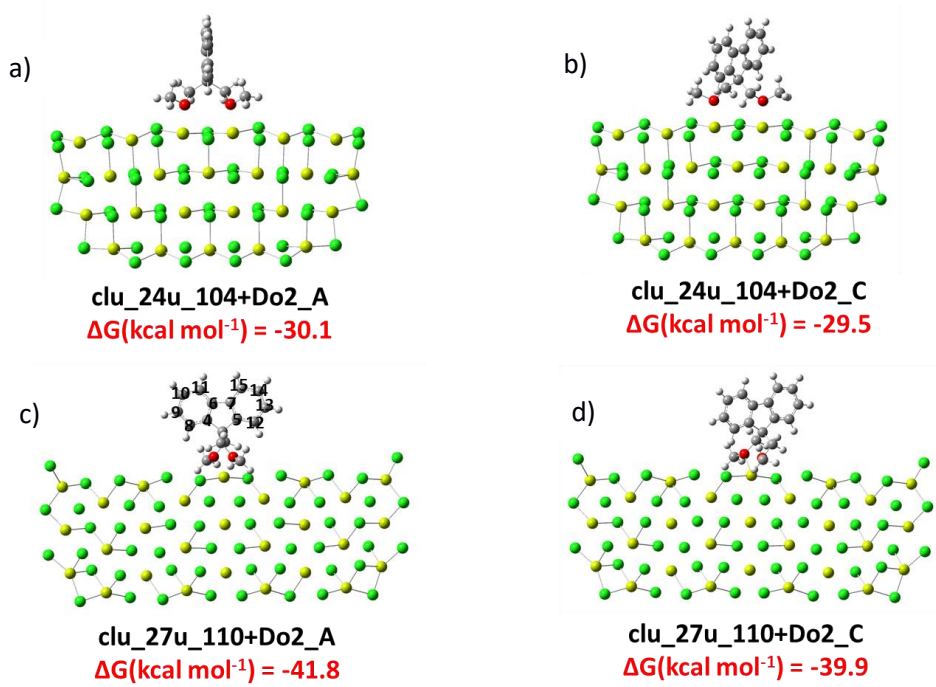

Figure 3.11. Optimized structures of clu_24u_104_**Do2_A** (a), clu_24u_104_**Do2_C** (b), clu_27u_110_**Do2_A** (c), and clu_27u_110_**Do2_C** (d), with corresponding calculated ΔG_{ads} values.

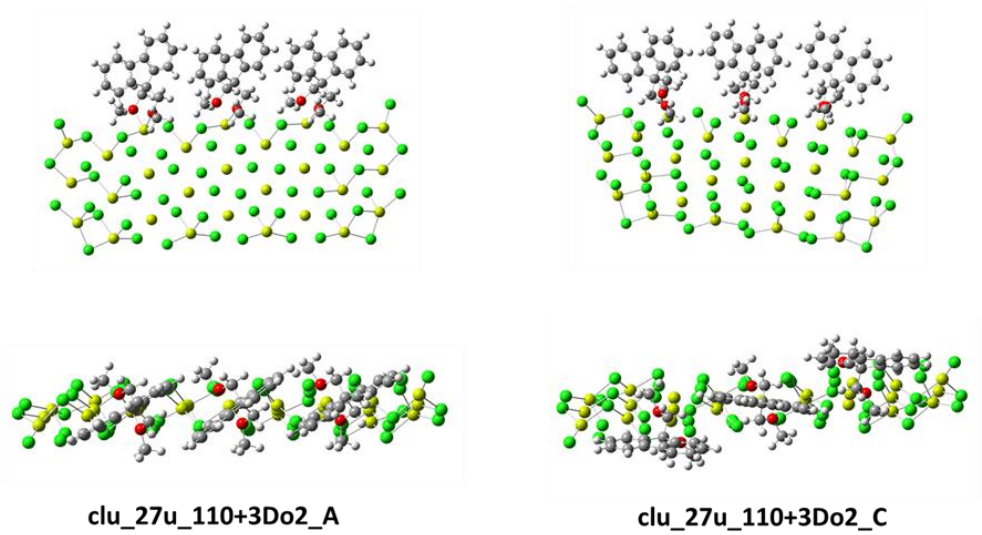

Figure 3.12. Side and top view of the optimized structures of clu_27u_110 + 3**Do2_A** (left), and clu_27u_110 + 3**Do2_C** (right). See text for details.

Table 3.13. Calculated ^{13}C chemical shifts (δ_{calc}; in ppm) at TPSSTPSS/IGLO-II level for clu_27u_110 + **Do2** and clu_24u_104 + **Do2** adducts (**A** and **C** conformers; see text and Figure 3.11).

Carbon #	**Type**	**δ_{calc} 104+A**	**δ_{calc} 104+C**	**δ_{calc} 110+A**	**δ_{calc} 110+C**
1	-OCH_2-	81.7	78.8	83.0	80.8
2		81.7	78.4	81.9	81.0
3	Quaternary	56.3	56.3	55.8	56.2
4	Aromatic	141.0	139.7	138.5	143.2
5		140.3	141.1	143.1	143.0
6		136.8	138.1	139.0	138.4
7		139.4	138.9	137.8	138.2
8		120.3	123.0	120.1	121.2
9		125.8	125.6	124.3	124.9
10		126.6	127.1	126.7	126.4
11		118.0	117.9	117.6	117.5
12		125.7	122.1	125.5	121.5
13		123.2	124.2	124.8	124.9
14		126.6	126.5	125.8	126.6
15		118.0	118.2	117.3	117.5
16	-OCH_3	63.9	63.3	63.6	64.1
17		63.9	63.5	63.3	64.0

Table 3.14. Calculated ^{13}C chemical shifts (δ_{calc}; in ppm) at TPSSTPSS/IGLO-II level for the clu_27u_110 + 3**Do2** adducts (see text and Figure 3.12).

Carbon #	**Type**	**δ_{calc}** clu 27u 110 + 3**Do2_A**	**δ_{calc}** clu _27u 110 + **3Do2_C**
1	-OCH_2-	83.2	80.4
2		81.7	80.4
3	Quaternary	56.5	56.8
4	Aromatic	139.5	144.8
5		144.7	144.8
6		139.2	138.8
7		138.3	138.8
8		122.0	122.1
9		124.5	127.1
10		127.2	126.8
11		117.5	117.8
12		126.7	122.1
13		125.0	128.1
14		125.8	126.8
15		117.2	117.8
16	-OCH_3	65.0	64.7
17		64.0	64.7

Looking at the calculated ^{13}C chemical shift values for the single-adsorbate models (Table 3.13), the agreement with experiment (Table 3.4) is rather good for the -OCH_2- and -OCH_3 Cs; decent for the quaternary C; poor for the aromatic Cs, likely due to surface effects on the π-electron density[22,23] that are challenging to model. In general, calculated chemical shift splittings following to adsorption were (much) less pronounced than experimental ones; in particular, no splitting was predicted for the methoxy Cs of both conformers **A** and **C** on 110-like terminations. A better agreement, on the other hand, was achieved for the higher-coverage models (Table 3.14); in this case, calculations did predict a splitting of the methoxy C resonance for the lowest-energy

conformer **A** on 110-like terminations, which therefore seems to be the most plausible structure.

*3.3.2.3 $MgCl_2$/**Do3** adducts*

Structure optimizations for single-molecule **Do3** adducts with 104-like and 110-like terminations (Figure 3.13) highlighted a symmetrical conformer (**S**) and a non-symmetrical conformer (**NS)**, differing in the orientation of the two isobutoxy substituents relative to the aromatic plane of the molecule. The lowest-energy adducts with 104-like surfaces featured a bridging mode; for the **NS** conformer, two minima with different orientations relative to the structural layer were identified (and labelled as **NS-1** and **NS-2**). A chelating mode, on the other end, was preferred on 110-like terminations. Calculated adsorption energies were similar for all adducts, which indicates that this ID has no clear preference for 5-coordinated or 4-coordinated surface Mg atoms; this is consistent with the previous literature.[1,2,21,24,25]

Calculated ^{13}C chemical shifts for all five structures of Figure 3.13 are reported in Table 3.15. The agreement with experimental data is rather good; however, most values are poorly sensitive to the donor adsorption mode. The only exception is the carbonyl resonance, which seems to be rather surface-specific: relative to the free **Do3** molecule in solution, adsorption on 110-like terminations was calculated to result into a larger downfield shift ($\Delta\delta \sim 4$ ppm) than that on 104-like terminations. In both cases, splittings of 1-3 ppm were predicted for the non-symmetrical conformers only. Experimentally, we observed multiple resonances in the carbonyl region (Figure 3.6), which lends support to the aforementioned hypothesis of indiscriminate binding of this donor based on thermodynamic data.

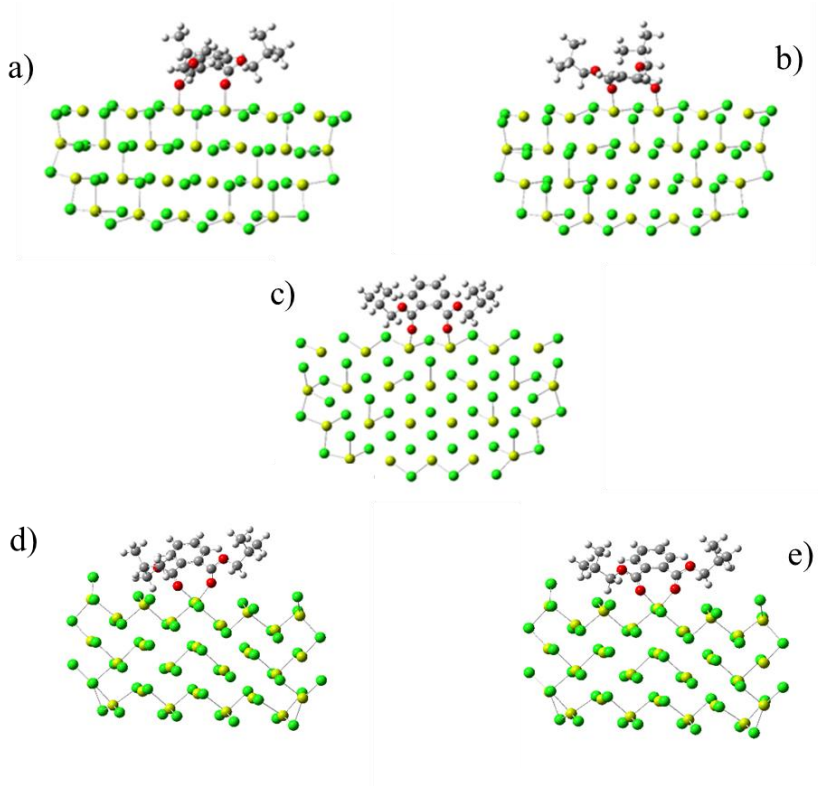

Figure 3.14. Optimized structure (side view) of (a) clu_24u_104 + **Do3_NS1,** (b) clu_24u_104 + **Do3_NS-2**, (c) clu_24u_104 + **Do3_S**, (d) clu_27u_110 + **Do3_NS**, and (e) clu_27u_110 + **Do3_S** (see text for details).

Table 3.15. Calculated ^{13}C chemical shifts (δ_{calc}; in ppm) at TPSSTPSS/IGLO-II level for the model $MgCl_2$/**Do3** adducts of Figure 3.13 (see text for details).

Carbon #	**δ_{calc} (ppm)**				
	clu_24u_104 + **Do3_NS-1**	clu_24u_104 + **Do3_NS-2**	clu_24u_104 + **Do3_S**	clu_27u_110 + **Do3_NS**	clu_27u_110 + **Do3_S**
1	171.4	175.4	174.0	168.8	169.9
2	174.9	174.5	173.9	170.4	170.0
3	129.9	132.4	128.7	128.9	129.3
4	133.1	130.2	128.7	130.0	129.5
5	128.6	129.3	128.6	132.1	131.6
6	128.0	128.5	128.6	130.5	130.9
7	129.4	131.8	128.6	130.7	130.9
8	131.3	130.0	128.6	131.4	131.4
9	80.7	78.9	78.3	76.0	78.2
10	80.4	78.6	78.3	79.4	79.6
11	31.4	30.4	30.8	32.7	30.9
12	30.2	31.4	30.8	30.4	30.1
13	17.8	17.6	17.8	16.9	17.9
14	17.7	17.7	17.4	18.5	18.3
15	17.5	17.6	17.8	17.5	17.9
16	17.5	17.6	17.4	17.9	18.0

3.4 Summary and conclusions

In this Chapter we reported on the characterization of $MgCl_2$/LB model adducts by means of advanced solid-state (Q)NMR techniques. The study included DFT-D calculations of quadrupole coupling constants and chemical shift tensors for systems at variable degree of surface coverage, as an aid to the interpretation of the experimental spectra. Unfortunately, the ^{25}Mg and ^{35}Cl QNMR spectra of samples at natural isotopic abundance were poorly informative, due to a low signal-to-noise ratio and a (very) broad line width. On the other hand, the comparison of CPMAS ^{13}C NMR spectra with DFT-D

simulated ones was very useful to narrow the hypotheses on possible LB adsorption sites and modes. A rather good agreement between experimental results and calculations was reached for all donors, in particular for the carbons closest to the binding site. Generally, the aromatic moieties show somewhat larger deviations, likely due to surface effects on the π-electron density.

All in all, our findings consistently indicated that certain LB (e.g. 1,3-diethers) chemisorb in preference on $MgCl_2$ crystal terminations exposing tetra-coordinated Mg, whereas others (e.g. phthalates) do not feature any strong preference for a particular crystal edge., in line with previous literature claims.

Appendix A-3

DFT Modeling

NMR chemical shielding (σ) arises from the neighboring electronic environment around the detecting nucleus. Chemical shift (δ) is reported as the frequency off set with respect to a reference compound (σ_{ref}), such as tetramethylsilane (TMS), as shown in Eq. A-3.1:

$$\delta = \frac{\sigma_{ref} - \sigma_{sample}}{1 - \sigma_{sample}} \sim \sigma_{ref} - \sigma_{sample} \qquad \text{(Eq. A-3.1)}$$

All chemical shielding calculations were carried out with a cluster approach, using the Gaussian09 package.[26]

For single-adsorbate models, optimization and frequency calculations were carried out at RI[27]-TPSSTPSS[28]/6-31+G(2d,p)[29] level, while single point energy corrections were carried out at RI-M06-2X[30](-D3)[31]/6-31+G(2d,p) and RI-BP86[32]-D3/6-31+G(2d,p) level. Considering the computational demanding size of the investigated systems, the calculated energies were not corrected for Basis Set Superposition Error (BSSE). The aforementioned computational protocol, recently published in the same group hosting the present thesis, has been benchmarked on model systems relevant to Ziegler-Natta catalysis, ensuring a good accuracy on the calculated energies (i.e. ± 1.5 kcal/mol), even without BSSE correction.[33]

^{13}C chemical shielding calculations were performed at TPSSTPSS level of theory exploring different basis sets, including basis set suited for chemical shielding calculations, such as aug-pVTZ-J,[34] IGLO-II[35] and IGLO-III.[36] In view of the fact that comparable results were obtained for all basis sets, we

only discussed IGLO-II results, for the sake of simplicity. Chemical shifts (δ) were calculated relative to TMS.

The increased computational demand for high-coverage systems with multiple adsorbate molecules forced us to carry out optimization and frequency calculations at RI-TPSSTPSS level, with a smaller basis set, namely def2-SVP,[37] correcting the electronic energy with Grimme's D3[31] dispersion correction.

Table A-3.1. Experimental and calculated lattice parameters (in Å), ^{25}Mg and ^{35}Cl quadrupole coupling constants (in MHz) and asymmetry parameters (η), computed at different energy cut-offs (in eV) with various dispersion correction methods (see text).

	E cut-off [eV]	Dispersion Correction	*a* [Å]	*c* [Å]	^{25}Mg C_Q [MHz]	η	^{35}Cl C_Q [MHz]	H
VASP	262	Grimme D2	3.6363 *	17.6663*	1.423	0.0	4.09	0.0
	400		3.6199	17.9490	1.258	0.0	3.57	0.0
	495		3.5950	17.3385				
	600		3.6267	17.8976	1.244	0.0	3.58	0.0
	700		3.6222	17.7812	1.219	0.0	3.55	0.0
	1200		3.6276	17.9441	1.172	0.0	3.83	0.0
	400	vdW-DF	3.6416	17.3399	1.380	0.0	4.51	0.0
	1200		3.6518	17.4228	1.227	0.0	4.65	0.0
	400	Grimme D3	3.6413	17.6911	1.484	0.0	4.36	0.0
	1200		3.6487	17.7100	1.448	0.0	4.61	0.0
CRYSTAL09	B3LYP/TZVP	Grimme D2	3.6309	17.2964	1.622	0.0	4.38	0.0
Experimental			3.6363	17.6663	1.619	0.0	4.60	0.0

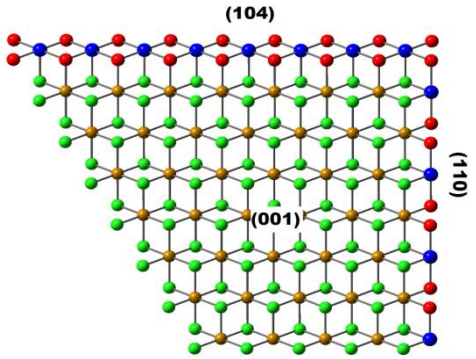

Figure A-3.1. Model of $MgCl_2$(001), $MgCl_2$(104) and $MgCl_2$(110) surfaces in a $MgCl_2$ monolayer.

Table A-3.2. ^{35}Cl and ^{25}Mg quadrupole coupling constants (C_Q) (in MHz) and asymmetry parameters (η) for $MgCl_2$(001), $MgCl_2$(104) and $MgCl_2$(110), calculated at PBE/PAW level using the VASP code, and at B3LYP/TZVP level using the CRYSTAL09 code (see text and Figure C3.1).

	Approach	Basis set	Atom	Surface	C_Q	η
VASP	Periodic	plane wave	^{35}Cl	$MgCl_2$ 001	4.18	0.0
				$MgCl_2$ 104	11.1	0.9
				$MgCl_2$ 110	15.4	0.5
			^{25}Mg	$MgCl_2$ 001	1.48	0.0
				$MgCl_2$ 104	7.61	0.3
				$MgCl_2$ 110	12.3	0.2
CRYSTAL09		atom-centred	^{35}Cl	$MgCl_2$ 001	5.60	0.0
				$MgCl_2$ 104	11.2	0.9
				$MgCl_2$ 110	16.0	0.6
			^{25}Mg	$MgCl_2$ 001	1.93	0.0
				$MgCl_2$ 104	10.8	0.3
				$MgCl_2$ 110	15.6	0.3

Table A-3.3. Relative ΔG (kcal/mol; 298.15K), Boltzmann distribution, and structural parameters for **Do1** conformers (M06-2X/6-31+G(2d,p)//TPSSTPSS/6-31+G(2d,p)).

	ΔG	**Boltzmann distribution**	**$d_{(O1-O2)}$ [Å]**	**$\tau_{(C1-C3-C2)}$ [deg]**	**$\vartheta_{(C6-O1-C1-C3)}$ [deg]**	**$\vartheta_{(O1-C1-C3-C2)}$ [deg]**	**$\vartheta_{(C1-C3-C2-O2)}$ [deg]**	**$\vartheta_{(C3-C2-O2-C7)}$ [deg]**
A	3.6	0.001	2.98	112.2	178.9	72.1	-72.1	-178.9
B	0.5	0.418	4.21	108.2	-178.8	-59.8	-176.7	-178.0
C	0.0	0.520	3.48	110.0	-177.3	61.0	61.1	-177.3
D	1.3	0.060	4.84	106.2	179.9	-179.9	-179.9	-179.9

Table A-3.4. Comparison of calculated (TPSSTPSS/IGLO-II) ^{13}C chemical shifts, weighted average, based on Boltzmann distribution ($\delta_{average}$; in ppm) and deviations (**Δ**; in ppm) wrt experiment for **Do1**.

Carbon #	**EXP**	**A**	**B**	**C**	**D**	**$\delta_{average}$**	**Δ**
1	78.9	88.4	84.3	81.5	84.8	83.1	+4.2
2		88.4	86.2	81.5	84.8	83.1	+4.2
3	35.9	42.0	42.4	41.5	43.4	42.0	+6.1
4	21.9	22.6	22.5	24.1	23.2	23.4	+1.5
5		25.7	24.0	24.1	23.2	24.0	+2.1
6	58.9	62.3	62.2	62.0	62.3	62.1	+3.2
7		62.3	62.2	62.0	62.3	62.1	+3.2
						MAD	+3.5

Table A-3.5. Comparison of calculated chemical shifts (in ppm) calculated at TPSSTPSS level (with different basis sets) with respect to experimental ones in solution ($CDCl_3$) for **Do1**.

	EXP	**aug-cc-pVTZ**				**aug-cc-pVTZ-J**				**IGLO-III**			
Carbon #		**A**	**B**	**C**	**D**	**A**	**B**	**C**	**D**	**A**	**B**	**C**	**D**
1	78.9	85.7	82.1	77.6	82.6	89.1	85.2	82.4	85.7	90.8	86.7	83.7	87.2
2		85.7	86.0	77.6	82.6	89.1	86.9	82.4	85.7	90.8	88.7	83.7	87.2
3	35.9	39.7	43.4	45.9	42.7	42.1	42.4	40.9	43.9	43.2	43.8	42.8	44.7
4	21.9	19.9	20.0	19.6	19.3	22.3	22.3	24.0	23.3	23.0	22.8	24.6	23.5
5		24.6	21.1	19.6	19.3	25.9	23.8	24.0	23.3	26.4	24.5	24.6	23.5
6	58.9	60.0	59.7	58.3	58.9	62.8	62.8	62.6	63.0	63.7	63.7	63.5	63.8
7		60.0	59.1	58.3	58.9	62.8	62.9	62.6	63.0	63.7	63.7	63.5	63.8

Table A-3.6. Weighted average of calculated chemical shifts (based on Boltzmann distribution; in ppm) and deviations (Δ; in ppm) with respect to experimental chemical shifts for **Do1**.

	EXP	aug-cc-pvTZ		aug-cc-pvTZ-J		IGLO-III	
Carbon #		**δ_{calc}**	**Δ**	**δ_{calc}**	**Δ**	**δ_{calc}**	**Δ**
1	78.9	80.5	+1.6	84.0	+5.1	85.4	+6.5
2		80.5	+1.6	84.0	+5.1	85.4	+6.5
3	35.9	44.7	+8.8	41.6	+5.7	43.3	+7.4
4	21.9	19.7	-2.2	23.3	+1.4	23.8	+1.9
5		20.2	-1.7	23.9	+2.0	24.5	+2.6
6	58.9	58.8	-0.1	62.7	+3.8	63.6	+4.7
7		58.8	-0.1	62.7	+3.8	63.6	+4.7

Table A-3.7. Structural parameters for the various optimized structures of **Do1** on 104-like and 110-like $MgCl_2$ cluster terminations.

	$d_{(O1\text{-}Mg)}$ [Å]	**$d_{(O2\text{-}Mg)}$ [Å]**	**$d_{(Mg\text{-}Mg)}$ [Å]**	**$d_{(O1\text{-}O2)}$ [Å]**	**$\vartheta_{(C6\text{-}O1\text{-}C1\text{-}C3)}$ [deg]**	**$\vartheta_{(O1\text{-}C1\text{-}C3\text{-}C2)}$ [deg]**	**$\vartheta_{(C1\text{-}C3\text{-}C2\text{-}O2)}$ [deg]**	**$\vartheta_{(C3\text{-}C2\text{-}O2\text{-}C7)}$ [deg]**
clu_24u_104 + A	2.12	2.18	3.59	3.06	75.20	59.04	-67.23	-98.28
clu_24u_104 + C	2.19	2.2	3.70	3.76	98.58	64.36	63.78	97.97
clu_27u_110 + A	2.14	2.09	6.46	2.91	163.9	67.59	-69.86	-125.9
clu_27u_110 + C	2.15	2.15	6.43	2.85	141.9	41.25	41.26	141.9

Table A-3.8. Calculated ^{13}C chemical shifts (δ_{calc}; in ppm) at TPSSTPSS level (with different basis sets) for the $MgCl_2$/**Do1** adducts.

	aug-cc-pVTZ-J				IGLO-III			
Carbon #	**δ_{calc} 104 + A**	**δ_{calc} 104 + C**	**δ_{calc} 110 + A**	**δ_{calc} 110 + C**	**δ_{calc} 104 + A**	**δ_{calc} 104 + C**	**δ_{calc} 110 + A**	**δ_{calc} 110 + C**
1	84.2	79.8	86.1	81.0	86.1	80.4	87.2	82.9
2	81.2	80.3	83.2	81.0	83.3	80.1	84.2	82.9
3	40.7	38.9	35.4	35.8	41.8	40.8	38.5	38.2
4	23.6	20.5	17.8	20.3	23.9	19.8	19.5	19.7
5	22.0	19.5	19.1	20.3	20.9	19.8	17.9	19.7
6	62.2	63.7	64.3	64.9	62.9	63.7	64.2	64.9
7	62.3	63.4	63.9	64.9	62.5	63.5	63.5	64.9

Table A-3.9. Calculated chemical shifts (δ; in ppm) at TPSSTPSS/IGLO-II level for the clu_27u_110 + 3**Do1** adducts (see text and Figure 3.9).

	δ clu_27u_110 + 3 Do1_A			**δ clu_27u_110 + 3 Do1_C**		
Carbon #	**Left**	**Middle**	**Right**	**Left**	**Middle**	**Right**
1	85.3	85.4	85.6	81.7	81.9	82.2
2	83.3	83.3	83.3	82.2	81.9	81.7
3	39.4	39.5	40.0	38.8	38.4	38.8
4	20.4	21.2	21.2	20.7	21.1	21.0
5	21.8	21.7	21.5	21.0	21.1	20.7
6	65.3	65.6	64.8	64.9	65.4	64.5
7	64.2	64.5	63.7	64.5	65.4	64.9

Table A-3.10. Calculated chemical shifts (δ; in ppm) at TPSSTPSS/IGLO-II level for the clu_27u_110 + 3**Do1** adducts; the structures were obtained keeping the Mg and Cl atomic positions frozen (see text for details).

	δ clu_27u_110_fixed + 3 Do1_A			**δ clu_27u_110_fixed + 3 Do1_C**		
Carbon #	Left	Middle	Right	Left	Middle	Right
1	85.8	86.1	85.9	81.8	81.9	82.2
2	82.6	83.7	81.8	82.2	81.9	81.8
3	39.2	39.5	39.0	38.0	39.3	38.0
4	21.9	21.0	22.3	22.6	22.5	23.9
5	23.1	22.2	22.4	23.9	22.5	22.6
6	62.4	65.4	61.4	62.4	65.4	61.4
7	62.7	64.2	62.4	61.4	65.4	62.4

Table A-3.11. Calculated chemical shifts (δ; in ppm) at TPSSTPSS/IGLO-II level for the clu_39u_110 + 5**Do1** adducts (see Figure 3.10); the structures were optimized keeping the Mg and Cl atomic positions frozen (see text for details).

	δ clu_39u_110 + 5 Do1_A					**δ clu_39u_110 + 5 Do1_C**				
Carbon #	**Leftmost**	**Left**	**Middle**	**Right**	**Rightmost**	**Leftmost**	**Left**	**Middle**	**Right**	**Rightmost**
1	83.5	82.9	82.5	82.3	81.7	81.2	79.9	79.7	79.9	80.3
2	85.8	86.3	86.1	85.8	85.4	80.3	79.9	79.7	79.9	81.2
3	41.0	39.4	39.2	39.0	40.7	40.4	40.4	40.3	40.4	40.4
4	23.2	23.1	22.5	22.5	22.6	23.2	23.4	23.4	23.4	25.0
5	23.4	23.5	23.2	22.9	22.8	25.0	23.4	23.4	23.4	23.2
6	62.0	63.0	63.4	63.7	63.1	61.1	61.6	61.7	61.6	60.8
7	61.9	62.8	62.8	62.5	61.1	60.8	61.6	61.7	61.6	61.1

Solid-state NMR characterizations

All solid-state NMR characterizations were carried out at the Radboud Universiteit Nijmegen (research group of Prof. A. Kentgens).

^{25}Mg and ^{35}Cl spectra were recorded at room temperature on a Varian VNMRS 850 MHz spectrometer (20 T, 52.0 MHz for ^{25}Mg, 83.25 MHz for ^{35}Cl) using a triple resonance 4.0 mm Varian T3MAS probe at 15.625 kHz MAS. The

spectra were obtained using a Hahn-echo with short echo times: 1 rotor period (64 µs) or 16 µs (static). Quantitative measurements were performed with recycle delays of 3-5 times T1. The relaxation times varied widely: ^{25}Mg and ^{35}Cl T_1 ranged from 5 s for neat $MgCl_2$ to roughly 100 ms for $MgCl_2$/**Do3** (6.7%). The sideband selective double frequency sweep (ssDFS) pulse scheme was used to transfer population from the satellites into the central transition to increase the signal. A theoretical maximum enhancement of 2*I* can be obtained using ssDFS. The QCPMG detection scheme was also used. A series of echo pulses was applied with signal detection between the echoes. This leads to a so-called spikelet spectrum in which the regular Hahn echo signal is split into a manifold of sharp lines (spikelets) which resembles the envelope of the echo spectrum. Since the intensity of the echo is distributed over a few spikelets, the signal-to-noise ratio increases significantly. The ssDFS and QCPMG schemes were combined in accordance with the literature to get maximum enhancement.

CPMAS ^{13}C NMR measurements were recorded at room temperature on a Varian VNMRS 400 MHz spectrometer (9.4 T, 104.6 MHz for ^{13}C) using a triple resonance 3.2mm Varian T3MAS probe at 15 or 20 kHz MAS using 75 or 100 kHz ^{1}H decoupling. Additional ^{13}C CPMAS experiments were performed on Varian VNMRS 600 and 850 MHz spectrometers (14.1 T, 156.9 MHz for ^{13}C and 20.0 T, 221.4 MHz for ^{13}C) using triple resonance 3.2 mm and 4.0 mm Varian T3MAS probes. Fast MAS ^{1}H measurements and ^{1}H SQDQ measurements were performed on the 850 MHz spectrometer using triple resonance 1.2 mm and 3.2 mm Varian T3MAS probes.

Deconvolution results for selected ^{13}C resonances in the spectra of $MgCl_2$/**Do1** adducts at different donor loadings are shown in Figure A-3.3. For the -OCH_2- resonance, a one-component fit is also shown. The comparison of panel B-E and C-F clearly highlights the presence of additional components at higher

field in the spectrum of adduct $MgCl_2$/**Do1** (4%) compared to $MgCl_2$/**Do1** (10%).

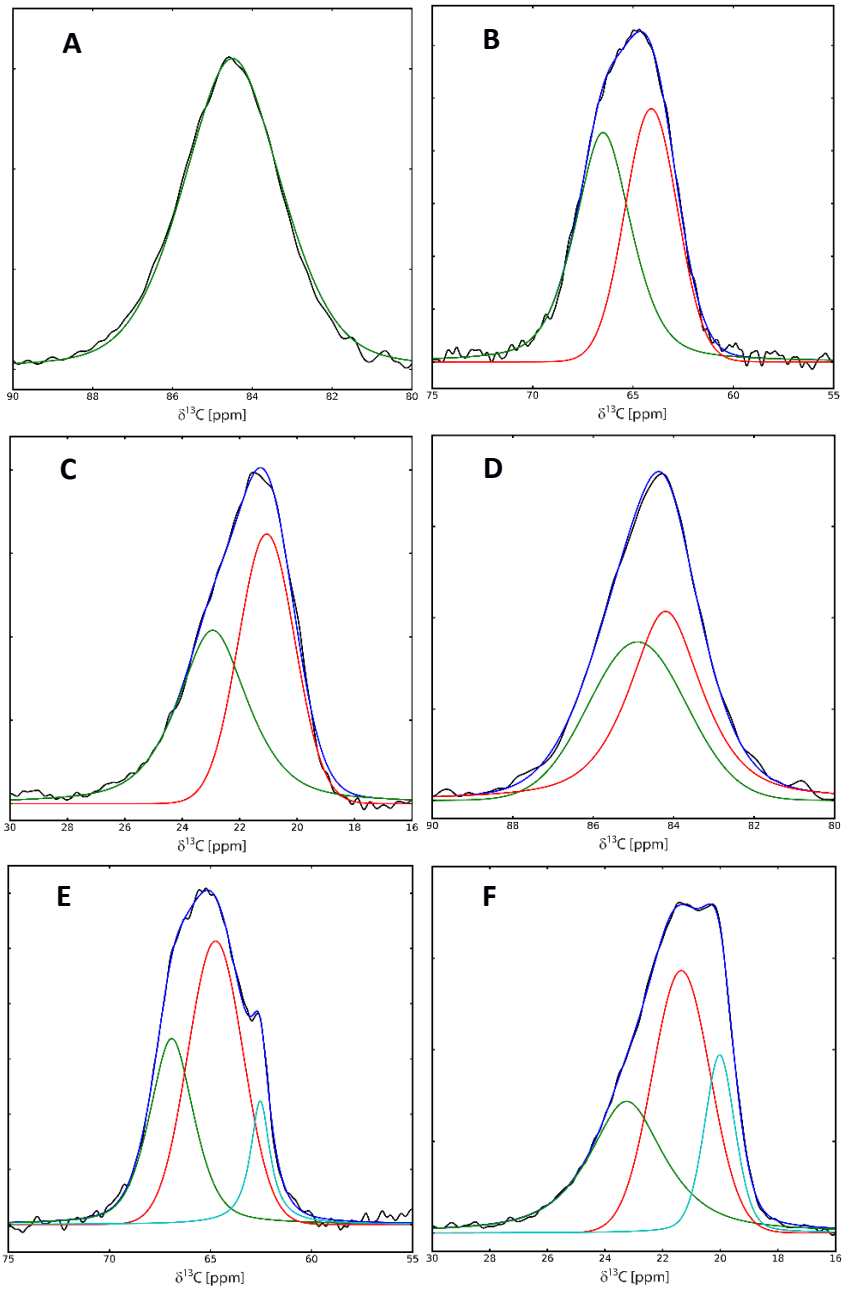

Figure A-3.2. Deconvolution of selected resonances in the CPMAS ^{13}C NMR spectra of (A-C) $MgCl_2$/**Do1** (10%) and (D-F) $MgCl_2$/**Do1** (4%) adducts. -OCH_2- resonance: (A,D); -OCH_3 resonance: (B,E); -CH_3 resonance: (C,F).

References

[1] Moore, E. P., Jr. (Ed.) *Polypropylene Handbook: Polymerization, Characterization, Properties, Processing, Applications*; Hanser Publishers: Munich, 1996.

[2] Cecchin, G.; Morini, G.; Piemontesi, F. *Ziegler-Natta Catalysts*. In *Kirk-Othmer Encyclopedia of Chemical Technology (5th Ed.),* Wiley: Hoboken (NJ), 2007; *Vol. 26*, p. 502.

[3] (a) Busico, V.; Cipullo, R.; Monaco, G.; Talarico, G.; Vacatello, M.; Chadwick, J. C.; Segre, A. L.; Sudmeijer, O. *Macromolecules* **1999,** *32*, 4173. (b) Vittoria, A.; Meppelder, A.; Friederichs, N.; Busico, V.; Cipullo, R. *ACS Catal.* **2017**, *7*, 4509.

[4] (a) Toto, M.; Morini, G.; Guerra, G.; Corradini, P.; Cavallo, L. *Macromolecules* **2000,** *33*, 1134. (b) Correa, A.; Piemontesi, F.; Morini, G.; Cavallo, L. *Macromolecules* **2007,** *40*, 9181. (c) Brambilla, L.; Zerbi, G.; Piemontesi, F.; Nascetti, S.; Morini, G. *J. Phys. Chem. C* **2010,** *114*, 11475. (d) Potapov, A. G.; Politanskaya, L. V. *J. Mol. Catal. A: Chem.* **2013,** *368*, 159.

[5] Song, B. G.; Ihm, S.-K. *J. Appl. Polym. Sci.* **2014,** *131*, 40536.

[6] Smith, M. E. *Appl. Magn. Reson.* **1993**, *4*, 1.

[7] (a) Kresse G., Furthmüller J. *Phys. Rev. B* **1996**, *54*, 169. (b) Kresse, G.; Joubert, D. *Phys. Rev. B*, **1999**, *59*, 1758.

[8] Dovesi, R.; Saunders, V. R.; Orlando, R.; Zicovich-Wilson, C. M.; Pascale, F.; Civalleri, B.; Doll, K.; Bush, I. J.; D'Arco, P.; Lunell, M. *Crystal 2009 User Manual*, University of Turin (Italy).

[9] Perdew, J. P.; Burke, K.; Ernzerhof, M. *Phys. Rev. Lett.* **1997**, *78*, 1396.

[10] (a) Grimme, S. *J. Comput. Chem.* **2006**, *27*, 1787. (b) Grimme, S.; Antony, J.; Ehrlich, S.; Krieg, S. *J. Chem. Phys.* **2010**, *132*, 154104.

[11] Dion, M.; Rydberg, H.; Schröder, E.; Langreth, D. C.; Lundqvist, B. I. *Phys. Rev. Lett.* **2004**, *92*, 246401.

[12] Becke, A. D. *J. Chem. Phys.* **1993**, *98*, 5648.

[13] D'Amore, M.; Credendino, R.; Budzelaar, P. H. M.; Causà, M.; Busico, V. *J. Catal*. **2012**, *286*, 103.

[14] Ahlrichs, R. *J. Chem. Phys.* **1992**, *97*, 2571.

[15] Capone F.; Rongo, L.; D'Amore, M.; Budzelaar, P. H. M.; Busico V. *J. Phys. Chem. C* **2013**, *17*, 24345.

[16] Clayden, N. J.; Jones, P. J. V. *J. Chem. Soc. Perkin Trans. 2* **1990**, *31*, 175.

[17] Heikkinen, H.; Liiti¨a, T.; Virkkunen, V.; Leinonen, T.; Helaja, T.; Denifl, P. *Solid State Nucl. Magn. Reson.* **2012**, *43*, 36.

[18] Sormunen, P.; Hjertberg, T.; Iiskola, E. *Makromol. Chem.* **1990**, *191*, 2663.

[19] (a) Chien, J. C. W.; Dickinson, L. C.; Vizzini, J. *J. Polym. Sci. A: Polym. Chem.* **1990**, *28*, 2321. (b) Abis, L.; Albizzati, E.; Giannini, U.; Giunchi, G.; Santoro, E.; Noristi, L. *Makromol. Chem.* **1988**, *189*, 1595. (c) Terano, M.; Saito, M.; Kataoka, T. *Makromol. Chem., Rapid Commun.* **1992**, *13*, 103.

[20] Pakkanen, T.; Vahasarja, E.; Pakkanen, T.; Iiskola, E.; Sormunen, P. *J. Catal.* **1990**, *121*, 248.

[21] Breuza E. *Computational and Structural Study of Model and Industrial Ziegler-Natta Catalysts, PhD Thesis;* Federico II University of Naples, 2016.

[22] Abelard, J.; Wilmsmeyer, A. R.; Edwards, A. C.; Gordon, W. O.; Durke, E. M.; Karwacki, C. J.; Troya, D.; Morris, J. R. *J. Phys. Chem. C* **2016**, *120*, 13024.

[23] Hunter, C. A.; Lawson, K. R.; Perkins, J.; Urch, C. J. *J. Chem. Soc., Perkin Trans. 2* **2001**, *2*, 651.

[24] (a) Bazhenov, A.; Linnolahti, M.; Pakkanen, T. A.; Denifl, P.; Leinonen, T. *J. Phys. Chem. C* **2014**, *118*, 4791. (b) Kuklin, M. S.; Bazhenov, A. S.; Denifl, P.; Leinonen, T.; Linnolahti, M.; Pakkanen, T. A. *Surf. Sci.* **2015**, *635*, 5. (c) Bazhenov, A. S.; Denifl, P.; Leinonen, T.; Pakkanen, A.; Linnolahti, M.; Pakkanen, T. A. *J. Phys. Chem. C* **2014**, *118*, 27878. (d) Lee, J. W.; Jo, W. H. *J. Organomet. Chem.* **2009**, *694*, 3076.

[25] Cheruvathur, A. V.; Langner, E. H. G.; Niemantsverdriet, J. W. H.; Thune, P. C. *Langmuir* **2012**, *28*, 2643.

[26] Gaussian 09, Revision A.1; Frisch, M. J.; Trucks, G. W.; Schlegel, H. B.; Scuseria, G. E.; Robb, M. A.; Cheeseman, J. R.; Scalmani, G.; Barone, V.; Mennucci, B.; Petersson, G. A.; Nakatsuji, H.; Caricato, M.; Li, X.; Hratchian, H. P.; Izmaylov, A. F.; Bloino, J.; Zheng, G.; Sonnenberg, J. L.; Hada, M.; Ehara, M.; Toyota, K.; Fukuda, R.; Hasegawa, J.; Ishida, M.; Nakajima, T.; Honda, Y.; Kitao, O.; Nakai, H.; Vreven, T.; Montgomery, J. A., Jr.; Peralta, J. E.; Ogliaro, F.; Bearpark, M.; Heyd, J. J.; Brothers, E.; Kudin, K. N.; Staroverov, V. N.; Kobayashi, R.; Normand, J.; Raghavachari, K.; Rendell, A.; Burant, J. C.; Iyengar, S. S.; Tomasi, J.; Cossi, M.; Rega, N.; Millam, M. J.; Klene, M.; Knox, J. E.; Cross, J. B.; Bakken, V.; Adamo, C.; Jaramillo, J.; Gomperts, R.; Stratmann, R. E.; Yazyev, O.; Austin, A. J.; Cammi, R.; Pomelli, C.; Ochterski, J. W.; Martin, R. L.; Morokuma, K.; Zakrzewski, V. G.; Voth, G. A.; Salvador, P.; Dannenberg, J. J.; Dapprich, S.; Daniels, A. D.; Farkas, Ö.; Foresman, J. B.; Ortiz, J. V.; Cioslowski, J.; Fox, D. J. Gaussian, Inc., Wallingford CT, 2009. User's reference at http://www.gaussian.com/.

[27] (a) Von Arnim, M.; Ahlrichs, R. *J. Comp. Chem.* **1998**, *19*, 1746. (b) Ahlrichs, R. *Phys. Chem. Chem. Phys.* **2004**, *6*, 5119.

[28] Tao, J.; Perdew, J. P.; Staroverov, V. N.; Scuseria, G. E. *Phys. Rev. Lett.* **2003**, *91*, 146401.

[29] Ratner, M.; Redfern, P. C.; Curtiss, L. A. *J. Comp. Chem.* **2001**, *22*, 976.

[30] Zhao, Y.; Truhlar, D. G. *J. Phys. Chem.* **2006**, *110*, 5121.

[31] (a) Grimme, S.; Antony, J.; Ehrlich, S.; Krieg, H. *J. Chem. Phys*. **2010**, *132*, 154104. (b) Grimme, S.; Ehrlich, S.; Goerigk, L. *J. Comp. Chem*. **2011**, *32*, 1456.

[32] (a) Becke, A. D. *Phys. Rev. A* **1988**, *38*, 3098. (b) Perdew, J. P. *Phys. Rev. B* **1986**, *33*, 8822.

[33] Ehm, C.; Antinucci, G.; Budzelaar, P. H. M.; Busico, V. *J. Organomet. Chem.* **2014,** *772*, 161.

[34] Provasi, G. A.; Sauer, S. P. A. *J. Chem. Phys.* **2001**, *115*, 1324.

[35] Kutzelnigg, W.; Fleischer, U.; Schindler, M. *The IGLO-Method: Ab Initio Calculation and Interpretation of NMR Chemical Shifts and Magnetic Susceptibilities*; Springer-Verlag: Heidelberg, 1990: Vol. 23.

[36] Dunning T. H., Jr. *J. Chem. Phys.* **1989**, *90*, 1007.

[37] Weigend, F.; Ahlrichs, R. *Phys. Chem. Chem. Phys.* **2005**, *7*, 3297.

Chapter 4. Computational modeling of Ti(III) surface species

4.1. Introductory remarks

Active site precursors of $MgCl_2$-supported ZNC are Ti(IV) surface species, but there is general consensus that the active sites are Ti(III)-C σ-bonds.[1,2] This is mainly based on the fact that most Ti(IV)-C σ-bonds formed by alkyl-Al activation are unstable towards homolytic cleavage; as a matter of fact, the original Ziegler's catalyst made by reacting $TiCl_4$ with TEA in heptane solution was based on β-$TiCl_3$. The results of a very recent ESR investigation[4] on a fourth-generation catalyst (containing a phthalate ID) are consistent with such a view. A mechanistic DFT evaluation of plausible precatalyst activation routes can be found in ref. 5.

In Chapter 1, we discussed at some length how state-of-the-art DFT-D calculations led several independent authors to conclude that stable $TiCl_4$ adsorbates can only form on $MgCl_2$(110) or equivalent crystal terminations. This, however, does not necessarily carry over to the active Ti(III) sites; in particular, one cannot rule out the hypothesis of extensive reconstruction phenomena upon activation and/or in the early stages of polymerization.

In the framework of this thesis project, we modeled by periodic DFT-D the formation of plausible alkylated Ti(III) species from $TiCl_4$ precursors by reaction with TEA, and estimated their thermodynamic stability. Calculated ESR parameters were then compared with experimental ones.[4] For computational details we refer to Appendix A-4.

4.2 Periodic DFT-D evaluations of Ti(III) species formation and stability

In this section we report and discuss the results of a periodic DFT-D study on the formation of Ti_xCl_{3x} adducts (x = 1 or 2) with $MgCl_2$(110) and $MgCl_2$(104) surfaces, as originally suggested by Corradini and coworkers (Chapter 1 and Figure 1.2).[6]

Optimized DFT-D structures are shown in Figure 4.1, whereas calculated stabilities are reported in Table 4.1.

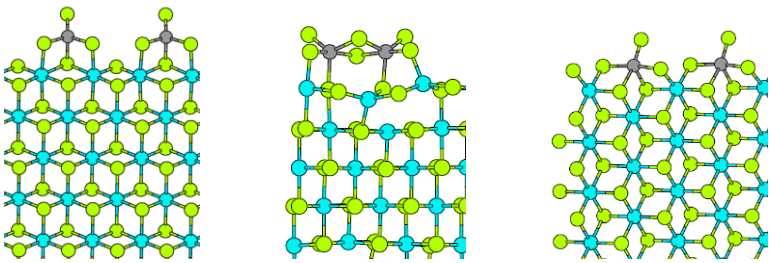

Figure 4.1. Optimized structures of periodic DFT-D $MgCl_2$(hkl)/Ti_xCl_{3x} model adducts at maximum degree of surface coverage ϑ (calculations performed at B3LYP-D2/TZVP level; see Appendix A-4 for details).

Table 4.1. Relative and absolute ΔG values, in kcal mol(Ti)$^{-1}$, for the formation of the $MgCl_2$(hkl)/Ti_xCl_{3x} model adducts of Figure 4.1 with different electronic structures (number of unpaired electron(s) $\Delta n = n_{spin\ \alpha} - n_{spin\ \beta}$), calculated at B3LYP-D2/TZVP level (see text and Appendix A-4 for details).

	ΔG (kcal mol^{-1})	ΔG_{rel} (kcal mol^{-1})
$MgCl_2$ (104)/$TiCl_3$, ϑ = ½, Δn = 1	-14.2	4.8
$MgCl_2$ (104)/Ti_2Cl_6, ϑ = 2/3, Δn = 2	-8.6	10.4
$MgCl_2$ (104)/Ti_2Cl_6, ϑ = 2/3, Δn = 0	-8.5	10.5
$MgCl_2$ (110)/$TiCl_3$, ϑ = 1, Δn = 1	-19.0	0.0

The following two facts should be noted:

(i) The optimized DFT-D structures of the mononuclear adducts are very similar to Corradini's qualitative models[6] (Figure 1.2 B', C'), with a distorted tetrahedral Ti coordination geometry for the $MgCl_2$(104)/$TiCl_3$ adduct, and a distorted trigonal bipyramidal Ti coordination geometry for the $MgCl_2$(110)/$TiCl_3$ adduct. On the other hand, for the putative dinuclear $MgCl_2$(104)/Ti_2Cl_6 adduct (Figure 1.2-A') our calculations indicated a severe distortion of the Ti coordination geometry and the underlying $MgCl_2$ surface as well.

(ii) Calculated ΔG values (Table 4.1) show that, similarly to what was found before for $TiCl_4$ chemisorption, mononuclear $TiCl_3$ chemisorption on $MgCl_2$(110) is preferred over that on $MgCl_2$(104). Dinuclear Ti_2Cl_6 adsorption on $MgCl_2$(104) turned out to be higher in energy by ~10 kcal/mol relative to the mononuclear $MgCl_2$(110)/$TiCl_3$ adduct, and by ~5 kcal/mol relative to the mononuclear $MgCl_2$(104)/$TiCl_3$ adduct; species with different spin states (namely, a 'ferromagnetic' triplet spin state (Δn = 2) and an

'antiferromagnetic' broken symmetry singlet state (Δn = 0)) were found to be very close in energy (within 0.1 kcal/mol).

We then investigated the thermodynamics of the activation process of all three Ti(IV) precursors by TEA (Table 4.2) and Al_2Et_6 (Table 4.3). Overall, the process was always predicted to be exergonic, once again with a slightly lower Gibbs free energy for the mononuclear adduct on $MgCl_2$(110).

Table 4.2. Calculated ΔE and ΔG values (in kcal mol^{-1}) for the alkylation and reduction of $TiCl_4$ surface precursors by $AlEt_3$ (see text and Figures 1.2 and 4.1).

Eq		ΔE	ΔG
1	$[MgCl_2(104)]$-$TiCl_4$ + $AlEt_3$ → $[MgCl_2(104)]$-$TiCl_3$ + Et• + $AlEt_2Cl$	30.9	20.2
	$[MgCl_2(110)]$-$TiCl_4$ + $AlEt_3$ → $[MgCl_2(110)]$-$TiCl_3$ + Et• + $AlEt_2Cl$	32.2	18.0
	$[MgCl_2(104)]$-Ti_2Cl_8 + 2 $AlEt_3$ → $[MgCl_2(104)]$-Ti_2Cl_6 + 2 Et• + 2 $AlEt_2Cl$	29.6	15.5
2	Et• → ½ Et-Et+ ½ Et=Et	-32.2	-29.3
3	$[MgCl_2(104)]$-$TiCl_3$ + $AlEt_3$ → $[MgCl_2(104)]$-$TiCl_2Et$ + $AlEt_2Cl$	1.9	0.2
	$[MgCl_2(110)]$-$TiCl_3$ + $AlEt_3$ → $[MgCl_2(110)]$-$TiCl_2Et$ + $AlEt_2Cl$	-3.3	-3.1
	$[MgCl_2(104)]$-Ti_2Cl_6 + $AlEt_3$ → $[MgCl_2(104)]$-Ti_2Cl_5Et + $AlEt_2Cl$	-2.0	-0.7
4	$[MgCl_2(104)]$-$TiCl_4$ + $AlEt_3$ → $[MgCl_2(104)]$-$TiCl_3$ + $AlEt_2Cl$ + ½ Et-Et + ½ Et=Et	-1.3	-9.2
	$[MgCl_2(110)]$-$TiCl_4$ + $AlEt_3$ → $[MgCl_2(110)]$-$TiCl_3$ + $AlEt_2Cl$ + ½ Et-Et + ½ Et=Et	0.0	-11.4
	$[MgCl_2(104)]$-Ti_2Cl_8 + 2 $AlEt_3$ → $[MgCl_2(104)]$-Ti_2Cl_6 + 2 $AlEt_2Cl$ + Et-Et + Et=Et	-2.5	-13.9
5	$[MgCl_2(104)]$-$TiCl_4$ + 2 $AlEt_3$ → $[MgCl_2(104)]$-$TiCl_2Et$ + 2 $AlEt_2Cl$ + ½ Et-Et + ½ Et=Et	0.6	-9.0
	$[MgCl_2(110)]$-$TiCl_4$ + 2 $AlEt_3$ → $[MgCl_2(110)]$-$TiCl_2Et$ + 2 $AlEt_2Cl$ + ½ Et-Et + ½ Et=Et	-3.3	-14.5
	$[MgCl_2(104)]$-Ti_2Cl_8 + 3 $AlEt_3$ → $[MgCl_2(104)]$-Ti_2Cl_5Et + 3 $AlEt_2Cl$ + Et-Et + Et=Et	-4.5	-14.5

Table 4.3. Calculated ΔE_{red} and ΔG_{red} values, in kcal mol^{-1}, for the alkylation and reduction of $TiCl_4$ precursors by Al_2Et_6 (see text and Figures 1.2 and 4.1).

Eq		ΔE_{red}	ΔG_{red}
6	$2\ AlEt_3 \rightarrow Al_2Et_6$	-20.5	-2.2
	$2\ AlEt_2Cl \rightarrow Al_2Et_4Cl_2$	-27.5	-15.9
1a	$[MgCl_2(104)]\text{-}TiCl_4 + ½\ Al_2Et_6 \rightarrow [MgCl_2(104)]\text{-}TiCl_3 + Et\bullet + ½\ Al_2Et_4Cl_2$	27.4	13.3
	$[MgCl_2(110)]\text{-}TiCl_4 + ½\ Al_2Et_6 \rightarrow [MgCl_2(110)]\text{-}TiCl_3 + Et\bullet + ½\ Al_2Et_4Cl_2$	28.7	11.1
	$[MgCl_2(104)]\text{-}Ti_2Cl_8 + Al_2Et_6 \rightarrow [MgCl_2(104)]\text{-}Ti_2Cl_6 + 2\ Et\bullet + Al_2Et_4Cl_2$	26.1	8.6
3a	$[MgCl_2(104)]\text{-}TiCl_3 + ½\ Al_2Et_6 \rightarrow [MgCl_2(104)]\text{-}TiCl_2Et + ½\ Al_2Et_4Cl_2$	-1.6	-6.6
	$[MgCl_2(110)]\text{-}TiCl_3 + ½\ Al_2Et_6 \rightarrow [MgCl_2(110)]\text{-}TiCl_2Et + ½\ Al_2Et_4Cl_2$	-6.7	-9.9
	$[MgCl_2(104)]\text{-}Ti_2Cl_6 + ½\ Al_2Et_6 \rightarrow [MgCl_2(104)]\text{-}Ti_2Cl_5Et + ½\ Al_2Et_4Cl_2$	-3.7	-4.1
4a	$[MgCl_2(104)]\text{-}TiCl_4 + ½\ Al_2Et_6 \rightarrow [MgCl_2(104)]\text{-}TiCl_3 + ½\ Al_2Et_4Cl_2 + ½\ Et\text{-}Et + ½\ Et{=}Et$	-4.8	-16.0
	$[MgCl_2(110)]\text{-}TiCl_4 + ½\ Al_2Et_6 \rightarrow [MgCl_2(110)]\text{-}TiCl_3 + ½\ Al_2Et_4Cl_2 + ½\ Et\text{-}Et + ½\ Et{=}Et$	-3.5	-18.2
	$[MgCl_2(104)]\text{-}Ti_2Cl_8 + Al_2Et_6 \rightarrow [MgCl_2(104)]\text{-}Ti_2Cl_6 + Al_2Et_4Cl_2 + Et\text{-}Et + Et{=}Et$	-6.0	-20.7
5a	$[MgCl_2(104)]\text{-}TiCl_4 + Al_2Et_6 \rightarrow [MgCl_2(104)]\text{-}TiCl_2Et + Al_2Et_4Cl_2 + ½\ Et\text{-}Et + ½\ Et{=}Et$	-6.4	-22.7
	$[MgCl_2(110)]\text{-}TiCl_4 + Al_2Et_6 \rightarrow [MgCl_2(110)]\text{-}TiCl_2Et + Al_2Et_4Cl_2 + ½\ Et\text{-}Et + ½\ Et{=}Et$	-10.2	-28.2
	$[MgCl_2(104)]\text{-}Ti_2Cl_8 + 3/2\ Al_2Et_6 \rightarrow [MgCl_2(104)]\text{-}Ti_2Cl_5Et + 3/2\ Al_2Et_4Cl_2 + Et\text{-}Et + Et{=}Et$	-9.7	-24.8

4.3 Cluster DFT-D calculation of Ti(III) ESR parameters

In the framework of a collaboration with the research groups of Profs. Elio Giamello and Mario Chiesa at the University of Turin, also involving Prof. Sabine van Dorslaer at the University of Antwerp (Belgium), a 4th-generation $MgCl_2$ catalyst (featuring a phthalate ID) was characterized by ESR.[4] The spectra were recorded after activation of the precatalyst with TEA vapor. ESR-active Ti(III) species were estimated to represent 10±3% of the total Ti in the sample. Two distinctly different species were found, along with a minor amount of a third one (Table 4.4).

Table 4.4. Multi-sited best-fit interpretation of experimental ESR parameters for 4th-generation $MgCl_2$ catalyst (featuring a phthalate ID) after activation with TEA (see text): Ti(III) g tensor and hyperfine A tensor (hfi; MHz), Euler angles (deg), and nuclear quadrupole Ti(III)-^{35}Cl interaction (nqi; MHz).[4]

Ti(III) g tensor			Relative abundance (%)	hfi tensor			Euler angles	nqi
g_x	g_y	g_z		A_x	A_y	A_z	α, β, γ	C_Q
1.936±0.005	1.888±0.005	1.84±0.01	76	-3±1	-2±2.5	7.5±3.5	-30, 50, 40	-9±3
1.960±0.01	1.945±0.01	1.89±0.01	23					
1.976±0.01	1.968±0.01	1.96±0.01	1					

We carried out DFT calculations of g, hyperfine, and nuclear quadrupole tensors for two model clusters of composition $Mg_8Cl_{16}TiCl_3$ and $Mg_7Cl_{14}TiCl_3$, mimicking the local surface environment of a $TiCl_3$ unit adsorbed on a $MgCl_2$(110)-like termination and a $MgCl_2$(104)-like termination, respectively (Figure 4.2). The results are reported in Tables 4.5 and 4.6.

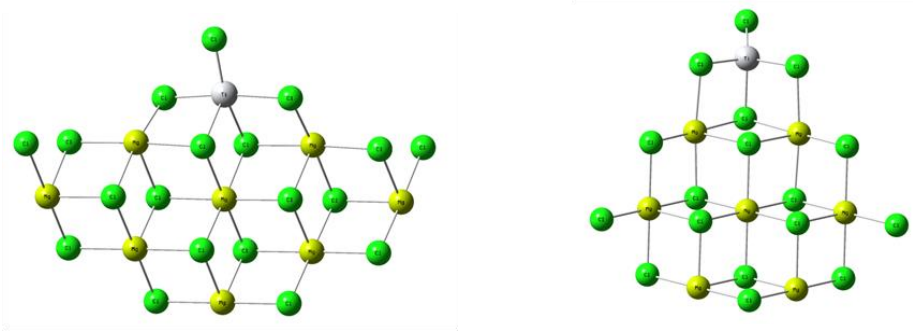

Figure 4.2. DFT-D structures of $Mg_8Cl_{16}TiCl_3$ (left), and $Mg_7Cl_{14}TiCl_3$ (right)

Table 4.5. Calculated values of the g tensor for the two model clusters of Figure 4.2 (see text).

	$Mg_8Cl_{16}TiCl_3$			$Mg_7Cl_{14}TiCl_3$		
Functional	g_x	g_y	g_z	g_x	g_y	g_z
B3LYP	1.939	1.888	1.788	1.968	1.909	1.850
PBE0	1.933	1.881	1.768	1.966	1.903	1.837

Table 4.6. Calculated values (in MHz) of the hyperfine isotropic coupling constant (a_{iso}), anisotropic spin dipole coupling tensor (T), and nuclear quadrupole interaction (C_Q) for the two model clusters of Figure 4.2 (see text).

Cluster	Functional		a_{iso}	T_x	T_y	T_z	C_Q
$Mg_8Cl_{16}TiCl_3$	B3LYP	Cl-1	-2.8	-0.8	0.0	0.8	8.4
		Cl-2	2.7	-5.4	-2.6	7.9	14.1
		Cl-3	1.0	-6.2	-2.9	9.1	12.4
		Cl-4	0.4	-4.1	-1.0	5.1	9.9
		Cl-5	0.1	-1.1	0.4	0.7	9.6
	PBE0	Cl-1	-3.4	-0.9	0.1	0.9	8.5
		Cl-2	1.4	-6.0	-2.0	8.0	14.5
		Cl-3	0.1	-6.7	-2.4	9.1	13.4
		Cl-4	-0.9	-4.8	-0.7	5.4	9.8
		Cl-5	-0.3	-1.3	0.4	0.8	9.6
$Mg_7Cl_{14}TiCl_3$	B3LYP	Cl-1	1.2	-4.9	-2.8	7.7	10.4
		Cl-2	-1.3	-4.7	-1.7	6.4	8.6
		Cl-3	1.4	-5.1	-3.0	8.2	10.4
		Cl-4	-2.1	-1.8	-1.5	3.3	5.7
	PBE0	Cl-1	0.1	-5.3	-2.5	7.8	11.0
		Cl-2	-2.6	-5.5	-1.3	6.8	8.5
		Cl-3	0.3	-5.6	-2.7	8.3	11.0
		Cl-4	-2.9	-1.8	-1.4	3.2	6.8

The Ti(III) **g** tensors for the two model clusters (Table 4.5) are consistent with the hypothesis of the single *d* electron occupying an orbital lying in the xy plane (d_{xy} and d_{x2-y2}). A good agreement with experiment was only obtained for the $Mg_8Cl_{16}TiCl_3$ cluster. The *hfi* and *nqi* tensors (Table 4.6), in turn, did not show revealing differences between the two models.

All this considered, one can conclude that the most abundant ESR-active Ti(III) species in the experimentally characterized system was an isolated distorted octahedral Ti adduct with a vacant coordination site on $MgCl_2$(110). This would be consistent with the periodic calculations of relative stability in § 4.1.

4.4 Summary and conclusions

In this Chapter we addressed the long-standing question of the chemical activation of the precatalyst by means of the Al-alkyl cocatalyst. DFT-D evaluations of epitaxial Ti_xCl_{3x} (x = 1 or 2) adsorbates on $MgCl_2$(104) and $MgCl_2$(110) terminations, as originally proposed by Corradini and coworkers, were carried out using high-end periodic and cluster methods. The relative stability of various Ti(III) model species *via* reduction and alkylation of Ti(IV) precursors by Et_3Al was calculated, along with the Ti(III) ESR parameters for comparison with experimental data for model and real-world catalysts. Overall, at odds with previous qualitative hypotheses, pointing to dinuclear Ti_2Cl_6 species on $MgCl_2$(104) terminations, our results indicated the mononuclear Ti(III) adsorbates on $MgCl_2$(110) terminations as the most plausible ZNC active species.

Appendix A-4

Computational details for the periodic DFT-D calculations

All calculations were performed with the CRYSTAL09 package, a periodic ab-initio program based on atom-centered (Gaussian) basis sets.[7] Starting from an α-$MgCl_2$ crystal, the surface of interest was generated with a slab approach as implemented in the code: slab models (2-D infinite systems) with translational symmetry in the *hkl* planes defining the surface were cut out of the previously optimized bulk structure. For each considered surface, slabs of different thickness were modeled, checking the convergence of the surface formation energy, γ_{hkl}. The slab thickness necessary for convergence, that is approaching bulk-like behavior in the middle of the slab, turned out to lie in the range of 1.5–2.0 nm, depending on the spacing between the given *hkl* lattice planes (Table A-4.1).

The adsorption models were built and analyzed allowing for the maximum number of symmetry operations; in particular, the up and down symmetry was ensured. The coverage degree ϑ (defined as the fraction of exposed adsorption sites occupied by the adsorbate on the given surface) was set at the maximum value allowed by the chosen adsorption mode. Geometries were optimized at the B3LYP[8] level including Grimme's semi-empirical corrections for dispersion (DFT-D2)[9], with the modification proposed by Civalleri and coworkers.[10] In all cases, the following all-electron basis sets were used: triple-ζ plus polarization (TZVP) quality basis sets for Mg, Cl and Ti atoms (the exponents of the outermost and most diffuse *sp* orbitals were optimized as previously described[11]), and Ahlrichs VTZ plus polarization[12] quality basis sets for Al, C and H atoms (for the latter two, the basis set was also optimized in previous work[13]). The positions of all atoms were fully relaxed along with

the cell parameters. With reference to the CRYSTAL09 user's manual,[7] in the evaluation of the Coulomb and Hartree−Fock exchange series, the five threshold parameters determining the level of accuracy were set at 7, 7, 7, 7, 18 values. The threshold on the SCF energy was set to 10^{-8} Ha for the geometry optimizations, and 10^{-10} Ha for the frequency calculations. The reciprocal space was sampled according to a regular sub-lattice with shrinking factor equal to 6.

In the case of open-shell Ti(III) and radical species, spin-polarized DFT was employed. For the dinuclear Ti(III)-Ti(III) two-spin system, we considered the triplet state (two unpaired electrons) and the broken symmetry singlet, in which one Ti atom has positive spin magnetic moment, while the other has a negative one, although the total spin magnetic moment is 0, as in the case of closed-shell singlet.

Vibrational analysis was carried out under standard conditions (p = 1 bar, T = 298 K) to calculate the enthalpy and entropy contributions. The vibrational analysis protocol used is similar to the computational scheme of many molecular codes, using analytical gradients of the energy with respect to nuclear positions and numeric differentiation to obtain the Hessian at the central point of the first Brillouin zone (Γ point, point k = 0 in BZ).

Structures were manipulated and visualized with the XCrysDen program.[14]

Table A4-1. Calculated surface formation energy vs slab thickness at B3LYP/TZVP and B3LYP-D2/TZVP level for various surfaces of $MgCl_2$.

	B3LYP		B3LYP-D2	
(h k l)	γ_{hkl} **[J m^{-2}]**	**Slab thickness [Å]**	γ_{hkl} **[J m^{-2}]**	**Slab thickness [Å]**
	0.004	8.7	0.087	8.4
	0.003	13.4	0.093	12.8
(001)	0.003	19.6	0.094	18.6
	0.003	26.8	0.095	25.6
	0.003	32.9	0.095	31.4
	0.003	38.9	0.096	37.1
	0.14	3.1	0.24	2.9
(104)	0.15	9.3	0.27	8.9
	0.15	13.8	0.27	13.5
	0.15	19.5	0.27	18.9
	0.31	3.9	0.42	3.8
(110)	0.26	10.2	0.38	9.8
	0.27	15.2	0.39	15.0

Computational details for the cluster DFT-D approach

All calculations were performed using the Gaussian09 software package.[15] Before embarking into ESR calculations of $MgCl_2$/Ti(III) adducts, we tested the performance of different hybrid DF's (B3LYP[8], PBE0[16], M06[17]) and basis sets (EPR-II[18], Chipman DZPD[19], N07D[20]) for the lighter atoms (while 6-311++G(d,p) was always employed for Ti) in the evaluation of the ESR parameters of a well-known molecular system, namely $Ti[(H_2O)_6]^{3+}$ (Figure A-4.1) The results of this benchmarking are reported in Tables A-4.2 to A-4.5. The best performance, in terms of accuracy and efficiency (Mean Absolute Deviation: ~0.020 for the g tensor), was observed for B3LYP and PBE0 functionals, in combination with the N07D basis set.

In view of the above, calculations for the $MgCl_2/TiCl_3$ systems were carried out at B3LYP and PBE0 levels, with 6-311++G(d,p) for Ti and N07D (double ζ quality basis set) for Cl and Mg.

The model cluster geometries were obtained from previously optimized $MgCl_2(hkl)/Ti_xCl_{3x}$ periodic systems (§ 4.2), cutting them according to the procedure described in the CRYSTAL09 user's manual.[7] ESR parameter calculations were performed without re-optimization. In all cases, very accurate quality settings were chosen (SCF = VeryTight and Int(Grid=UltraFine); see Gaussian09 user's reference[15]).

The gyromagnetic tensor **g** was computed as the sum of the free-electron value g_e (2.0023193), the relativistic mass correction term (Δg_{rm}), the gauge first-order corrections (Δg_c) and one last term arising from the coupling of the orbital Zeeman (OZ) and the spin-orbit coupling (SOC) operator (Eq. 4.1).[20]

$$\mathbf{g} = g_e + \Delta g_{rm} + \Delta g_c + \Delta g_{OZ/SOC} \qquad \text{(Eq. A-4.1)}$$

The hyperfine interactions of the electron spin with the nuclear spin of the ^{35}Cl atoms were also determined. The hyperfine spin-Hamiltonian was given in terms of the hyperfine coupling tensor (**A**), which describes the interaction between the electron spin density and the nuclear magnetic momentum of nucleus. **A** can be represented as the sum of an isotropic part (a_{iso}) and a dipolar part **T** (**T** is a traceless 3 x 3 matrix).

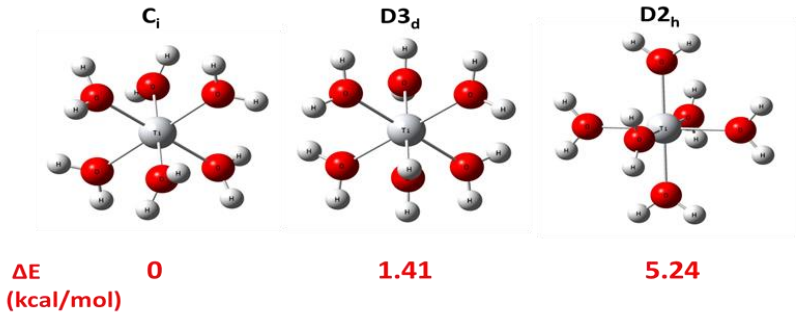

Figure A-4.1. Optimized structures of three models of the $[Ti(H_2O)_6]^{3+}$ species with different symmetries, with corresponding relative ΔE values (B3LYP/6-311++G(d,p) level).

Table A-4.2. Experimental g tensor, hyperfine A tensors (hfi; MHz) for the ^{1}H - ^{17}O interaction in $[Ti(H_2O)_6]^{3+}$.[21]

			^{1}H				^{17}O			
g_x	g_y	g_z	a_{iso}	T_x	T_y	T_z	a_{iso}	T_x	T_y	T_z
1.896	1.896	1.994	4.8 ± 0.2	-3.3± 0.2	-3.3 ± 0.2	6.6 ± 0.2	7.5 ± 0.5	-0.5± 0.5	2.0 ± 0.5	-1.5 ± 0.5
			7.5 ± 0.2	-4.0 ± 0.2	-4.0 ± 0.2	8.0 ± 0.2				

Table A-4.3. Calculated g tensor, hyperfine isotropic coupling constant (a_{iso}), anisotropic spin dipole coupling tensor (T) in MHz for $[Ti(H_2O)_6]^{3+}$ (C_i symmetry).

C_i	g_x	g_y	g_z	a_{iso} ($^1H_1$)	a_{iso} ($^1H_2$)	a_{iso} ($^1H_3$)	a_{iso} ($^1H_4$)	a_{iso} ($^1H_5$)	a_{iso} ($^1H_6$)	a_{iso} ($^{17}O_1$)	a_{iso} ($^{17}O_2$)	a_{iso} ($^{17}O_3$)
B3LYP												
EPR-II	1.859	1.899	1.938	4.9	4.9	4.8	4.4	4.4	4.4	5.7	5.7	5.7
N07D	1.859	1.899	1.938	4.6	4.6	4.6	4.1	4.1	4.1	5.1	5.1	5.1
Chipman	1.858	1.898	1.938	4.8	4.8	4.7	4.2	4.2	4.2	5.6	5.6	5.7
M06												
EPR-II	2.033	2.208	2.206	5.6	5.5	5.5	5.2	5.3	5.2	9.1	9.1	9.1
N07D	2.033	2.075	2.055	4.8	4.7	4.7	4.4	4.4	4.3	8.2	8.2	8.2
Chipman	2.036	2.082	2.206	5.3	5.2	5.2	4.8	4.9	4.8	8.9	8.9	8.9
PBE0												
EPR-II	1.852	1.893	1.935	4.7	4.7	4.7	4.3	4.4	4.3	7.7	7.8	7.8
N07D	1.850	1.893	1.934	4.2	4.2	4.1	3.9	3.9	3.9	7.0	7.0	7.0
Chipman	1.851	1.893	1.935	4.6	4.6	4.6	4.2	4.2	4.2	7.7	7.7	7.7

Table A-4.4. Calculated g tensor, hyperfine isotropic coupling constant (a_{iso}), anisotropic spin dipole coupling tensor (T) in MHz for $[Ti(H_2O)_6]^{3+}$ (D_{3d} symmetry).

$D3_d$	**g_x**	**g_y**	**g_z**	**a_{iso} ($^1H_1$)**	**a_{iso} ($^1H_2$)**	**a_{iso} (^{17}O)**
B3LYP						
EPR-II	1.885	1.885	2.000	6.8	7.9	6.7
N07D	1.883	1.883	2.000	6.3	7.3	6.4
Chipman	1.884	1.884	2.000	6.6	7.7	6.7
M06						
EPR-II	2.306	2.306	2.000	7.8	9.0	10.5
N07D	2.278	2.278	1.999	6.6	8.0	9.3
Chipman	2.301	2.301	2.000	7.3	8.5	10.4
PBE0						
EPR-II	1.881	1.881	2.000	6.6	7.4	9.1
N07D	1.880	1.880	2.000	6.0	6.6	8.6
Chipman	1.880	1.880	2.000	6.5	7.3	9.0

Table A-4.5. Calculated g tensor, hyperfine isotropic coupling constant (a_{iso}), anisotropic spin dipole coupling tensor (T)in MHz for the $[Ti(H_2O)_6]^{3+}$ complex (D_{2h} symmetry).

$D2_h$	**g_x**	**g_y**	**g_z**	**a_{iso} ($^1H_1$)**	**a_{iso} ($^1H_2$)**	**a_{iso} ($^1H_3$)**	**a_{iso} ($^{17}O_1$)**	**a_{iso} ($^{17}O_2$)**	**a_{iso} ($^{17}O_3$)**
B3LYP									
EPR-II	1.890	1.924	1.932	-0.4	10.8	11.6	5.0	7.6	7.8
N07D	1.889	1.923	1.931	-0.4	10.0	10.8	5.0	7.0	7.3
Chipman	1.889	1.924	1.932	-0.5	10.5	11.3	5.0	7.5	7.8
M06									
EPR-II	1.837	2.146	2.576	0.0	12.0	13.0	4.5	14.4	14.5
N07D	1.830	2.140	2.457	-0.1	10.3	11.1	4.2	12.8	13.0
Chipman	1.838	2.145	2.567	-0.1	11.3	12.2	4.4	14.0	14.2
PBE0									
EPR-II	1.885	1.924	1.930	-0.5	10.5	11.3	5.7	10.7	11.0
N07D	1.884	1.924	1.930	-0.4	9.4	10.2	5.8	10.0	10.4
Chipman	1.884	1.924	1.930	-0.5	10.2	11.0	5.7	10.6	10.9

References

[1] Moore, E. P., Jr. (Ed.) *Polypropylene Handbook: Polymerization, Characterization, Properties, Processing, Applications*; Hanser Publishers: Munich, 1996.

[2] Cecchin, G.; Morini, G.; Piemontesi, F. *Ziegler-Natta Catalysts*. In *Kirk-Othmer Encyclopedia of Chemical Technology (5th Ed.)*, Wiley: Hoboken (NJ), 2007; *Vol. 26*, p. 502.

[3] Boor, J., Jr. *Ziegler-Natta Catalysts and Polymerizations*; Academic Press: New York, 1979.

[4] Morra, E.; Giamello, E.; Van Doorslaer, S.; Antinucci, G.; D'Amore, M.; Busico, V.; Chiesa, M. *Angew. Chem. Int. Ed.* **2015**, *54*, 4857.

[5] Bahri-Laleh, N; Correa, A.; Mehdipour-Ataei, S.; Arabi, H.; Haghighi, M. N.; Zohuri, G.; Cavallo, L. *Macromolecules* **2011**, *44*, 778.

[6] Corradini, P.; Barone, V.; Fusco, R.; Guerra, G. *Gazz. Chim. Ital.* **1983**, *113*, 601.

[7] Dovesi, R.; Saunders, V.R.; Orlando, R.; Zicovich-Wilson, C.M.; Pascale, F.; Civalleri, B.; Doll, K.; Bush, I. J.; D'Arco, P.; Lunell, M. *Crystal 2009 User Manual*, University of Turin (Italy).

[8] Becke, A. D. *J. Chem. Phys.* **1993**, *98*, 5648.

[9] Grimme, S. *J. Comput. Chem.* **2006**, *27*, 1787.

[10] Civalleri, B.; Zicovich-Wilson, C. M.; Valenzano, L.; Ugliengo, P. *CrystEngComm.* **2008**, *10*, 405.

[11] D'Amore, M.; Credendino, R.; Budzelaar, P. H. M.; Causà, M.; Busico, V. *J. Catal.* **2012**, *286*, 103.

[12] Ahlrichs, R. *J. Chem. Phys.* **1992**, *97*, 2571.

[13] Capone, F.; Rongo, L.; D'Amore, M.; Budzelaar, P. H. M.; Busico, V. *J. Phys. Chem. C* **2013**, *17*, 24345.

[14] Kokalj, A. *Comp. Mater. Sci.* **2003**, *28*, 155. Code available from http://www.xcrysden.org/.

[15] Gaussian 09, Revision A.1; Frisch, M. J.; Trucks, G. W.; Schlegel, H. B.; Scuseria, G. E.; Robb, M. A.; Cheeseman, J. R.; Scalmani, G.; Barone, V.; Mennucci, B.; Petersson, G. A.; Nakatsuji, H.; Caricato, M.; Li, X.; Hratchian, H. P.; Izmaylov, A. F.; Bloino, J.; Zheng, G.; Sonnenberg, J. L.; Hada, M.; Ehara, M.; Toyota, K.; Fukuda, R.; Hasegawa, J.; Ishida, M.; Nakajima, T.; Honda, Y.; Kitao, O.; Nakai, H.; Vreven, T.; Montgomery, J. A., Jr.; Peralta, J. E.; Ogliaro, F.; Bearpark, M.; Heyd, J. J.; Brothers, E.; Kudin, K. N.; Staroverov, V. N.; Kobayashi, R.; Normand, J.; Raghavachari, K.; Rendell, A.; Burant, J. C.; Iyengar, S. S.; Tomasi, J.; Cossi, M.; Rega, N.; Millam, M. J.; Klene, M.; Knox, J. E.; Cross, J. B.; Bakken, V.; Adamo, C.; Jaramillo, J.; Gomperts, R.; Stratmann, R. E.; Yazyev, O.; Austin, A. J.; Cammi, R.; Pomelli, C.; Ochterski, J. W.; Martin, R. L.; Morokuma, K.; Zakrzewski, V. G.; Voth, G. A.; Salvador, P.; Dannenberg, J. J.; Dapprich, S.; Daniels, A. D.; Farkas, Ö.; Foresman, J. B.; Ortiz, J. V.; Cioslowski, J.; Fox, D. J. Gaussian, Inc., Wallingford CT, 2009. User's reference at http://www.gaussian.com/.

[16] Adamo, C.; Barone, V. *J. Chem. Phys.* **1999**, *110*, 6158.

[17] (a) Zhao, Y.; Truhlar, D.G. *Theor. Chem. Acc.* **2008**, *120*, 215. (b) Zhao, Y.; Schultz, N. E.; Truhlar D. G. *J. Chem. Theory Comput.* **2006**, *2*, 364.

[18] Barone, V. in *Recent Advances in Density Functional Methods, Part I* (D. P. Chong, Ed.); World Scientific Publ. Co.: Singapore, 1996.

[19] Chipman, D. M. *Theor. Chim. Acta* **1989**, *76*, 73.

[20] (a) Barone, V.; Cimino, P.; Stendardo, E. *J. Chem. Theory Comput.* **2008,** *4*, 751. (b) Barone, V.; Cimino, P. *Chem. Phys. Lett.* **2008**, *454*, 139.

[21] Maurelli, S.; Livraghi, S.; Chiesa, M.; Giamello, E.; Van Doorslaer, S.; Di Valentin, C.; Pacchioni, G. *Inorg. Chem.* **2011**, *50*, 2385.

Chapter 5. Concluding remarks

$MgCl_2$-supported Ziegler-Natta catalysts for the industrial production of isotactic polypropylene (iPP) are very peculiar heterogeneous systems, in which Ti-based active species on a nano-structured $MgCl_2$ support are modified by co-adsorbed organic Lewis Bases (LB), which seem to play a role similar to ancillary ligands in molecular catalysts. Real-world (pre)catalysts, as well as simple(r) model systems thereof, were investigated by means of advanced spectroscopies including solid-state QNMR, CPMAS NMR, and ESR, all integrated with state-of-the-art DFT-D calculations. The general aim of the project was to shed light on the nature and structure of the catalytic surfaces.

In Chapter 2 we focused on the preparation and characterization of the 'activated' dry $MgCl_2$ support, and of binary $MgCl_2$/LB model adducts. Notwithstanding the apparent simplicity of the systems, this turned out to be the most complicated part of the entire project. Indeed, solid-state ^{1}H NMR spectra invariably highlighted the presence of substantial amounts of adventitious molecular and/or dissociated water in neat $MgCl_2$, even when starting from a thoroughly dried material. Additional (ATR) FTIR studies confirmed that it is extremely difficult to prevent water from saturating the coordinatively unsaturated surfaces of $MgCl_2$ crystallites, even when these are carefully manipulated inside a high-performance glovebox. On the other hand, the problem was far less acute for simple $MgCl_2$/LB model adducts, due to the shielding effect of the chemisorbed LB molecules.

As a matter of fact, thorough solid-state NMR studies of the aforementioned adducts could be carried out (Chapter 3). The ^{25}Mg and ^{35}Cl QNMR spectra of samples at natural isotopic abundance were poorly informative, due to a low signal-to-noise ratio and a (very) broad line width. On the other hand, the

comparison of CPMAS ^{13}C NMR spectra with DFT-D simulated ones was very useful to narrow the hypotheses on possible LB adsorption sites and modes. In particular, it was possible to confirm the strong preference of 1,3-diethers for chelating adsorption on $MgCl_2$(110)-like terminations, which expose 4-coordinated Mg (as previously suggested by the previous literature based on DFT calculations only).

The ESR study of an activated 4th-generation catalyst (Chapter 4), in turn, demonstrated conclusively that molecular-like Ti(III) surface species are present. Comparison of experimental and DFT-D-calculated ESR parameters gave strong evidence that such species are mononuclear adducts on $MgCl_2$(110) (or equivalent surfaces).

Albeit preliminary, this study highlighted the great potential of the approach; the integration of advanced spectroscopic investigation with state-of-the-art DFT modeling provide a powerful tool for the development and understanding of the active constructs involved in the catalytic process at the molecular level. Further studies on isotopically enriched samples will likely lead to more thorough information, and ultimately to an atomic scale description of these fascinating and elusive catalysts.

Acknowledgements

This Ph.D. thesis project was part of the research programme of the Dutch Polymer Institute (DPI). I gratefully acknowledge the DPI for funding the project and my Ph.D. studentship.

First of all, I wish to thank Prof. Vincenzo Busico, who gave me the chance to carry out this PhD project in his group and for his patience, motivation, and immense knowledge. His guidance helped me in all the time of research and writing of this thesis.

I wish to thank Prof. Christophe Copéret (ETH) for hosting me in his research group for a 3-month stage (May-July 2017), and Profs. Arno Kentgens (Radboud Universiteit Nijmegen) and Mario Chiesa (University of Turin) for the structural research collaboration within the DPI.

PhD Course Activity Summary

Candidate: Giuseppe Antinucci **Supervisor:** Prof. Vincenzo Busico

1) Attended Courses (6 minimum, 8 hours each):

- *Electronic Structure Methods for Solid State Materials* (Prof. Ana B. Munoz Garcia, May 2015).
- *Structural Analysis of Materials at Nanometer Length Scale with Small Angle X-ray Scattering* (Prof. Finizia Auriemma, September 2015).
- *Origins of Chirality and Asymmetric Synthesis* (Prof. Giovanni Palumbo, October 2015).
- *Neutron Scattering* (Prof. Reiner Zorn, October 2015).
- *Application of Conformational Analysis to the Structural Study of Synthetic Polymeric Materials.* (Prof. Beniamino Pirozzi, November 2016).
- *Selective Organometallic Catalysis: Systems and Advanced Techniques* (Prof. Peter H. M. Budzelaar, May 2017).

2) Attended Seminars:

Title	Speaker	Date	Place
Advanced Technology for Life Sciences by Using TEM	Dr. Paolo Grianti	24/11/2014	DSC-UniNa
Characterization of Complex Ethylene-Propylene Copolymers – A Journey Inside the Analytical Techniques	Dr. Benjamin Monrabal	27/11/2014	DSC-UniNa
Le Fitotossine: un'Avventura Lunga 40 Anni	Prof. Antonio Evidente	10/12/2014	DSC-UniNa
New Chiral Catalysis Derived from Iron(II) and Bismuth(III) for Asymmetric Synthesis	Prof. Thierry Ollevier	15/12/2014	DSC-UniNa
Enhanced Sampling Techniques Aimed at Characterizing Protein-	Dr. Walter	22/12/2014	DSC-

Ligand Binding for Drug Design Applications	Rocchia		UniNa
Multiscale Modeling of Soft Materials: Atoms, Beads and Fields	Prof. Giuseppe Milano	19/02/2015	DSC-UniNa
In Searching of the Chemical Basis of the Origin of Life: from Experiments to the Space missions (I)	Prof. Guido Barone	23/02/2015	DSC-UniNa
In Searching of the Chemical Basis of the Origin of Life: from Experiments to the Space missions (II)	Prof. Guido Barone	27/02/2015	DSC-UniNa
European Large Facilities: Neutron and Synchroton Sources	Prof. Serge Perez	06/05/2015	DSC-UniNa
Non-conventional Techniques for the Modification of Carbon Nanoforms	Prof. Ester Vazques	28/04/2015	DSC-UniNa
Ab-initio Theoretical Study of Lanthanide Impurities In Ionic Cristals: Tb^{3+} Doped Fluorides	Prof- Jose Luis Pascal	17/07/2015	DSC-UniNa
Effect of Graphene Oxide in Disentangled Polyethylene and LLDPE	Dr. Sara Ronca	17/07/2015	DSC-UniNa
Disentangled UHMWPE: Synthesis to Mechanical Properties	Dr. Sara Ronca	17/07/2015	DSC-UniNa
Bleaching Systems in Domestic Laundry Detergents	Dr. Giulia Bianchetti	29/10/2015	DSC-UniNa
Scientific Calculator	Prof. Michele Vacatello	11/11/2015	DSC-UniNa
Industria e Ricerca nel Settore Biofarmaceutico: Bisogni Attuali e	Dr. Sara Carillo	25/02/2016	DSC-

Sviluppi Futuri			UniNa
Basics of Detergents Formulations and Challenges	Dr. Giulia Bianchetti	16/03/2016	DSC-UniNa
Progettazione, Risk-assessment e Controllo Qualità del Packaging Alimentare: il ruolo inatteso del Chimico	Dr. Vincenzo Benessere	17/03/2016	DSC-UniNa
The versatility of Mesoscopic Solar Cells	Prof. Anders Hagfeldt	14/04/2016	DSC-UniNa
La Chimica: Un diamante	Dr. Mario Marzullo	21/04/2016	DSC-UniNa
Il Percorso Multidisciplinare nello Sviluppo di un Nuovo Farmaco:DF2755A	Dr. Samuele Lillini	16/05/2016	DSC-UniNa
EPDM: Back to basics	Prof. Martin Van Duin	29/04/2016	DCS-UniNa
Supramolecular Chemistry of Chiral Calixarenes	Prof. Mauro Mocerino	13/01/2017	DSC-UniNa
La Chimica tra le Biotecnologie e la Bioeconomia	Dr. Piero Bellofiore	10/04/2017	DSC-UniNa
Using ab-initio methods to describe ground and excited state reactivity	Dr. Ilaria Ciofini	31/10/2017	DSC-UniNa

DSC-UniNa = Dept. of Chemical Sciences – University of Naples Federico II

3) Visiting periods in Institutions different from University of Naples "Federico II":

Host Institution	Country	Start Date	End Date
Radboud University Nijmegen	The Netherlands	03/02/2016	19/02/2016
ETH Zurich	Switzerland	24/04/2017	26/07/2017

4) Publications:

- Blaakmeer, E. S. (Merijn), Antinucci G., Busico V., van Eck, Ernst R. H., Kentgens, Arno P. M., Solid-State Investigation of $MgCl_2$, Crystal Support. *Journal of Physical Chemistry C*, **2016**, *120*, 6063.
- Morra E., Giamello E., Van Doorslaer S., Antinucci G., D'Amore M., Busico V., Chiesa M., Probing the Coordinative Unsaturation and Local Environment of Ti^{3+} Sites in an Activated High-Yield Ziegler-Natta Catalyst. *Angew. Chem. Int. Ed.*, **2015**, *54*, 4857.

5) Attended congresses/workshops/summer schools:

- *International Summer School "Ab initio Modeling in Solid State Chemistry – MSSC2015",* Imperial College London (UK), 14-18 September 2015.
- *Dutch Polymer Institute Annual Meeting, Arnhem (The Netherlands), 3-4 November 2015*.
- *Dutch Polymer Institute Research Training Course in Polyolefins Block 1. Chemistry / Catalysis / Polymer Microstructure – Advanced Module,* Sorrento (I), June 2016.
- *Dutch Polymer Institute Annual Meeting, Arnhem (The Netherlands), 23-24 November 2016*.
- *4th Blue Sky Conference on Catalytic Olefin Polymerization*, Sorrento (I), July 2016.